HARVARD UNIVERSITY

Graduate School of Arts and Sciences

DISSERTATION ACCEPTANCE CERTIFICATE

The undersigned, appointed by the

Harvard John A. Paulson School of Engineering and Applied Sciences
have examined a dissertation entitled:

"Oxide thin films and surfaces for electro-optics and superconductivity"

presented by: Larissa B. Little

Signature _____
Typed name: Professor Jennifer Hoffman

Signature _____
Typed name: Professor Julia Mundy

Signature _____
Typed name: Professor Robert Westervelt

Signature _____
Typed name: Professor Marko Loncar

April 22, 2024

Oxide thin films and surfaces for electro-optics and superconductivity

A DISSERTATION PRESENTED
BY
LARISSA B. LITTLE
TO
THE DEPARTMENT OF SCHOOL OF ENGINEERING AND APPLIED SCIENCES

IN PARTIAL FULFILLMENT OF THE REQUIREMENTS
FOR THE DEGREE OF
DOCTOR OF PHILOSOPHY
IN THE SUBJECT OF
APPLIED PHYSICS

HARVARD UNIVERSITY
CAMBRIDGE, MASSACHUSETTS
APRIL 2024

Thesis advisors: Professor Jennifer Hoffman & Professor Julia Mundy Larissa B. Little

Oxide thin films and surfaces for electro-optics and superconductivity

Abstract

In this dissertation, I describe work completed on several oxide materials. Firstly, I discuss the effects of doping the cuprate $YBa_2Cu_3O_{7-\delta}$ with calcium, which introduces an alternate cleavage plane and allows for the inspection of bulk-like superconducting properties via scanning tunnelling microscopy. Secondly, I discuss thin film growth of $BaTiO_3$ using conventional oxide molecular beam epitaxy (MBE), focusing particularly on the effects of stoichiometry and strain. Thirdly, I introduce preliminary results of using hybrid MBE to grow thin film $BaTiO_3$. Finally I briefly describe work growing the binary oxide anatase TiO_2 via both conventional and hybrid MBE. To the best of my knowledge, this report is the first of hybrid MBE-grown anatase.

$YBa_2Cu_3O_{7-\delta}$ has favorable macroscopic superconducting properties of T_c up to 93 K and H_{c2} up to 150 T. However, its nanoscale electronic structure remains mysterious because bulk-like electronic properties are not preserved near the surface of cleaved samples for easy access by local or surface-sensitive probes. It has been hypothesized that Ca-doping at the Y site could induce an alternate cleavage plane that mitigates this issue. We use scanning tunneling microscopy to study both Ca-free and 10% Ca-doped YBCO, and find that the Ca-doped samples do indeed cleave on an alternate plane, yielding a spatially-disordered partial (Y,Ca) surface. Our density functional theory calculations support the increased likelihood of this new cleavage plane in Ca-doped $YBa_2Cu_3O_{7-\delta}$. On this surface, we image a superconducting gap with average value 24 ± 3 meV and characteristic

length scale 1–2 nm, similar to Bi-based high-T_c cuprates, and the first map of gap inhomogeneity in the $YBa_2Cu_3O_{7-\delta}$ family.

Thin films of barium titanate show promise as an electro-optic candidate for integrated photonic devices due to their high Pockels coefficient of up to 1300 pm/V — over 30 times higher than lithium niobate, the most widely used electro-optic material. In this work we show that both excess Ba and excess Ti have a higher solubility in strained thin films than in bulk crystals. Excess Ti causes defects in the crystal structure of the film that seem proportional in quantity to the amount of excess Ti, as expected for an element with a sticking factor of one. Excess Ba, on the other hand, does not incorporate into the film. Instead it seems to rise to the surface of the thin film during growth to form a water-sensitive BaO-based compound that can be rinsed off post-growth to expose a single crystal $BaTiO_3$ film.

To explore strain effects on $BaTiO_3$, 80 nm films are grown on a variety of scandate substrates with epitaxial compressive strains of up to 1.5%. Films have a low surface roughness, and are single crystal with high crystallinity. We find that the nature of the scandate substrates makes it challenging to find the index of refraction of the films, but see features in the UV-vis spectra that correspond to the expected bandgap values. We construct a confocal measuring setup that can be used to access the electro-optic tensor of interest (r_{42}), and show preliminary results that indicate a strong electro-optic response.

Exploratory work of hybrid MBE growth of $BaTiO_3$ is conducted, mapping out the complex phase space of adsorption controlled growth. Effects of Ba:Ti ratio, growth speed, liquid nitrogen cooling, substrate temperature, and oxygen plasma are each briefly demonstrated and discussed.

Contents

Citation of collaborators and prior work

Chapter 2 appears in its entirety in manuscript:

Larissa B. Little, Jennifer Coulter, Ruizhe Kang, Ilija Zeljkovic, Dennis Huang, Can-Li Song, Toshinao Loew, Han-Jong Chia, Jason D. Hoffman, John T. Market, Bernhard Keimer, Boris Kozinsky, Jennifer E. Hoffman. 2024. "Alternate cleavage structure and electronic inhomogeneity in Ca-doped $YBa_2Cu_3O_{7-\delta}$." arXiv:2402.03238.

Chapter 3 uses sections from the manuscripts referenced below for Chapters 4 and 5.

Chapter 4 is adapted from manuscript:

Ashley Cavanagh*, Larissa B. Little*, Yang Zhang, Charles M. Brooks, Ismail El-Baggari, Robert Westervelt, Julia A. Mundy. "Stoichiometry Effects in Barium Titanate" (in preparation)

Chapter 5 is adapted from manuscript:

Larissa B. Little, David Barton, Keith Powell, Neil Sinclair, Ashley Cavanagh, Charles M. Brooks, Matthew Yeh, Chen Jie Xin, Robert Westervelt, Marko Loncar, Julia A. Mundy "Strain Effects in Barium Titanate" (in preparation)

Chapter 6 discusses films grown and analysis conducted in collaboration with Benazir Fazlioglu-Yalcin with support from Charles M. Brooks and Jason D. Hoffman.

Listing of figures

Acknowledgments

When I decided to leave my job in industry to pursue a Ph.D., I wanted to be intellectually challenged, to have freedom to pursue knowledge even if it wasn't clear that it would be immediately relevant or applicable, and finally to do research I cared about and believed in. Looking back on my journey through graduate school, I am so grateful to all of those who made it possible for me to realize those aspirations.

First and foremost are my advisors. I am grateful to have had the chance to work with both Jenny Hoffman and Julia Mundy. Jenny accepted me into her group as a first year and I've consistently appreciated and benefited from Jenny's deep knowledge of cuprate superconductivity as well as her ability to quickly drill down to tough scientific questions. Over the course of my Ph.D., Jenny also broke the record for running across the country; she truly is as an inspiration to pursue dreams of all kinds tenaciously.

When a pandemic, supply chain problems, and other external circumstances disrupted my planned research, I started to work with Julia Mundy on electro-optic materials. This project gradually became my full-time research, and I am so grateful to both Julia and Jenny for supporting me in pursuing this opportunity, which has been a perfect fit for my interests and skills. Julia has been an im-

portant source of oxide MBE knowledge during my years at Harvard. I've learned from her ability to foresee and removing all kinds of obstacles, allowing research to be done efficiently. Julia also strikes the difficult balance between moonshot ideas and consistent scientific progress, a skill I greatly admire.

Thank you to everyone in both the Hoffman and Mundy groups for always being willing to chat about interesting science and to lend a hand (often literally during system maintenance or tricky experiments). In particular Jason Hoffman and Charles Brooks have taught me so much about MBE and have been true mentors and role models to me as oxide film growth gurus. Either Charles or Jason has been an important collaborator in nearly every one of my research efforts. It has been a delight to work with Bena Fazlioglu-Yalcin and Tema Zulu (the Mundy $BaTiO_3$ crew!). Tema's productivity over the past year has been amazing to witness. Bena's deep knowledge of hybrid MBE is matched only by her kindness and positivity, even after long days in the basement of LISE. I'm glad to have had the chance to train Anjola Bamtefa on oxide MBE, and for the friendship that developed as a result. Thank you to Grace Pan, Ben November, Ruizhe Kang, and Nathan Drucker, who are all in my cohort — I feel like we have been traveling companions throughout this journey of graduate school. Kevin Hauser's technical prowess, good ideas, and dedicated work ethic were instrumental in our time improving a tricky STM system. I've greatly appreciated having the chance to work with and learn from Wan-Ting Liao, Alyson Spitzig, Aaron Coe, Stefan Ulrich, Maggie Anderson, Ari Turkiewicz, Tan Dao, Spencer Doyle, Zubia Hasan, Nicole Taylor, Yoony Baek, Abbie Jiang, Dan Ferenc Segedin, Christian Matt, Tatiana Webb, Harry Pirie, Mengke Liu, Dilek Yildiz, Johanna Nordlander, Richard Liu, Denisse Cordova Carrizales, Juliette Nwagwu Ume-Ezeoke, Wenjie Gong, Lauren Kwee, Xavier Piña, Federico Maccagno, Amari Butler, and Annie Ruperto.

I have been extremely lucky in my group of collaborators at Harvard. David Barton was essential in getting the $BaTiO_3$ work off the ground. His knowledge of photonics and materials science and his ability to use that intersectional fluency to further science in both fields is inspiring to me.

Not only did he teach me so much about the world of photonics but was also a partner in early film growth efforts, making late nights much more enjoyable and productive. Jenny Coulter is brilliant and helped me gain a better understanding of how computational and experimental work can compliment each other. Thank you to Ashley Cavanagh, Neil Sinclair, and Keith Powell— it has been a privilege to collaborate closely and learn from each of them.

The staff at Harvard have been wonderful resources for learning about a myriad of techniques and have supported my work in many ways, in particular Arthur McClelland, Jules Gardener, Stephan Kraemer, Jason Tresbeck, Adam Graham, and Jim MacArthur. Thank you to John Doyle, who I had the honor of working with in the N95decon consortium and who has generally been supportive throughout my Ph.D.

Thank you to all the folks who keep the cooling water flowing 24/7, the leaks at bay, and the MBE running during (too frequent) Cambridge brown-outs and to Joel Day and Stuart McNeil who manage that effort. Special thanks to Stephen Concannon, Sean Concannon, Larry O'Connell, Collin O'Connell, Jack Connors, and Joe Sears. As you work to fix or prevent issues, thank you for letting me shadow you, ask (a lot) of questions, and sometimes peek into back rooms where cool infrastructure is tucked away.

Thanks especially to Grace, Anjola, Charles, my DND friends, and Maggie Reagan, whose support has been very meaningful to me in these past few weeks.

Finally, thank you to my parents Zena, and Rob, who engendered in me a love of learning and the bravery to pursue my passions; to my sister Chandra, who has been my best friend for many many years; and to my partner Eric, who has been a bastion of support and brought joy and laughter to my life for many years.

1

Introduction

Over the course of my Ph.D. research, I've had the opportunity to do research in several sub-fields of condensed matter, all focused on the oxide material family. The majority of my research has been on oxide thin film growth via molecular beam epitaxy (MBE), focusing mainly on growth of $La_{2-x}Sr_xCuO_4$ in earlier years with Jenny Hoffman and $BaTiO_3$ in later years with Julia Mundy, the latter of which also included getting a hybrid MBE system up and running. Additionally, in Jenny Hoffman's lab I worked on noise reduction in a commercial scanning tunneling microcope

(STM) system and briefly conducted STM and non-contact atomic force microscopy on oxide films. Finally, during and after COVID, I had the opportunity to spend time learning about density functional theory, which I used to study bulk $YBa_2Cu_3O_{7-x}$.

This dissertation focuses on a subset of the work I have done in my Ph.D. I've focused on the more novel results and research directions. Part I regards work with $YBa_2Cu_3O_{7-\delta}$ and lays out both experimental STM taken by earlier students in the Hoffman lab and the DFT results contributed by Jenny Coulter and myself. Part II of the dissertation covers the majority of my work done with $BaTiO_3$ thin films grown with conventional MBE, some exploratory work on hybrid MBE completed during the last few months of my research as a graduate student, and research done along the way on anatase TiO_2 films.

Although the two parts of the dissertation study different properties of interest — bulk crystal superconductivity and thin film electro-optics respectively — I hope that the range of research in this work displays the rich nature of oxide materials and showcases the flexibility and strength of taking an materials science and applied physics approach across a range of research and application areas.

Part I: Cuprate thin films and surfaces for superconductivity

2

Cleavage and electronic inhomogeneity in Ca-doped $YBa_2Cu_3O_{7-x}$

High-T_c cuprates exhibit chemical, structural, and electronic disorders, which contribute to their rich phase diagram. Scanning tunneling microscopy and spectroscopy (STM and STS) are well-suited to study these atomic-scale properties across a range of temperatures and magnetic fields[1,2]. For example, STM and STS studies on cuprates have been used to quantify inhomogeneity in the

spectral gap[3,4,5,6,7,8], reveal "checkerboard" and other charge orders[9,10], and provide evidence for pair density wave order in some regions of the phase diagram[11,12]. However, only a subset of cuprates are suitable for STM study. Bulk crystals must: (a) cleave easily to reveal terraces of at least 50–100 nm, and (b) retain bulk-like superconductivity at the cleaved surface. Some cuprates such as $La_{2-x}Sr_xCuO_4$ (LSCO) do not cleave, but rather fracture onto an uneven surface. Other cuprates such as $YBa_2Cu_3O_{7-\delta}$ (YBCO) cleave to reveal a flat surface whose electronic structure does not reproducibly represent a bulk superconductor. Thus, most STM work has focused on a limited number of cuprates that fulfill both requirements, particularly $Bi_2Sr_2CaCu_2O_{8+\delta}$ (BSCCO) and other Bi-based cuprates. The limited scope of cuprate STM studies may not be fully representative of the rich high-T_c cuprate material family.

YBCO is an appealing candidate for further STM work to contextualize existing studies on BSCCO. YBCO has high T_c (up to 93 K) and H_{c2} (up to 150 T) in single crystal form[13]. Due to its balance of anisotropy and flexibility, YBCO is also the primary cuprate used in commercial superconducting wire[14]. However, cleaved YBCO does not reproducibly show bulk-like behavior at the surface. The Y plane and the CuO chain planes act as charge reservoirs for the superconducting CuO_2 planes [Fig. 2.1(a)]. When the undoped crystal is cleaved, it typically splits cleanly between the CuO and BaO planes. The internal dipole moment between the charge reservoir CuO and charge neutral BaO planes is therefore disrupted, leading to surfaces with a different electronic environment than the bulk crystal. See Appendix 2.3.1 for a comparison of BSCCO and YBCO cleavage.

Given the electronic disruption upon cleaving YBCO, it is unsurprising that STM results have been varied. On the atomically-resolved CuO chain plane of cleaved YBCO, spectral gaps ranging from ∼18 to ∼30 meV were observed[15,16,17], but several ambiguous gap-edge features were not consistently reproduced (see Table VIII in Fischer et al.[1]. The complicated one-dimensional modulation and spectroscopic features observed on the CuO surface were initially attributed to a charge

density wave[18], but later proposed to be proximity-induced superconductivity and quasiparticle scattering due to O vacancies in the CuO chains[19]. As-grown[20] and etched[21,22,23] YBCO surfaces have also been studied. These surfaces retain some bulk superconducting properties, as demonstrated by direct vortex imaging, but they lack the atomic resolution of cryogenically-cleaved YBCO that is needed to correlate the superconductivity with chemical or structural disorders.

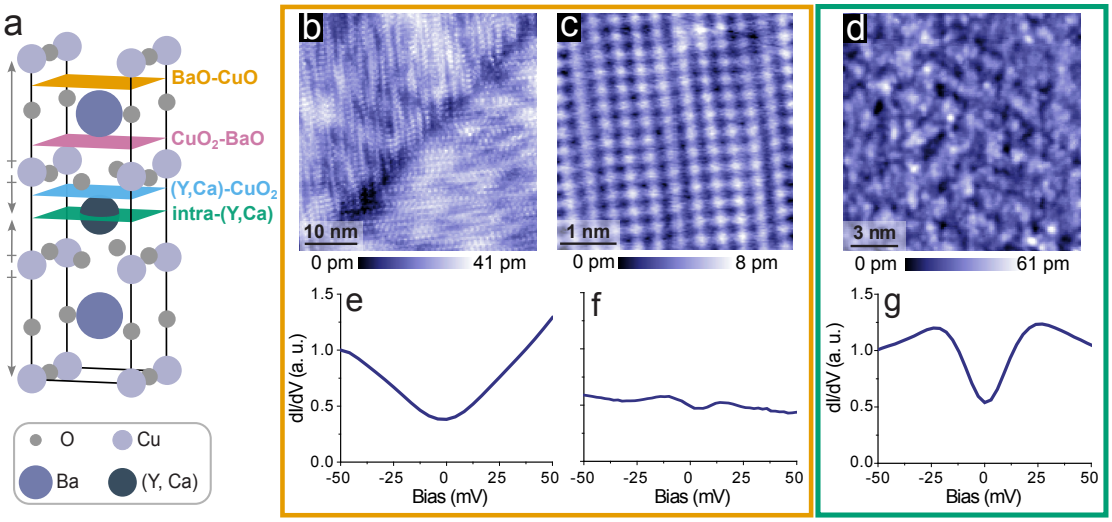

Figure 2.1: (a) YBCO unit cell with dipole moments shown as grey arrows. The four cleavage planes considered here are BaO-CuO (orange), CuO_2-BaO (pink), (Y-Ca)-CuO_2 (blue), and intra-(Y,Ca) (green). (b-g) STM topographs and corresponding dI/dV spectra on various surfaces. (b,e) Optimally doped, Ca-free YBCO cleaved to reveal a CuO surface with a twin boundary, and no apparent superconducting gap. (c,f) Optimally doped, Ca-free YBCO cleaved to reveal a BaO square lattice with a gap that has a high zero bias conductance. (d,g) 10% Ca-doped YBCO with hole doping $p = 0.12$ cleaved on the intra-(Y,Ca) plane to reveal a disordered surface morphology. Spectrum on the (Y,Ca) surface shows a superconducting gap. Experimental conditions: (b,e) setpoint current $I_s = 10$ pA and sample bias $V_s = -150$ mV; (c,f): $I_s = 200$ pA, $V_s = -150$ mV; (d): $I_s = 10$ pA, $V_s = -60$ mV; (g): $I_s = 50$ pA, $V_s = -60$ mV.

Doping YBCO with Ca has been proposed as a possible method for retaining bulk-like properties upon cleavage. Zabolotnyy *et al.* performed angle-resolved photoemission spectroscopy (ARPES) measurements on the surface of cleaved Ca-free YBCO that revealed two components: (1) an overdoped metallic component with hole doping $p \sim 0.3$ regardless of the bulk hole concentration, presumed to come from the CuO_2 plane closest to the surface, and (2) a superconducting compo-

nent presumed to originate from the CuO_2 planes further from the surface. However, in YBCO crystals with 15% Ca substitution at the Y site, the overdoped surface component was suppressed. The authors hypothesized that the Ca substitution results in an alternate cleavage plane that preserves a bulk-like electronic environment for CuO_2 planes near the surface and thus allows better access to study the superconducting properties of the YBCO crystal[24].

Here we study cleaved $YBa_2Cu_3O_{7-\delta}$ and $Y_{0.9}Ca_{0.1}Ba_2Cu_3O_{7-\delta}$ with STM and STS. We demonstrate experimentally and with support from density functional theory (DFT) calculations that Ca-doped YBCO cleaves through the (Y,Ca) crystal plane, revealing a surface that retains bulk-like superconductivity. On this (Y, Ca) surface, we observe a gap of 24 ± 3 meV with a characteristic length scale of 1–2 nm, similar to the spatial inhomogeneity of the superconducting gap reported on Bi-based cuprates.

2.1 Methods

2.1.1 Crystal preparation

We study single crystals of optimally-doped YBCO with $p \sim 16\%$ and underdoped Ca-YBCO with $p \sim 12\%$. The pure YBCO crystals were grown by a standard flux method in yttria-stabilized zirconia (YSZ) crucibles[15]. The Ca-YBCO crystals were synthesized by the solution-growth technique[24] with ∼10% Ca substitution, confirmed by energy-dispersive x-ray (EDX) measurements after the growth. Each Ca is expected to donate one hole to the bulk. Since each unit cell contains two CuO_2 planes per one Ca/Y plane, 10% Ca substitution implies average 5% hole doping per CuO_2 plane [Fig. 2.1(a)]. After synthesis, we annealed the crystals to deplete the oxygen and lower p to a target value of 12%. We first determined the annealing conditions necessary for Ca-free YBCO to have hole doping $p = 7\%$, estimating the hole doping from the c-axis lattice parameter of the crystal[25]. Then, we annealed the 10% Ca-doped YBCO under the same conditions to obtain a total

hole doping of 12%, assuming that the 5% hole doping from the Ca and the 7% hole doping from the oxygen vacancies add linearly. The optimally doped YBCO has $T_c = 91$ K, while the Ca-YBCO has $T_c = 31$ K, measured with magnetic susceptibility and shown in Appendix 2.3.2.

2.1.2 STM and STS measurements

We cleave the YBCO and Ca-YBCO single crystals in ultra-high vacuum at cryogenic temperatures to expose a clean surface and immediately insert them into the STM head. We image the resulting surfaces at 6–7 K using PtIr tips cleaned by field emission on polycrystalline Au foil. All dI/dV measurements are acquired using a standard lock-in amplifier technique with peak-to-peak amplitude 5 meV and frequency 1110 Hz. To measure the superconducting gap map, we acquire dI/dV spectra on a square, densely-spaced pixel grid, and calculate the magnitude of the gap at each point by fitting a Gaussian curve to the more prominent gap-edge peak on the negative side of the spectrum.

2.1.3 DFT cleavage calculations

We use density functional theory (DFT) to investigate the cleavage of pure and Ca-doped YBCO. We compare the total energies of both pure and Ca-doped YBCO cleaved in each of the four configurations shown in Fig. 2.1(a): between the BaO and CuO planes [BaO-CuO], between the CuO_2 and BaO planes [CuO_2-BaO], between the (Y,Ca) and CuO_2 planes [(Y,Ca)-CuO_2], and finally through the (Y,Ca) atomic plane, with 50% of the (Y,Ca) atoms on one of the resulting surfaces and 50% on the other [intra-(Y,Ca)]. We use the intra-(Y,Ca) plane as an approximation of the disordered experimental behavior since true disorder is impractical to model with DFT.

We use the VASP[26,27,28] code with the projector-augmented wave method[29] and the r^{2}SCAN[30] exchange-correlation functional. As the challenges of studying correlated electron systems with

DFT are well documented[30], we follow recent work that validated different methods of computing the structural properties of YBCO[31]. This work suggests that r^{2}SCAN used with an on-site U parameter of 4 eV applied to the Cu d orbitals and the D4 van der Waals correction is the most suitable method for describing the structural properties of YBCO[32]. For cleaved structure calculations, we found D4 to be numerically unstable, and therefore use the D3(BJ) vdW correction with damping parameters $a_1 = 0.4948$, $a_2 = 5.7308$, and $s_8 = 0.7898$, and a scaling factor $s_6 = 1.0000$[33,34], which should produce a similar result[34].

We base our calculations on two initial crystal structures, $YBa_2Cu_3O_7$ and $Y_{0.8}Ca_{0.2}Ba_2Cu_3O_7$, taken from experimental results[35,36]. Forces were converged using a plane-wave energy cutoff of 600 eV. To perform cleaved structure calculations, we use $2\times2\times2$ supercells of the YBCO unit cell and a **k**-mesh of $4\times4\times2$. As DFT does not allow for fractional occupancies, we replace one of every four Y atoms in each of the Y atomic layers in the supercell with a Ca atom to generate a 25% Ca-doped structure (Appendix 2.3.3). Lower Ca-doping is computationally impractical for cleavage calculations, given the large unit cell size.

To calculate the surface energy of different cleavage planes, we follow standard methods[37]. The unit cell structure was split, introducing 0.5 nm of vacuum between layers at the selected surface, as we observed minimal changes to the structure beyond this distance. This yields a slab thickness of 12 atomic layers upon cleavage. Then a structural relaxation with fixed unit cell size was performed to find the new atomic positions and system energies of the cleaved structures. Energies are reported as 'relative energy per atom,' calculated by first finding the total energy of the cleaved system, subtracting the energy of the corrolary bulk system, then dividing by the number of atoms in the calculation. A visualization of the intra-(Y,Ca) cleavage plane is shown in Appendix 2.3.3.

2.2 Results and Discussion

2.2.1 STM on cleaved YBCO and Ca-YBCO

We cleave optimally-doped Ca-free YBCO, and image both the CuO chains and BaO square lattice with atomic resolution. In Fig. 2.1(b), we see one-dimensional CuO chains with modulations, consistent with previous reports [15,18,38,39,16,17,19,40]. Although the surface is atomically smooth, there are 40 pm corrugations at the twin boundary. Our dI/dV spectroscopy on this surface, shown in Fig. 2.1(e), exhibits no gap in our measured bias range, in contrast to some prior work showing a $\sim$25 meV gap [15,17,16]. In Fig. 2.1(c), our BaO surface topography shows the same lattice seen in prior work [16,38]. Our dI/dV spectroscopy on this surface, shown in Fig. 2.1(f), exhibits a weak partial gap, which has not been previously reported on the BaO surface to our knowledge. Our observed BaO gap may be explained by the close proximity of the BaO plane to the superconducting CuO_2 planes, coupled with the lack of charge on the BaO surface.

The Ca-doped YBCO crystal cleaves to reveal a surface with a new morphology, shown in Fig. 2.1(d). This surface is flat but disordered, with no step edges or valleys appearing over several hundred nanometer areas, as shown in Appendix 2.3.2. We do not achieve atomic resolution on this surface. Spectroscopy shows a symmetric gap in the density of states of 24 ± 3 meV around the Fermi level [Fig. 2.1(g)], consistent with the bulk gap [41]. We suggest that Ca-YBCO crystals favor the intra-(Y,Ca) cleavage plane; i.e. they cleave through the (Y,Ca) atomic layer between adjacent CuO_2 layers, leaving a fraction of the (Y,Ca) atoms on either side. This partial (Y,Ca) occupancy is consistent with the disordered surface seen in Fig. 2.1(d). The CuO_2 plane alone is unlikely to explain the disordered surface, as atomically-resolved CuO_2 surfaces have been imaged in BSCCO [42,43].

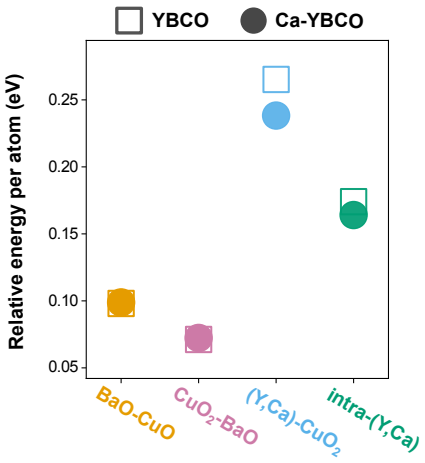

Figure 2.2: DFT-calculated surface energy of both YBCO and 25% Ca-doped YBCO for each of the four possible cleavage planes. In line with experimental findings, Ca-doping increases the probability of cleaving to expose (Y,Ca) atoms by lowering the energy of both the (Y,Ca)-CuO_2 and the intra-(Y,Ca) planes, without significantly affecting the BaO-CuO or CuO_2-BaO plane energies. In contrast to experimental findings, the calculated overall surface energy of the CuO_2-BaO plane is the lowest of all plans for both YBCO and Ca-doped YBCO. See Appendix 2.3.3, Table 2.1 for numerical values.

2.2.2 DFT CLEAVAGE ENERGY

We use DFT to compare the energies of the four cleavage planes in Ca-doped and Ca-free YBCO, as shown in Fig. 2.2. We find that Ca-doping YBCO decreases the energy cost of cleaving on the intra-(Y,Ca) or the (Y,Ca)-CuO_2 planes while minimally changing the cost of cleaving on the BaO-CuO or CuO_2-BaO planes. This trend supports that Ca-doped YBCO is more likely than Ca-free YBCO to cleave to expose the (Y,Ca) atoms, in line with our experimental results. Additionally, the calculations show that leaving 50% of the (Y,Ca) atoms on each surface lowers the cleavage energy compared to cleaving between the Y and CuO_2 planes, again in line with our experimental results. This trend holds true across a range of oxygen stoichiometries (Appendix 2.3.3).

Though the relative energies between Ca-doped and Ca-free YBCO are in line with our experimental observations, the relative energies between different cleavage plans of a single YBCO compound exhibit discrepancies. In our calculations, the CuO_2-BaO plane has the lowest surface energy

of the four possible cleavage planes, indicating that it should be the most favorable. This calculated result is inconsistent with experiments on Ca-free YBCO, where the CuO-BaO plane is the most commonly observed. There are several possible explanations for this discrepancy. Some long-range ordering that is not captured in our moderately-sized unit cells could play an important role in inter-layer bond strength. Experiments have seen charge density waves phases in YBCO with a period of four unit cells [44], while prior DFT work on YBCO indicates that there are a number of stripe phases very close in energy with periodicities of several unit cells [45]. Furthermore, experiments indicate a disordered surface with partial (Y,Ca) occupancy, while disorder cannot be accurately captured in DFT. Finally, and perhaps most importantly, we know that YBCO is a strongly correlated material and the shortcomings of DFT in handling electronic interactions may not adequately capture inter-layer bond strength.

2.2.3 Superconductivity on (Y,Ca) surface

We explore the nanoscale electronic structure by acquiring a simultaneous topography and gap map, in Fig. 2.3. The gap $\Delta(r)$ has an average value of 24 $\pm$ 3 meV, with extremal values from 9 to 35 meV over the 10 nm field of view. This relative variation is comparable to that seen throughout the full doping range in Bi-based cuprates [6,8,46]. The auto-correlation coefficient of the gap map in Fig. 2.3(b) shows a length scale of 1–2 nm [Fig. 2.3(c)], also comparable to the length scale observed in Bi-based cuprates [6,8,46]. We find negligible correlation between the topographic height [$z(r)$], spectral gap [$\Delta(r)$)], and zero bias conductance [ZBC(r)] features [Fig. 2.3(c)], suggesting that the spatial distribution of the spectral gap and ZBC is independent of surface disorder. Together with ARPES experiments on cleaved 15% Ca-doped YBCO that detected spectral weight attributed to Cooper pairing [24], our data suggest that the gap we observe on the new surface can be identified as a superconducting state with spatially inhomogeneous properties similar to that of other cuprates. Spectral gap inhomogeneity seems to be omnipresent in Bi-based cuprates, but gap inhomogeneity

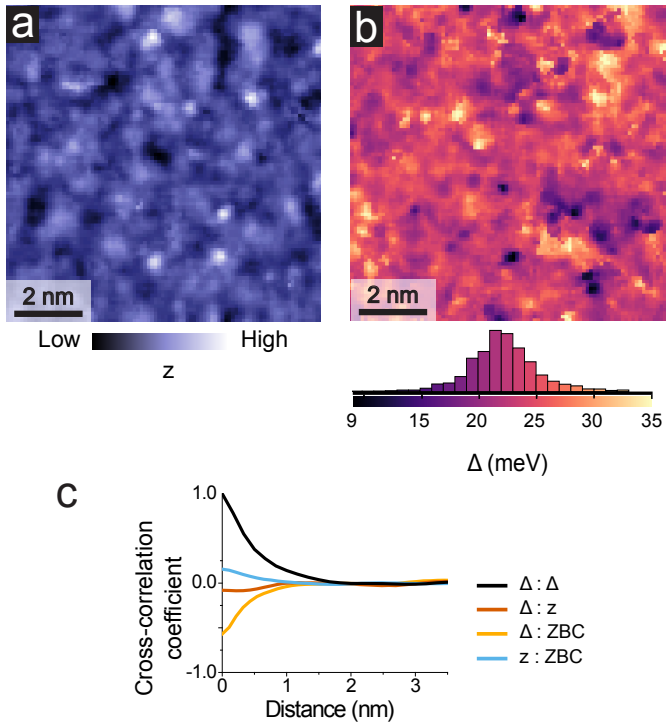

Figure 2.3: (a) Topograph and (b) spectral gap map of $Y_{0.9}Ca_{0.1}Ba_2Cu_3O_{7-\delta}$ acquired simultaneously over a 10 nm square region ($I_s = 50$ pA, $V_s = -60$ mV). (c) Correlation coefficients for gap $\Delta(r)$, zero bias conductance (ZBC), and topographic height z. The auto-correlation coefficient of $\Delta(r)$ shows a characteristic gap length scale of 1–2 nm. The cross-correlation coefficient between gap and topography is low.

was not previously reported in YBCO [17].

Previous STM studies have imaged a disordered vortex lattice in near-optimally-doped BSCCO [47,48] and YBCO [23,16,20]. Vortices in these earlier maps appear as regions of higher ZBC, and lower dI/dV at energies close to the gap edge. In ten tip-sample approaches in magnetic field on two different zero-field-cooled Ca-YBCO samples, we have not observed a vortex lattice [Fig. 2.7]. We suggest the formation of a vortex liquid, similar to that observed in other underdoped cuprates, including closely related compound $YBa_2Cu_4O_8$ [49].

Though we do not observe static vortices in Ca-doped YBCO, we observe that the gap fills slightly with increasing B-field [Fig. 2.8]. To the best of our knowledge, H_{c2} of 10% Ca-doped YBCO has

not been reported, so we have no good reference point for the expected behavior of the superconducting gap up to 9 T. In Ca-free YBCO, T_c is more sensitive to magnetic field at hole doping around $p = 0.12$ ($H_{c2} = 25$ T) compared to optimal hole doping $p = 0.16$ ($H_{c2} > 150$ T)[50,13]. However, this H_{c2} dip at $p = 0.12$ is attributed to competition from the incipient charge density wave, which has not been reported in 10% Ca-doped YBCO and which we do not observe in our sample [Fig. 2.1(d)]. More data on the high-B suppression of T_c in bulk Ca-doped YBCO are necessary to provide a point of comparison for our STM measurements of Ca-doped YBCO up to $B = 9$ T.

In summary, we study the effect of Ca-doping on the preferred cleavage plane of YBCO and characterize the resulting superconducting partial (Y,Ca) surface with STM. In alignment with prior work, our measurements of cleaved Ca-free, optimally-doped YBCO crystals show an electronic environment that is not representative of bulk and thus not compatible with the use of surface-sensitive techniques to study the nanoscale superconducting properties. However, when YBCO is doped with 10% Ca, crystals cleave to expose a partial (Y,Ca) surface that is consistent with bulk-like superconductivity. DFT calculations support the increased probability of this intra-(Y,Ca) cleavage plane in Ca-doped samples, relative to the commonly observed BaO-CuO cleavage plane in Ca-free samples, though the calculated relative energies of the different cleavage planes within a single sample do not align with experimental results. We use STM to study the superconductivity on the partial (Y,Ca) surface and find a superconducting gap of 24 ± 3 meV with length scale 1–2 nm, similar to that seen in Bi-based cuprates. Ours is the first report of spatial inhomogeneity of the spectral gap on YBCO compounds. Areas of opportunity for Ca-doped YBCO include cleaving at a lower temperature to achieve a more ordered surface, and imaging a Ca-doped compound with optimal hole concentration $p = 0.16$ to search for a vortex lattice. Our work opens the door for further study of the superconductivity in Ca-doped YBCO via surface-sensitive techniques like STM, and demonstrates the use of doping to modify the cleavage plane of crystals and reveal new surfaces of

interest.

2.3 Appendices

2.3.1 YBCO vs. BSCCO

YBCO commonly cleaves between the BaO square lattice and CuO chain planes, which intersects an internal dipole moment. In contrast, BSCCO commonly cleaves between two van-der-Waals-bonded BiO layers that have mirror symmetry. Thus BSCCO cleavage does not interrupt any dipole moments and allows the surface to retain bulk-like electronic properties. The comparison between YBCO and BSCCO cleavage is shown in Fig. 2.4.

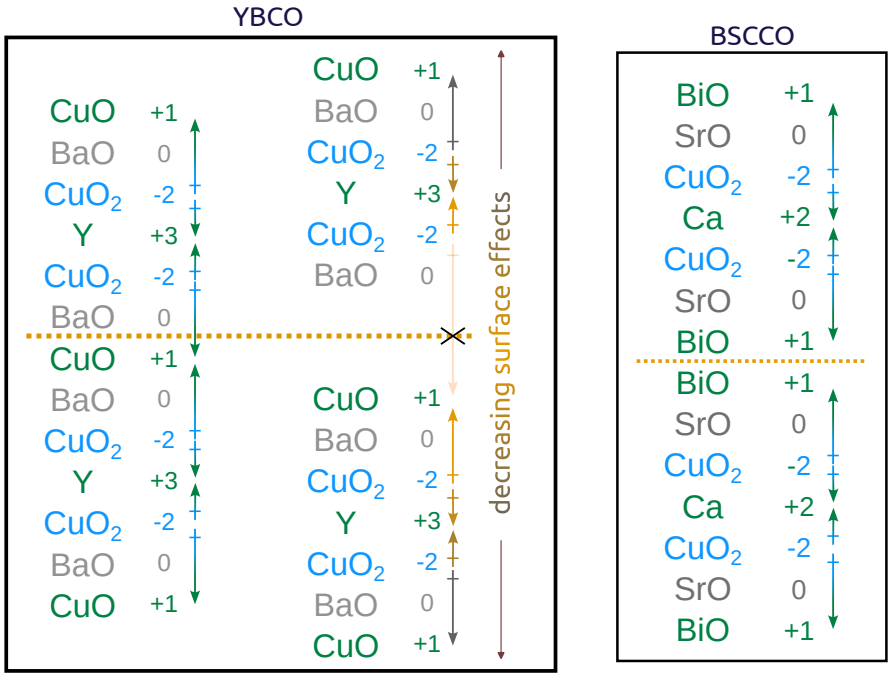

Figure 2.4: Schematic of the dipole moments and cleavage planes in YBCO and BSCCO.

2.3.2 Experimental characterization of Ca-YBCO

We performed STM experiments on two different cleaved $Y_{0.9}Ca_{0.1}Ba_2Cu_3O_{7-\delta}$ crystals from a single batch. Magnetic susceptibility measurements on a third crystal from the same batch showed a $T_c = 31$ K (Fig. 2.5). STM topographies over several hundred nanometer areas show flat but disordered surfaces, with no steps, valleys, or reconstructions on either of the two cryogenic cleaves (Fig. 2.6).

We track a single region of the cleaved Ca-YBCO surface as B is increased to 9 T in Fig. 2.7. Average spectra from this region, displayed in Fig. 2.8, show that the gap fills only slightly with increasing B.

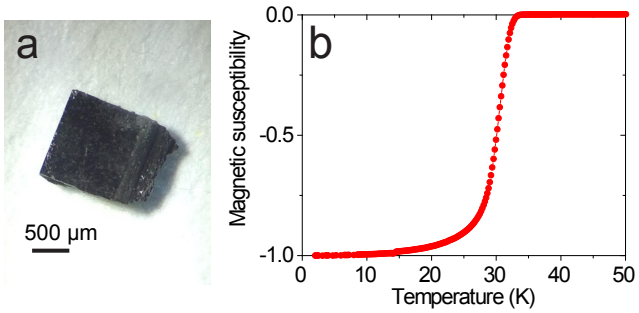

Figure 2.5: (a) Photograph of one of the Ca-YBCO single crystals from the same batch used in this study. (b) Magnetic susceptibility measurements of Ca-YBCO samples with $T_c \sim 31$ K determined as the peak in the first derivative of the susceptibility vs. temperature trace.

2.3.3 DFT Calculations

In our intra-(Y,Ca) cleavage calculations, the partial (Y,Ca) surfaces have ordering not present in our experimental results: all of the Ca-atoms end up on one of the two surfaces, and there is a 2×2 'stripe-like' supercell that we do not observe in our STM images on the partial (Y,Ca) surfaces (Fig. 2.9).

To study the effect of oxygen doping on the effect of Ca-doping, we calculate cleavage energies for $Y_{0.75}Ca_{0.25}Ba_2Cu_3O_6$ (Ca-YBCO6) in addition to the $YBa_2Cu_3O_7$ (YBCO7) and $Y_{0.75}Ca_{0.25}Ba_2Cu_3O_7$ (Ca-YBCO7) structures discussed in the main text. The bulk Ca-YBCO6 structure was taken from experiment[51] and differs from the Ca-YBCO7 structure in that the apical O is removed. In other words the 'CuO' planes become Cu planes, while the CuO_2 planes remain unchanged. Results of the cleavage calculation show that the trends discussed in the main text hold for both Ca-YBCO7 and Ca-YBCO6 (Table 2.1).

Table 2.1: Energy difference per atom (eV) for each structure and cleavage plane.

Cleavage plane	YBCO7	Ca-YBCO7	Ca-YBCO6
BaO-CuO	0.098	0.099	0.114
CuO_2-BaO	0.071	0.072	0.112
(Y,Ca)-CuO_2	0.265	0.234	0.251
intra-(Y,Ca)	0.174	0.164	0.166

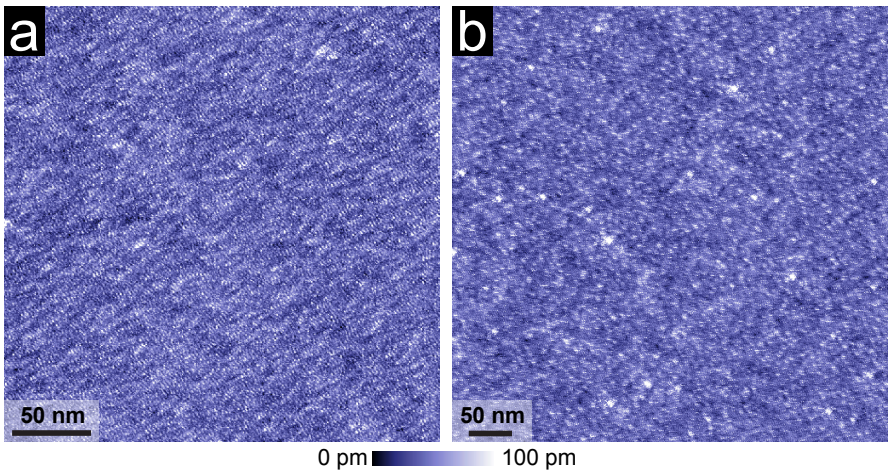

Figure 2.6: STM topographs of two different cryogenic cleaves of Ca-YBCO showing (a) ∼300 nm, and (b) ∼500 nm square regions of the sample. Setup condition in (a): $I_s = 10$ pA and $V_s = -500$ mV; (b) $I_s = 10$ pA, $V_s = -150$ mV.

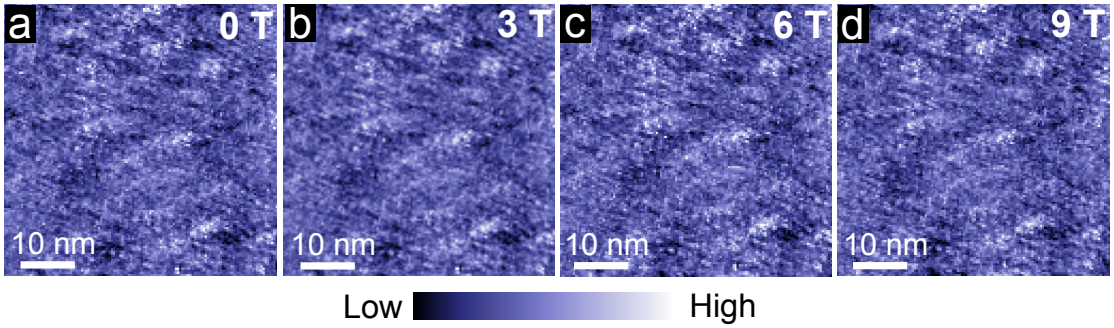

Figure 2.7: Topographs over the same region of the sample acquired at (a-d) 0, 3, 6, and 9 T magnetic fields respectively.

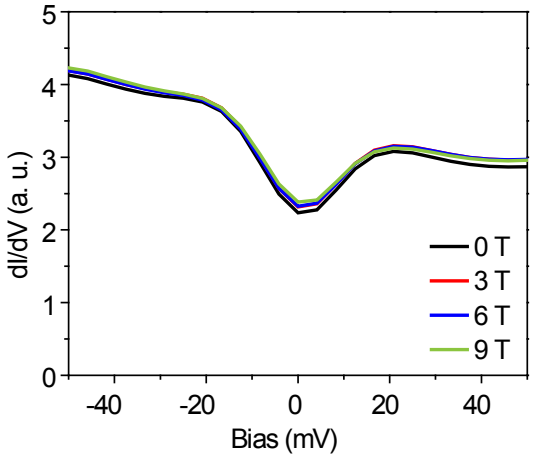

Figure 2.8: Average dI/dV spectra obtained over the region shown in Fig. 2.7. The Fermi-level gap fills only slightly with application of magnetic field up to 9 T.

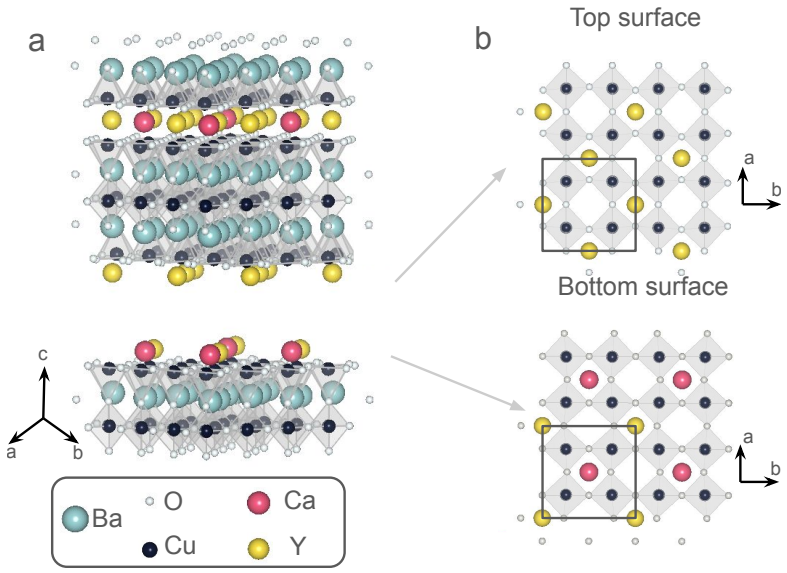

Figure 2.9: (a) Side view of the intra-(Y, Ca) cleavage planes and (b) top view of the two resulting partial (Y,Ca) surfaces with black square showing the DFT supercell.

Part II: Barium titanate thin films for electro-optics

3

Barium Titanate for Integrated Photonics

Demand for high performance materials for photonics has risen drastically with the increase in light-based data transfer, sensors, computation, and even quantum network applications. Currently, $LiNbO_3$ is the ubiquitous material of choice for electro-optic applications, with an electro-optic coefficient of 31 pm/V[52]. Generally the cited electro-optic coefficient, also called the Pockels coefficient or r, is the electro-optic tensor value with the highest value, which in the case of

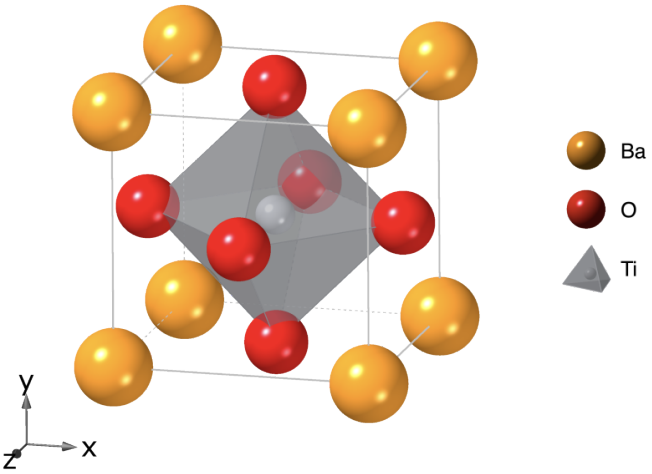

Figure 3.1: Crystal structure of $BaTiO_3$.

$LiNbO_3$ is r_{33} (for a more detail on the electro-optic tensor, see Chapter 5.3.3). Recent work has demonstrated that electro-optic modulators made with integrated photonics, as opposed to bulk materials, have improved performance [52]. Integrated $LiNbO_3$ modulators have lower power requirements as well as lower half-wave voltage-length products ($V\pi L$), a common performance metric for electro-optic modulators that is defined as the voltage required to to shift the output phase of light moving through the modulator by π radians multiplied by the length of the phase shifter. As integrated photonic devices become more dominant in industry, there has been renewed interest in pushing the design to achieve even higher performance, and a natural next step is to look for promising materials that could replace $LiNbO_3$ as the electro-optic material of choice.

Since any crystal that lacks inversion symmetry may have non-zero electro-optic tensor components, possible material options are myriad. However, although many materials are allowed to have a non-zero electro-optic response, predicting which materials will have a *strong* response is not straightforward. Effective methods and improved heuristics for predicting strongly electro-optic materials is an area of active research [53].

Even once a strongly electro-optic material has been identified, our task of finding a material that improves upon $LiNbO_3$ in a meaningful way is not complete. In fact there are many material options that have been experimentally confirmed to have much higher electro-optic tensor components[54,53], yet $LiNbO_3$ remains the pervasive choice of the moment. Why is this?

For use in a practical integrated photonic device, materials must not only be strongly electo-optic, but also perform well in several other design requirements and metrics. For example, materials would ideally have a Curie temperature of many hundred degrees Celsius, far above processing temperatures required to fabricate photonic devices. If an electro-optic component is heated and then cooled through the Curie temperature, its ferroelectric domain polarization, which must be carefully controlled to achieve the strongest electro-optic response, will be lost. Materials would also ideally have a relatively low dielectric constant so that an electrical field can be effectively applied, be relatively straightforward to synthesize, and have a wide transparency window to minimize losses. Though this is only a partial list of design considerations, it is clear that one must consider any material candidate more holistically than merely looking at its r value. In most of these metrics, $LiNbO_3$ performs well, with a Curie temperature of 1200°C, dielectric constant of 29, a bandgap of 3.6 eV, and a synthesis process that can be scaled up to produce boules of several inches in diameter. Finding a material that is an overall improvement on $LiNbO_3$ is thus not as straightforward as it first appears.

Several groups over the last decade or so have identified $BaTiO_3$ as a promising material and have published results that show effective electro-optic coefficients of thin film $BaTiO_3$ waveguides anywhere from 140 to 923 pm/V[55,56,57,58]. In bulk, it has an electro-optic tensor component r_{42} = 1300 pm/V. The optical bandgap of thin film $BaTiO_3$ is measured to be anywhere from 3.2 to 3.7 eV (about 340 to 390 nm), on par with that of $LiNbO_3$ [59,60]. $BaTiO_3$ has the additional advantage of being materially compatible with silicon foundries, while lithium niobate is not due to the high mobility of lithium and its poisoning effect on semiconductor devices[58].

With so many advantages, one may wonder why $BaTiO_3$ is not *already* more widely used commercially. In bulk, $BaTiO_3$ has a Curie temperature of only $130°C$, and shatters easily when temperature cycled (so much so that $BaTiO_3$ crystals are generally shipped in a special box that contains battery-powered temperature control to prevent cracking). Of course, this prevents $BaTiO_3$ from being reasonably used in commercial discrete photonic components that require large crystals of electro-optic material. Additionally, the dielectric constant along the relevant crystallographic axes of $BaTiO_3$ is around 3500 at room temperature — around two orders of magnitude higher than $LiNbO_3$ [61]. Thus, $BaTiO_3$ only becomes a viable candidate in thin-film form.

In the following chapters, I hope to add to the body of work on $BaTiO_3$ with a focus on the practical aspects of film growth and properties that are important for realizing its promise for integrated photonics.

4

Effects of Stoichiometry in Barium Titanate

The quantitative chemical composition, or stoichiometry, of a material can dramatically alter its functional properties. As described in Chapter 3, there are a number of properties that must be considered when evaluating the suitability of thin films for integrated photonics. Thus, understanding how stoichiometry affects $BaTiO_3$ film growth and resulting properties is a critical aspect our research efforts. For some material-application pairings, 10% stoichiometry control may be suf-

ficient. For other pairings, such as in the semiconductor industry, control over stoichiometry down to trace amounts is critical. Molecular beam epitaxy (MBE) is a technique well suited to study the effects of stoichiometry on the crystalline structure and performance of thin films, as it allows for stoichiometric control within a thin film of around 1%[62,63]. This tight control results from MBE being a relatively slow, low-energy technique, as well from the ability to shutter individual elements so each monolayer of a film may be deposited with precise timing.

Given the differences in surface kinetics and control variables between film synthesis methods, there may be some variation the types of defects that appear in off-stoichiometry films between MBE and other methods such as pulsed laser deposition or sputtering. Nevertheless, the overall performance of off-stoichiometric films grown via MBE is a useful metric for evaluating the sensitivity of a material's performance across its compositional phase diagram.

Additionally, mapping out a well-characterized 'stoichiometry series' for a material and identifying figures of merit is useful for efficient film growth. Although MBE-grown films are generally very repeatable when grown one after another, entropy wins in the end. Invariably, settings such as effusion cell temperature must be adapted as source material is used up, refilled, exposed to high pressures during chamber maintenance, when effusion cell design changes, when elements locations within the chamber are swapped, etc. Being able to repeatably and accurately estimate the stoichiometry of a film from on-site, quick, and nondestructive characterization techniques is a valuable time-saver when re-optimizing growth conditions.

A good starting point for understanding the tolerance of a compound to stoichiometry changes is the compositional phase diagram. We can consider the BaO-TiO_2 phase diagram in Figure 4.1. Below around 1000°C $BaTiO_3$ is nearly a line compound, meaning that at those temperatures even <1% of excess Ba or Ti in a bulk crystal will form a secondary phase as opposed to being incorporated via defects into the bulk $BaTiO_3$ phase. Though the solubility of excess Ba and Ti are both low, $BaTiO_3$ can accommodate around double the amount of excess Ba than Ti[65]. As excess

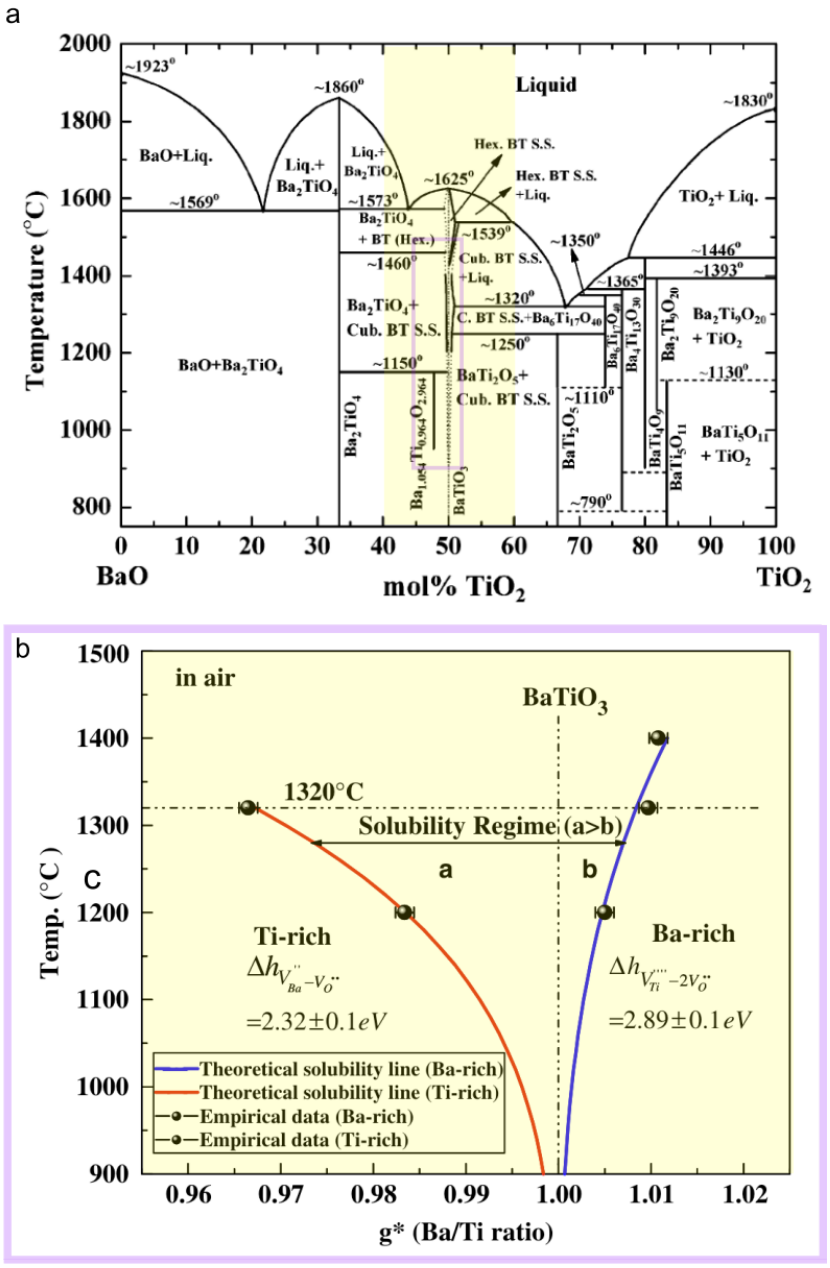

Figure 4.1: (a) Binary phase diagram at high temperatures of BaO-TiO_2 compounds, adapted from Lee et al.[64]. Stoichiometry range of films grown in this chapter highlighted in yellow and the area covered in (b) shown a in pink square. (b) Calculated and experimental solubility limits.

Ba is introduced, at higher temperatures an off-stoichiometric compound $Ba_{1.054}Ti_{0.964}O_{2.964}$ forms[64,66]. At lower temperatures excess Ba forms Ba_2TiO_4, which is not a Ruddleston-Popper type compound, unlike the Sr_2TiO_4 which can form in the case of SrO-TiO_2. On the Ti-rich side, $BaTiO_3$ forms a solid solution with $BaTi_2O_5$.

While this phase diagram is a useful starting point, it is important to note that bulk phase diagrams do not give us all the information we need to understand how off-stoichiometry thin films will form for several reasons. Firstly, the phase diagram does not specify the how defects will form within a single crystallographic phase to accommodate any off stoichiometry. This information is important to understand the effect of the defects on the final properties of interest. Secondly, a bulk phase diagram is only valid in the thermodynamic limit. In thin film growth kinetics plays an especially important role as surface diffusion determines the growth mode and can even affect the quality and phase of film that grows[67]. Finally, meta-stable phases of materials can be achieved in thin film form that do not occur in bulk and thus would never appear in a thermodynamic phase diagram.

Here we vary the composition of 10 nm $BaTiO_3$ films grown on $SrTiO_3$ substrates. This allows us to explore the 'off composition thin film phase diagram,' characterize the types of defects and phases that are stabilized in off-stoichiometric films, and identify metrics that can be used as diagnostics for future film growths.

A thickness of 10 nm was chosen because the films should be fully strained to the $SrTiO_3$ substrate (-2.32% strain), which will allow us to focus on defects that form in the crystal structure due to non-stoichiometry as opposed to defects that form to relax strain when the film thickness exceeds the critical thickness for relaxation on the substrate.

Fazlioglu-Yalcin et al. have published similar work with $BaTiO_3$ films grown via hybrid MBE, (as opposed to conventional MBE)[68]. In that work films were are grown on $(LaAlO_3)_{0.3}(Sr_2TaAlO_6)_{0.7}$ (LSAT) substrates, and the effects of off-stoichiometry on the 002 peak in XRD, the crystal struc-

ture via STEM, and the optical properties of the films are explored[68].

4.1 Growth Methods

Films are roughly calibrated first with a quartz crystal monitor (QCM), then with reflection high energy electron diffraction (RHEED) shutter oscillations[62]. We cover a stoichiometry range of $\pm 10\%$. All films were grown by shuttering Ba and Ti one monolyaer at a time as opposed to co-depositing. Stoichiometry is controlled by changing the time each element is deposited. The overall dose of atoms deposited was kept constant, only the ratio of Ti and Ba was changed via shutter time. The sticking coefficient for Ba and Ti is assumed to be one, in other words, it is assumed that every atom that lands on the film surface will be incorporated into the film in some fashion.

All films were grown with conventional MBE. To oxygenate the films, we use an approximately 80% ozone, 20% oxygen mixture at a pressure of 5×10^{-8} Torr, controlled by a piezoelectric leak valve and supplied by a Heeg Vacuum Engineering distilled ozone system. We prevent any reduction post-growth by cooling the films to 250°C or colder in the same environment. Films were grown at a temperature of 600-630°C as measured by the in-situ thermocouple and 723-752°C as measured by the in-situ Fluke Endourance infrared pyrometer with 1 μm spectral response. Samples were silver pasted with PELCO® High Performance Silver Paste to a Haynes 214 platen. Ba flux was 0.79×10^{13} atoms/(cm^2·s) and Ti flux was 0.87×10^{13} atoms/(cm^2·s). All films are grown to be 10 nm on $SrTiO_3$ substrates. Films are cooled in the presence of the distilled ozone.

Substrates are prepared by cleaning with Micro 90 soap, DI water, acetone, then isopronanol for 5 minutes each, then etching in DI water held at 60°C for 30 minutes, and finally annealing in air at 1000°C for 4 hours. This produces $SrTiO_3$ substrates with an atomically smooth surfaces with unit cell step height terraces.

We identify the film with highest quality in RHEED, XRD, and STEM and label this film 'sto-

ichiometric'. The six films discussed in this chapter were grown sequentially within a period of 24 hour without cooling the elemental sources.

4.2 Effects of Stoichiometry on Structure and Surface

4.2.1 RHEED Characterization

During growth, the samples are characterized through RHEED, shown in Figure 4.2. Based on the RHEED images, it is easier to distinguish Ba-rich samples from the Ti rich samples through the formation of what appears as a secondary phase. All the Ba rich samples show characteristic spots with a slightly larger lattice constant than than of the $BaTiO_3$ film, which appears as streaks. Even 2.5% excess Ba shows up in RHEED. On the other hand it is more difficult to tell when a sample is Ti rich by RHEED since the film remains high quality and smooth, as indicated by clear streaks. However there are tell-tale sign of the the Ti-rich nature of the films. In the nominally stoichiometric film and the 5% rich Ti film, a 1/2 order reconstruction appears in the film (very faint in the stoichiometric [100] azimuth). When the film becomes 10% Ti rich, a 1/3 order reconstruction appears. Based on the RHEED it is challenging to distinguish between the 5% Ti rich and the nominally stoichiometric films.

4.2.2 X-ray Diffraction Characterization

After growth samples were characterized with X-ray diffraction (XRD), performed with a Malvern Panalytical Empyrean diffractometer using Cu Kα radiation. A wide-range 2-θ scan that shows the 001, 002, 003, and 004 film reflections is shown in Figure 4.3a. All films show thickness fringes around the 001 reflection. The nominally stoichiometric film also has thickness fringes around the 002 reflection, as does the 5% Ti-rich film, although they are less pronounced. All of the off-stoichiometric films show less intense 003 and 004 reflection compared to the nominally stoichio-

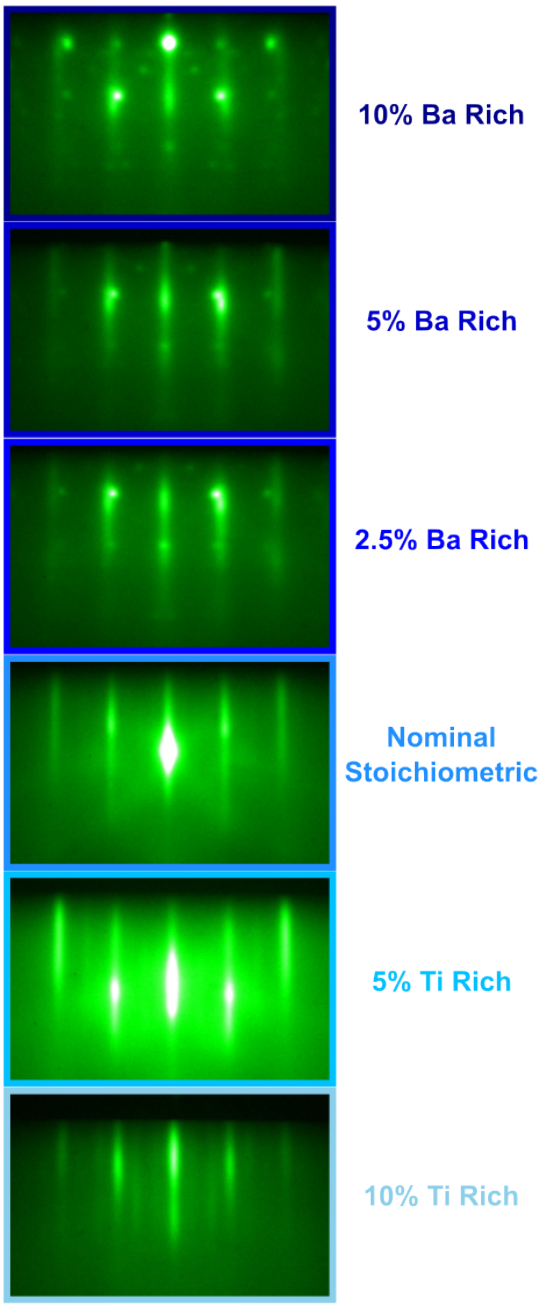

Figure 4.2: RHEED images obtained during growth for the stoichiometry series along the [100] azimuth of the films. Images are obtained near or at the end of film growth but before the samples are cooled. Ba-rich samples show a characteristic secondary phase, which Ti rich samples appear smooth. The 10% Ti rich sample shows a 1/3 reconstruction, while both the 5% Ti and nominally stoichiometric show a 1/2 reconstruction (faint for the nominally stoichiometric sample).

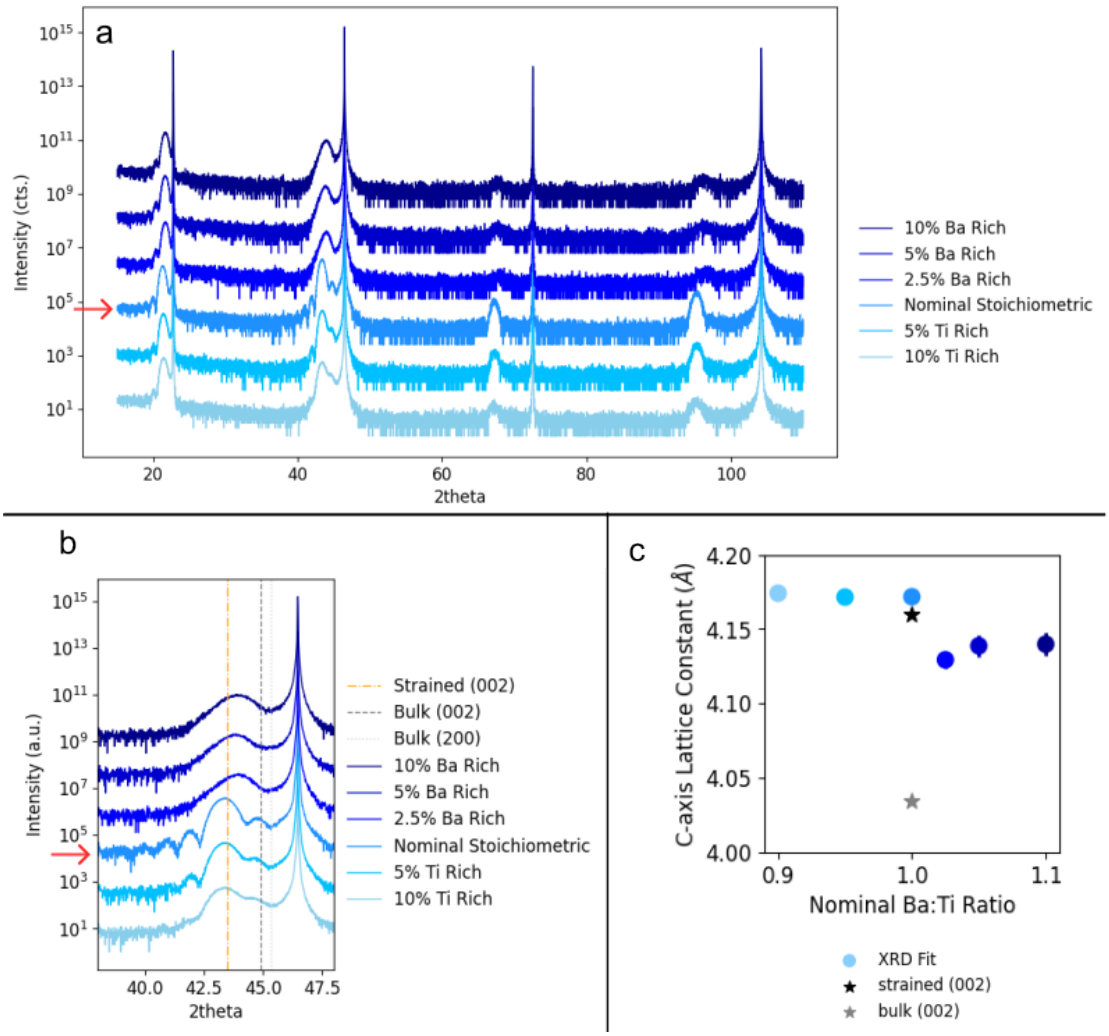

Figure 4.3: (a) wide range 2θ scan of the out-of-plane film peaks of the series. Note that the small peaks that appear at 38.6 in some of the samples are [111] reflections from the Ag paste used to secure the sample during growth. (b) zoom in on the 002 peak of the films. Ti-rich films align well with the position of the a fully strained film on $SrTiO_3$ while the Ba-rich films show a 2θ value between a fully strained film and a relaxed film. (c) c-axis lattice constants derived from the 001, 002, 003, and 004 film peaks, which align with the trends shown in (b).

metric film, with the decrease in intensity more dramatic in the Ba-rich films than the Ti-rich films.

Focusing on the 002 reflection, as shown in Figure 4.3b, we can compare the peak locations to reference lines of the bulk/relaxed 002 location, the bulk/relaxed 200 location, and the calculated 2θ value of a $BaTiO_3$ film fully strained on an $SrTiO_3$ substrate. This value is calculated using the three-dimensional isotropic strain tensor relations[69], which yields:

$\varepsilon_{33} = [\varepsilon_{22} + \varepsilon_{11}] \times -\nu/(1-\nu)$

ε_{33} is the out-of-plane stain, ε_{22} and ε_{11} are the in-plane tensor components (equivalent in this case as $SrTiO_3$ is isotropic in-plane), and ν is the Poisson's ratio, 0.4 for $BaTiO_3$[70].

When compared to these reference 2θ values, we can see that the nominally stoichiometric film peak is very close to the strained value. In the Ti rich samples, the primary peak also lies very close to the strained 002 value, but as the Ti concentration increases the intensity of a secondary peak with a smaller c-axis constant also increases, which could corresponds with some amount of relaxation toward the bulk 002 value within the film. The Ba-rich films have a lower overall crystalline quality based on the lack of peak intensity and thickness fringes for even the 2.5% of Ba-rich film. All of the peaks seem to be around the same 2θ value, which is higher than the calculated strained 002 position, corresponding to a lower lattice constant. The peaks are still above the relaxed c-axis lattice constant, indicating some amount of strain.

To extract the lattice constant of the films, we use the fitting method proposed by Nelson and Riley[71]. This method accounts for physical and geometric sources of error that occur when determining lattice constant from a single film peak, and instead uses the location of all measured film peaks. The extracted lattice parameters from the stoichiometry series can be seen in Figure 4.3c. As expected, we can see that the the nominally stoichiometric and the Ti-rich samples have a lattice constant that does not vary much and is close to the calculated strained lattice constant. The lattice constant of the Ba-rich films also does not vary much with changing concentrations of Ba, and in all cases is lower than the fully strained lattice constant but higher than the bulk value. Note that due

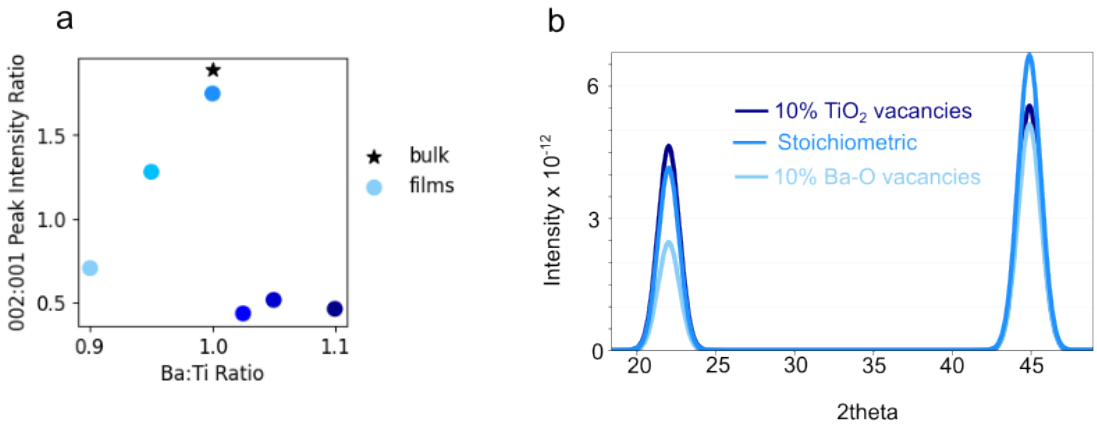

Figure 4.4: (a) ratio of the 002:001 peaks from scan shown in Figure 4.3a. The nominally stoichiometric film has a ratio close to bulk values. With increasing Ti, the 002:001 ratio gradually decreases. With excess Ba, there is a dramatic decrease in the 002:001 ratio, which then does not change significantly with more Ba excess. (b) Model created with CrystalDiffract of the 001 and 002 $BaTiO_3$ peaks with partial Schottky defects of either Ti-O—2 or Ba-O. The does not align well with the experimental results, indicating that these partial Schottky defects are insufficient to explain the intensity ratio changes the data show.

to the film's orientation only the out-of-plane lattice constant can be calculated from these diffraction scans.

Another possible figure of merit for determining film stoichiometry is the ratio of the 002 and the 001 peak, shown in Figure 4.4a. In bulk, the 002 peak is nearly twice as intense as the 001 peak, similar to what we see in the nominally stoichiometric film. For Ti-rich films, the 002:001 ratio seems to decrease linearly between. For Ba-rich films, the 002:001 ratio is lower than for any of the Ti-rich films and remains nearly constant through the stoichiometry range explored.

Based on prior work in bulk systems, non-stoichiometric films of $BaTiO_3$ form partial Schottky defects, where a cation vacancy of either Ba or Ti will stabilize one (in the case of Ba) or two (in the case of Ti) anion O-vacancies in order to balance the overall charge of the crystal, even in an environment with sufficient oxidative power[65].

$\varnothing \rightleftharpoons v''_{Ba} + v''''_{Ti} + 3v^{\bullet\bullet}_{O}$ Full Schottky defect in $BaTiO_3$

$\varnothing \rightleftharpoons v''''_{Ti} + 2v^{\bullet\bullet}_{O}$ Partial Schottky defect in Ba-rich $BaTiO_3$

$\varnothing \rightleftharpoons v''_{Ba} + v^{\bullet\bullet}_{O}$ Partial Schottky defect in Ti-rich $BaTiO_3$

Although both Ti-vacancies and equatorial oxygen vacancies do decrease the 002:001 ratio, the trend seen in the XRD data cannot be fully explained solely by the effect of site-occupancies on the peak intensity. To model these partial Schottky vacancies, we used CrystalDiffract to model a film with a thickness of 5 nm. For the TiO_2 partial Schottky defects, the Ti occupancy was adjusted to 0.9, and the equatorial O occupancy to 0.9 as there are two equatorial O's per Ti atom. For the BaO partial Schottky defects, the Ba occupancy was adjusted to 0.9 and the equatorial O occupancy to 0.95. Results are shown in Figure 4.4b. Notably, Ba vacancies do not decrease the 002:001 peak ratio, though the data for Ti rich films show a decrease in this ratio. Additionally, increasing the TiO_2-partial Schottky defects should gradually decrease the 002:001 peak intensity, and even at 10% the model does not show a 002 peak that is less intense than the 001 peak. This is in contrast to the stable ratio 0.5 002:001 ratio seen in Ba-rich films. The inconsistency between this vacancy-based model and experimental results may be due to the limitations of the model, which neither accounts for the effect of strain on the atomic position of the Ti atom in the unit cell, nor for any interstitial atoms that may occur in off-stoichiometry films.

Despite the lack of clarity about the mechanism by which this change in peak intensity arises, the clear trend for off-stoichiometry films is a useful metric for diagnostics of film quality.

4.2.3 Reciprocal Space Mapping

Another X-ray diffraction technique that can be used to extract the in-plane as well as out-of-plane lattice parameters of a film is reciprocal space mapping. Here we use the same X-ray diffractometer described above using a two-dimensional pixel detector (PIXcel3D). In this technique, the X-ray diffractometer scans with $\theta \neq \omega$ over a range of 2θ and ω ranges. The out-of-plane axis is carefully leveled with respect to the X-ray beam, and the sample φ position is aligned to a high symmetry crystallographic angle of choice. Ideally, an area of reciprocal space where both a substrate and a film

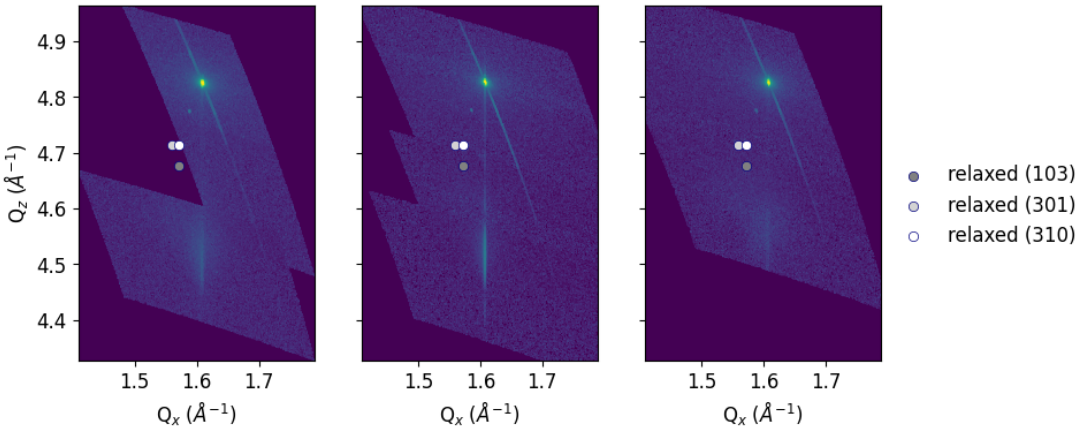

Figure 4.5: Reciprocal space mapping of the [-103] film and substrate peaks for the 10% Ti-rich film (left), nominally stoichiometric film (center), and 5% Ba-rich film (right). The Ti-rich and nominally stoichiometric are strained to the $SrTiO_3$ substrate in the x-axis, while the 5% Ba-rich film peak is much fainter and shows relaxation towards the bulk value.

peak appear would be mapped out in order to check if the film is coherently strained to the substrate. In the case of $BaTiO_3$ on $SrTiO_3$, we scan around the film and substrate ($\bar{1}03$) peaks, shown in Figure 4.5. Since the range of reciprocal space we are looking over is large several scans are stitched together. The $SrTiO_3$ ($\bar{1}03$) peak appears with lattice constants of a = c = 3.905Å in line with bulk values. The film peaks appears as a streak because the film experiences dimensional confinement in the out-of-plane, c-axis, direction but not in the in-plane, a-axis, direction. For comparison, the calculated fully strained and bulk (fully relaxed) values are plotted.

The a-axis lattice constant of the 10% Ti-rich film is directly in line with the lattice constant of STO. This indicates that the film is fully strained in-plane. This is also the case for the nominally stoichiometric film, where the peak shows even less relaxation in the a-axis direction. Above and below the main peak, fringes can be seen in the c-axis direction. The 10% Ba-rich film, on the other hand, is much less coherent in the a-axis and shows relaxation in both the c- and a-axes, in line with the XRD results.

4.2.4 Atomic Force Microscopy Characterization

Atomic force microscopy (AFM) is conducted after film growth to analyze the film surfaces in real space. Images of the 10% Ba rich, nominally stoichiometric, and 10% Ti rich samples are shown in Figure 4.6.

The results of AFM align well with the expected results based on RHEED, which is also a surface sensitive technique. Both Ti-rich and nominally stoichiometric films are relatively flat with low surface roughness. In both cases, the underlying substrate terraces have templated the film growth and are visible in the images. The 10% Ba-rich sample has a very different surface morphology, with bumpy island-like features that are about an order of magnitude taller than any of the features in the other films and of similar magnitude to the overall expected thickness of the film. These islands are on the order of around 10 nm in diameter.

4.2.5 Scanning Transmission Electron Microscopy Characterization

To further characterize the types of defects that form with off-stoichiometry, we use scanning transmission electron microscopy (STEM) to take real-space, atomic-resolution images of the films. These studies are able to identify defects such as grain boundaries, antiphase boundaries, stacking faults, twin boundaries, and edge dislocations, as well as any areas of atomic disorder.

Cross-sectional STEM specimens were prepared using an FEI Helios 660 focused ion beam (FIB) at 30 keV with a final thinning step at 2keV. HAADF- and ABF-STEM was performed using an aberration-corrected Thermo Fisher Scientific Themis Z G3 aberration-corrected STEM oper- ated at 200kV.

Results of the STEM study is shown in Figure 4.7. In all cases, the interface between the film and substrate appears atomically precise with little to no intermixing of the A site Ba- and Sr- atoms. The nominally stoichiometric film is very high quality, with only one clear edge dislocation in the 1

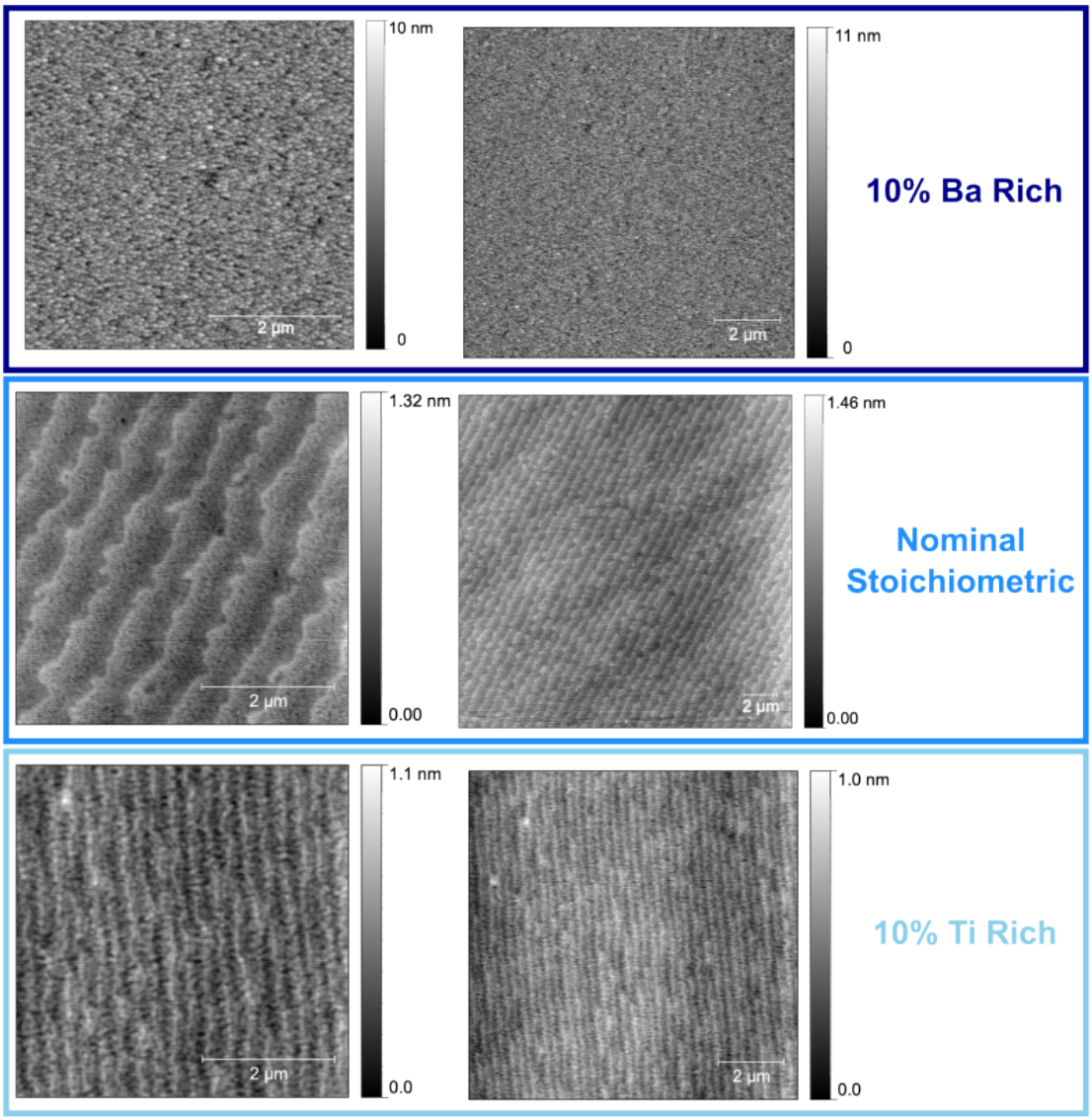

Figure 4.6: Atomic force microscopy of the films, 5 μm scans (left) an 10 μm scans (right). The nominally stoichiometric and 10% Ti rich films are both relatively smooth, while the 10% Ba rich film is a rough, island-like surface.

μm area studied. The surface is also flat to within one atomic plane. The 10% Ti rich films shows a high number of defects and areas where the atomic columns are not in good alignment.

Interestingly, the Ba-rich film does not show specific Ba inclusions. Instead the film shows a phase with relatively similar quality to the nominally stoichiometric film. However, there is significant surface roughness across the 1 μm area scanned. We know from the RHEED images that there is a rough secondary crystalline phase that forms during growth, but we do not see any sign of this in STEM. Instead, there appears to be about 2 nm of an amorphous phase between the film and the Pt. Interestingly, the 10% Ba rich sample undergoes dramatic beam damage near the surface in a matter of minutes. Three scans over the same area spaced about 2 minutes apart are shown in Figure 4.8. In each image, the purple arrow points to the same point on the film. In the 6 minutes that pass between the initial and final image, the area above the defect and the area along surface of the film becomes undergoes significant amorphization. This may indicate that the excess Ba, instead of being incorporated into the film, as the excess Ti is, phase separates and rises to the surface of the film. There are many Ba-based oxide compounds that are not stable upon water exposure such as BaO, BaO_2, $BaCO_3$ and $Ba(OH)_2$. One of these phases may crystallize during film growth, but become amorphous when exposed to atmosphere. Given that the secondary phase is crystalline during growth but does not remain crystalline between unloading and the STEM analysis, we deem it unlikely that the phase is crystalline $BaTi_2O_4$ as suggested by the phase diagram, which we would expect to be air stable.

4.3 Treatment of Ba-rich Samples with DI Water

To further explore this possibility, Ba-rich samples are soaked in DI water, which should not affect the $BaTiO_3$ film but would affect the water-sensitive phases discussed above.

Results of the DI water soak can be seen in Figure 4.9. After soaking in DI water, the surface of

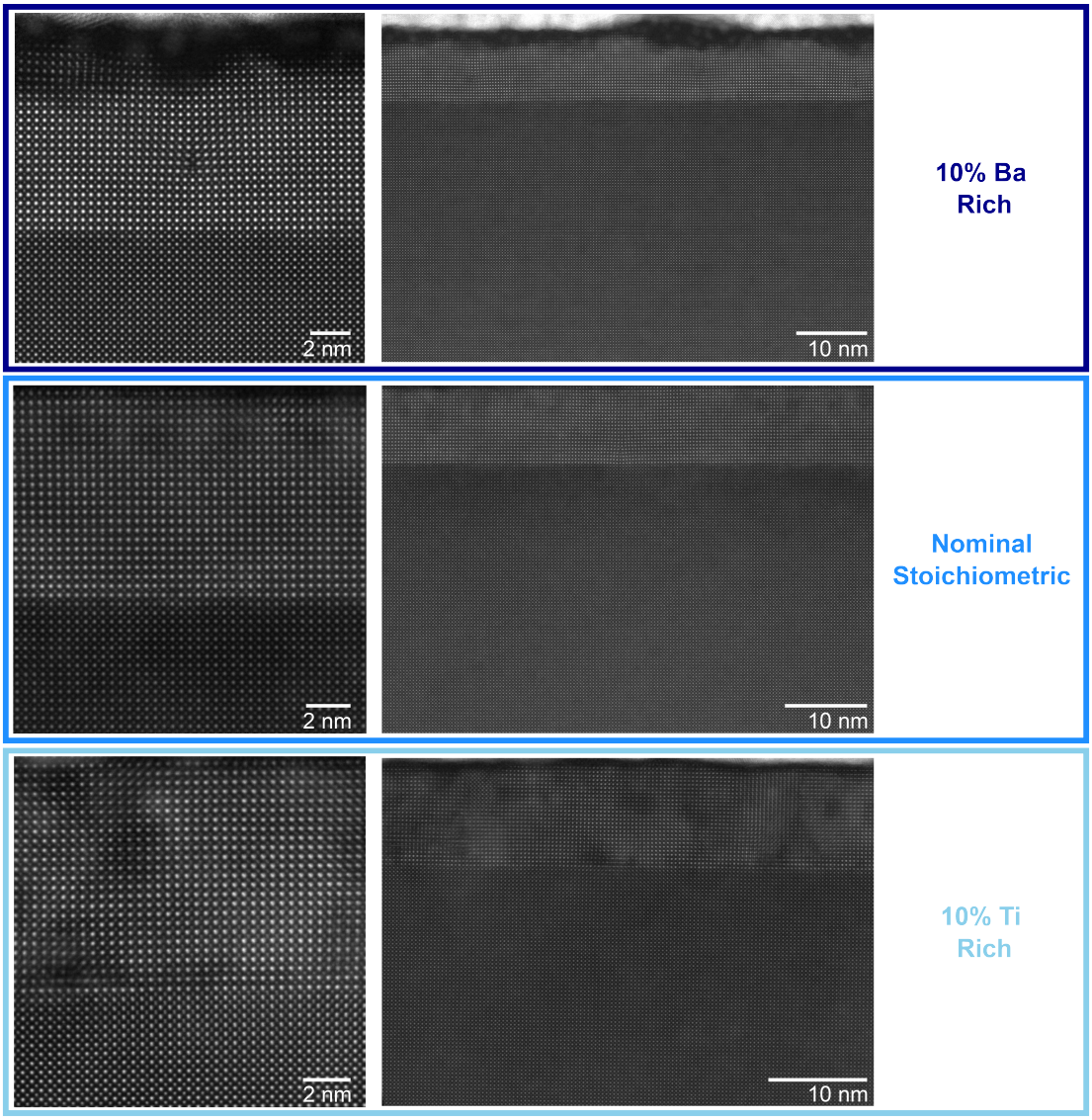

Figure 4.7: Smaller scale (left) and large scale (right) scanning transmission electron microscopy cross section images of films. The film appears at the top of the image, with sputtered platinum on top of the film. The $SrTiO_3$ substrate appears slightly darker due to the lower atomic weight of Sr compared to Ba.

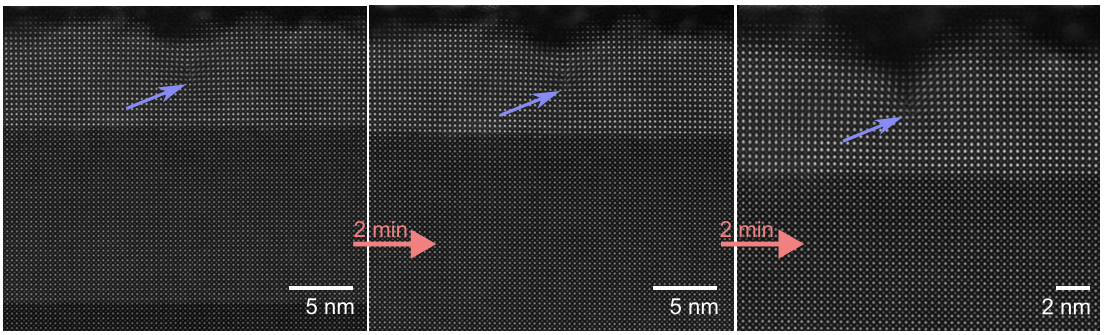

Figure 4.8: Time series of STEM images on the 10% Ba-rich sample, with approximately 2 minutes between each image. The purple arrow points to same edge defect in all images. Over time, amorphization of the film takes place above the defect and along the surface.

the Ba-rich films becomes much smoother and the terraces structure templated by the substrate is visible on the film surface. The post-water-treatment film surface is fairly comparable to the Ti-rich and stoichiometric film surface, although it seems slightly less smooth on each individual terrace. XRD after water treatment does not show significant changes (not shown). This procedure was done on both the 10% and 5% Ba-rich films with similar results.

After the water treatment, the 10% Ba-rich film was treated with an anneal of the same temperature and time as the $SrTiO_3$ substrate treatment (1000°C for 4 hours in air). AFM and XRD results after the anneal are shown in Figure 4.9 c,d,e. The anneal drastically changes both the surface and crystalline nature of the $BaTiO_3$ film. Instead of a smooth surface, there are tall, >100 nm $\times$ 0.5 μu islands with partial coverage of the surface. Due to the density and height of the islands, the nature of the surface between the islands cannot be resolved well. Additionally, the out-of-plane lattice constant has significantly reduced from 4.14 Å to 4.0 Å. This value is even lower than the 4.03 Å bulk c-axis lattice constant of $BaTiO_3$, so it is possible that the orientation of the $BaTiO_3$ has changed, or there may have been Sr diffusion into the $BaTiO_3$, which would also lower the lattice constant.

The effect of the water treatment on Ba-rich films raises the interesting question of if one could grow off-stoichiometry, soak the film in water to rinse off the Ba excess, and then treat the film via an

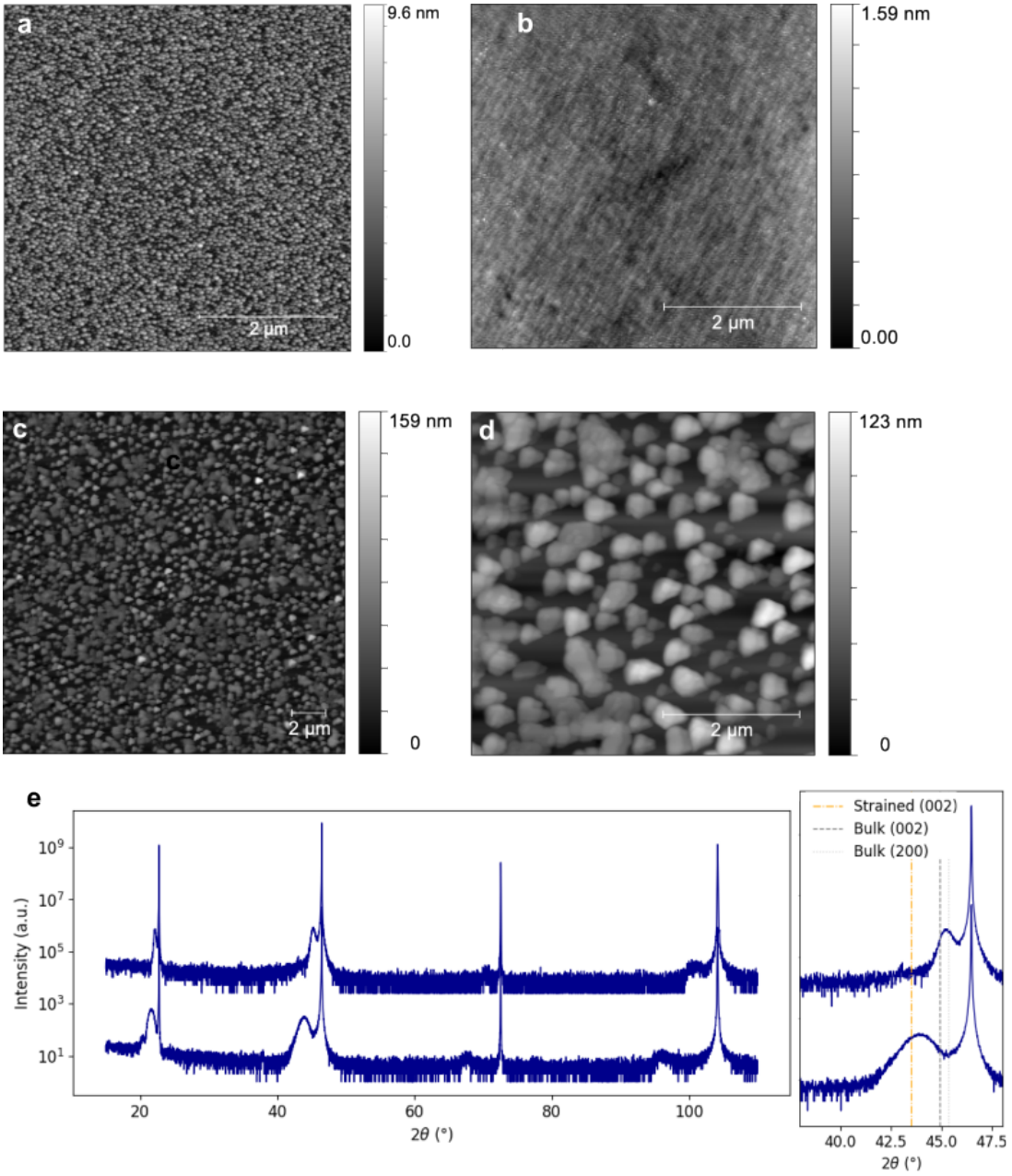

Figure 4.9: Changes of the Ba-rich sample with water and annealing treatment. AFM of the 5% Ba-rich sample before (a) and after (b) being treated with DI water. These results were replicated with the 10% Ba-rich sample. (c,d) AFM of the 10% Ba-rich sample after both DI water treatment and a 4 hour 1000°C anneal. (e) XRD comparison of the 10% Ba rich sample after growth versus after subsequent DI water and annealing treatment.

anneal near growth temperature to reconstruct the film to a flat surface. However, this test was only done on thin samples of $BaTiO_3$. It is possible that for thicker films, this non-stoichiometric layer would build up and would no longer form stoichiometric $BaTiO_3$ below the layer of BaO. It is also true that based on the XRD analysis, the remaining film is not as high of quality as the nominally stoichiometric film.

4.4 Discussion

In comparison to the bulk phase diagram, our results indicate that thin films can accommodate a higher percentage of excess Ba and Ti than can bulk crystals. We find that excess Ti creates defects and disruption of crystalline order in a way that is proportional to the amount of excess Ti in the film, for example 5% excess Ti causes fewer defects than 10% excess Ti but more than 2% excess Ti. Although not explicitly tested in this work, Ti-rich films of $BaTiO_3$ are electrically lossy and so unsuitable for photonics applications[68].

On the other hand, the Ba-rich films show very different trends. Even small amounts of additional Ba have a dramatic effect on the overall crystal structure and film surface but adding a greater amount of excess Ba does not seem to make a big difference in terms of defects and crystalline order. Across the range of 2.5% to 10% excess Ba, the lattice constant doesn't change, nor does the 002:001 reflection intensity ration. STEM imaging of the 10% Ba-rich film doesn't show clear defects in the majority of the film, only near the surface. Taken together, our results imply that excess Ba could acts as a 'flux' during film growth that rises to the surface of the film and forms BaO or BaO_2 on the film surface. Both of these compounds decompose in air, as do the carbonized and hydrolysed compounds $BaCO_3$, $Ba(OH)_2$, and would thus become amorphous once the film is unloaded from the UHV environment. This interpretation aligns well with the large amount of amorphous compound we see in STEM at the surface of the Ba-rich film, with the rough surface seen in AFM, and with the

improved surface seen after DI water treatment. While the phase diagram suggests the formation of Ba_2TiO_4 or $Ba_{1.054}Ti_{0.964}O_{2.964}$, both of these compounds are air stable, and we do not see any signs that either of these compounds are forming[66].

Our results have the interesting implication that while Ti-rich films should be avoided for photonic applications, it is possible that Ba-rich films may be post-treated with water to recover high quality $BaTiO_3$. Further work is needed to test if this strategy scales to much thicker films and to test if water-treated Ba-rich films have degraded optical properties compared to stoichiometric films.

5

Effects of Strain on Barium Titanate

There have been both computational and experimental indications that strain could significantly enhance the electro-optic effect in barium titanate[72]. Prior work has shown that strain in $BaTiO_3$ thin films can result in a 2.5× enhancement in the polarization of $BaTiO_3$ thin films on $DyScO_3$ substrates, increase the Curie temperature by hundreds of degrees[73], and enhance the second harmonic generation intensity of $BaTiO_3$ thin films on piezoelectric substrates by up to

15%[74]. However, direct measurement of strain enhancement on the electro-optic coefficient has not been demonstrated experimentally.

In this chapter, we grow films with in-plane, epitaxial strains between -0.7 and -1.5% for the purpose of characterizing their structural, optical, and electro-optic properties. Some of this characterization is currently underway with collaborators.

5.1 Film Growth

We grow smooth, c-axis oriented, strained, 80 nm film of $BaTiO_3$ via molecular beam epitaxy on $DyScO_3$, $TbScO_3$, and $GdScO_3$. These substrates impart an average in-plane strain of -1.08%, -0.97% and -0.67% respectively.

To ensure stoichiometric films, we calibrate the flux of Ba and Ti with a quartz crystal monitor, then use in-situ reflection high energy electron diffraction to monitor oscillations and further tune stoichiometry. The flux of the sources are confirmed through X-ray reflectivity measurements that can be fit to extract the thickness of the thin films. For all films, Ba and Ti are co-deposited throughout the film growth, each with a flux of about 7.4×10^{12} atoms/(cm^2·s). To oxygenate the films, we use an approximately 80% ozone, 20% oxygen mixture at a pressure of 3×10^{-8} Torr, controlled by a piezeoelectric leak valve and supplied by a Heeg Vacuum Engineering distilled ozone system. We prevent any reduction post-growth by cooling the films to 250°C or colder in the same environment. The films grow at a temperature of 730-750°C, as read by the Fluke Endourance infrared pyrometer with 1 μm spectral response. We grow on the (110) plane of various scandate substrates, which have an orthorhombic perovskite structure where the (110) plane is equivalent to the (100) pseudocubic plane. As the (110) scandate planes have slightly different in-plane lattice constants in the two orthogonal directions, we average the two lattice constants for the in-plane strain calculation.

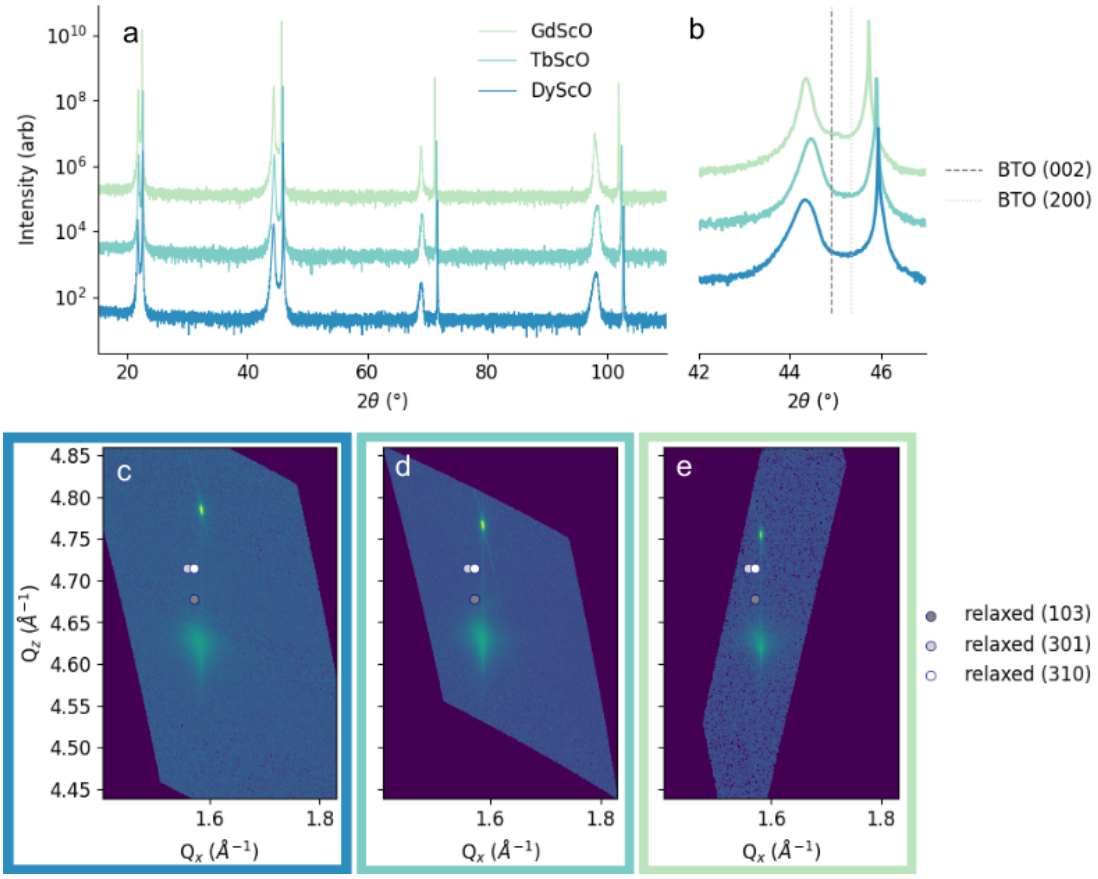

Figure 5.1: XRD scans of strained films on $DyScO_3$, $TbScO_3$, and $GdScO_3$. Larger (a) scan shows the 00*n* film peaks, while the smaller angle scan (b) zooms in on the 002 reflections and how their placement compares to the bulk 002 and 200 reflection locations. (c-e) show reciprocal space maps of the $BaTiO_3$ 103 reflection and the scandate 332 reflection on $DyScO_3$, $TbScO_3$, and $GdScO_3$, respectively.

5.1.1 Structural Characterization

Structural Characterization Methods

Structural characterization was done through in-situ RHEED and ex-situ XRD, RSM, AFM, and TEM. X-ray diffraction was performed with a Malvern Panalytical Empyrean diffractometer using Cu Kα radiation. Reciprocal space maps were taken using a two-dimensional pixel detector (PIXcel3D). Cross-sectional TEM specimens were prepared using an FEI Helios 660 focused ion beam (FIB) at 30 keV with a final thinning step at 2keV. HAADF- and ABF-STEM was performed using an aberration-corrected Thermo Fisher Scientific Themis Z G3 aberration-corrected STEM operated at 200kV.

Structural Characterization Results

Ex-situ X-ray diffraction, shown in Figure 5.1a and b, shows that the films are single crystal, fully c-axis oriented, and have a c-axis lattice constant larger than bulk, as expected.

Reciprocal space mapping of each of the three films is shown in Figure 5.1c-e. The films on $DyScO_3$, $TbScO_3$ and $GdScO_3$ all show in-plane strain commensurate with the substrate lattice constant, although there is some spread in the in-plane lattice constant in all three cases. The films are 80 nm, which is relatively thick for a strained film, so some spread is expected when compared to the 10 nm films presented in the earlier chapter. Interestingly, the $GdScO_3$ film has the largest out-of-plane lattice constant of the three films – an unexpected result given that $GdScO_3$ applies the lowest amount of in-plane strain to the film.

STEM imaging of the films, shown in Figure 5.2, demonstrate the high quality of the films with no secondary phases and few defects. The high-magnification image shows some area where the contrast between the Ba and Ti atoms is lessened, indicating that there may be a 1/2 unit cell shift in parts of the film. Nevertheless, there are not any clear domains nor does the film resemble the

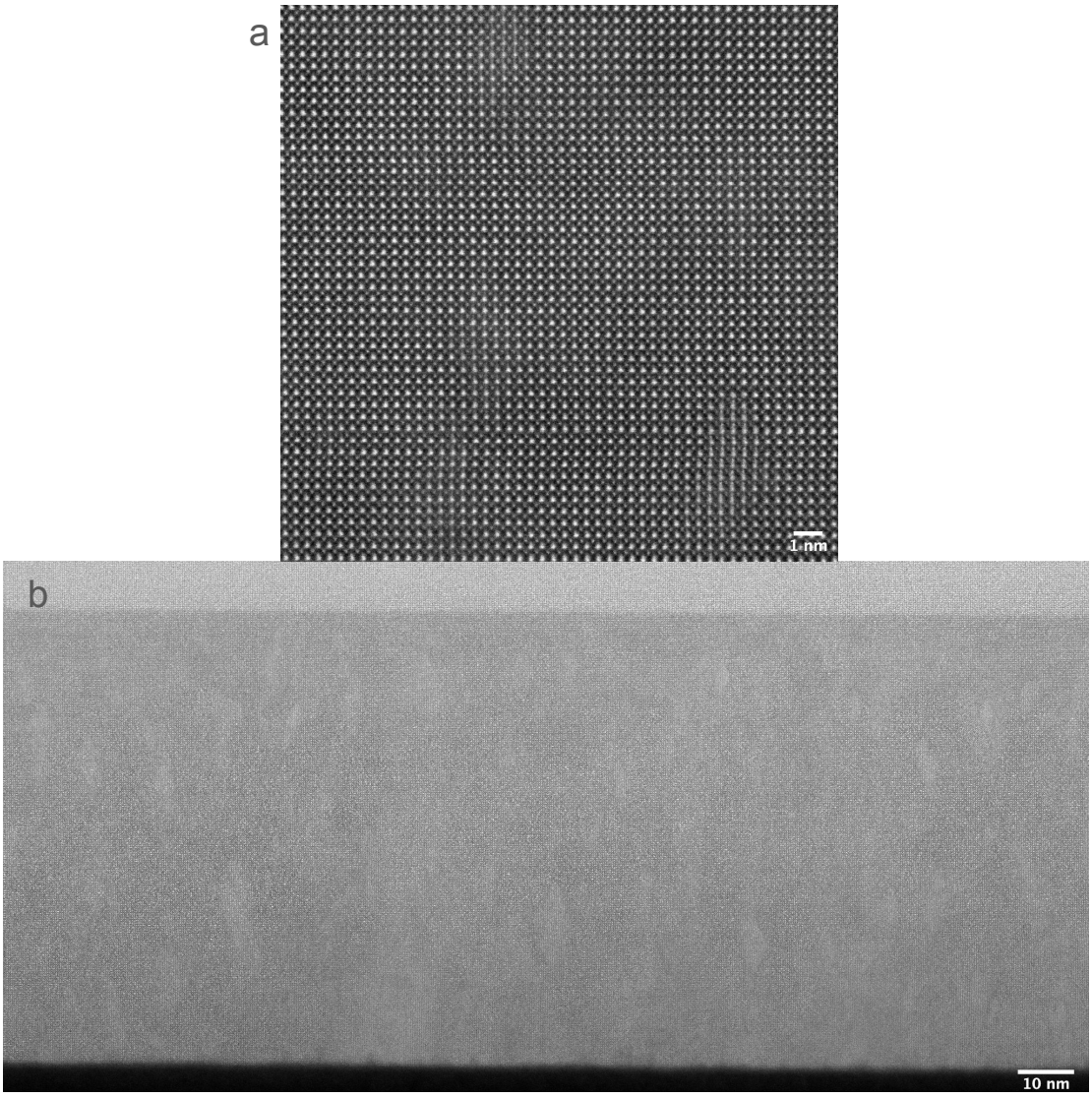

Figure 5.2: STEM imaging of the 80 nm $BaTiO_3$ film on $GdScO_3$, (a) high-magnification, and (b) low-magnification. The film shows some defects but is overall highly crystalline compared to the off-stoichiometric films from Figure 4.7.

off-stoichiometric films from chapter 4.

In addition to being strained and single crystal, the films are very smooth, with RMS roughness of 144 pm or less. RHEED and AFM are shown in Figure 5.3. High surface quality is another indication of the stoichiometric nature of the films. In all cases, the RHEED is taken the end of the film deposition but before cooling. The RHEED images do not show signs of any secondary phase or clear reconstructions. On all substrates, the surface of the film conforms to the substrate's terraces. This level of smoothness is functionally important as roughness increases loss in optical devices.

5.2 Optical Properties

Ideally, we would have an idea of the effect of strain on the index of refraction of $BaTiO_3$, as measured by ellipsometry. Unfortunately after conducting measurements on the strained $BaTiO_3$ films on scandate substrates, it is apparent that the substrates themselves have optical proprieties that make it very challenging to disentangle the properties of film itself from the overall film and substrate sample. Nevertheless, I elaborate on the experiments conducted and the challenges encountered. Note that this limitation is a function of the scandate substrates. Thin films grown via MBE on substrates with more straightforward optical properties should not encounter these issues. Unfortunately the scandate substrates are the template providing the epitaxial strain, so studying the effects of strain on optical properties is inherently coupled with substrates that can provide this type of expitaxial strain.

5.2.1 Ellipsometry

One challenge of measuring properties of thin films is that unless the measurement technique is surface sensitive, the properties of the underlying substrate must also be accounted for. In this case, the substrates pose a challenge in that the scandates are not a well studied material family. Additionally,

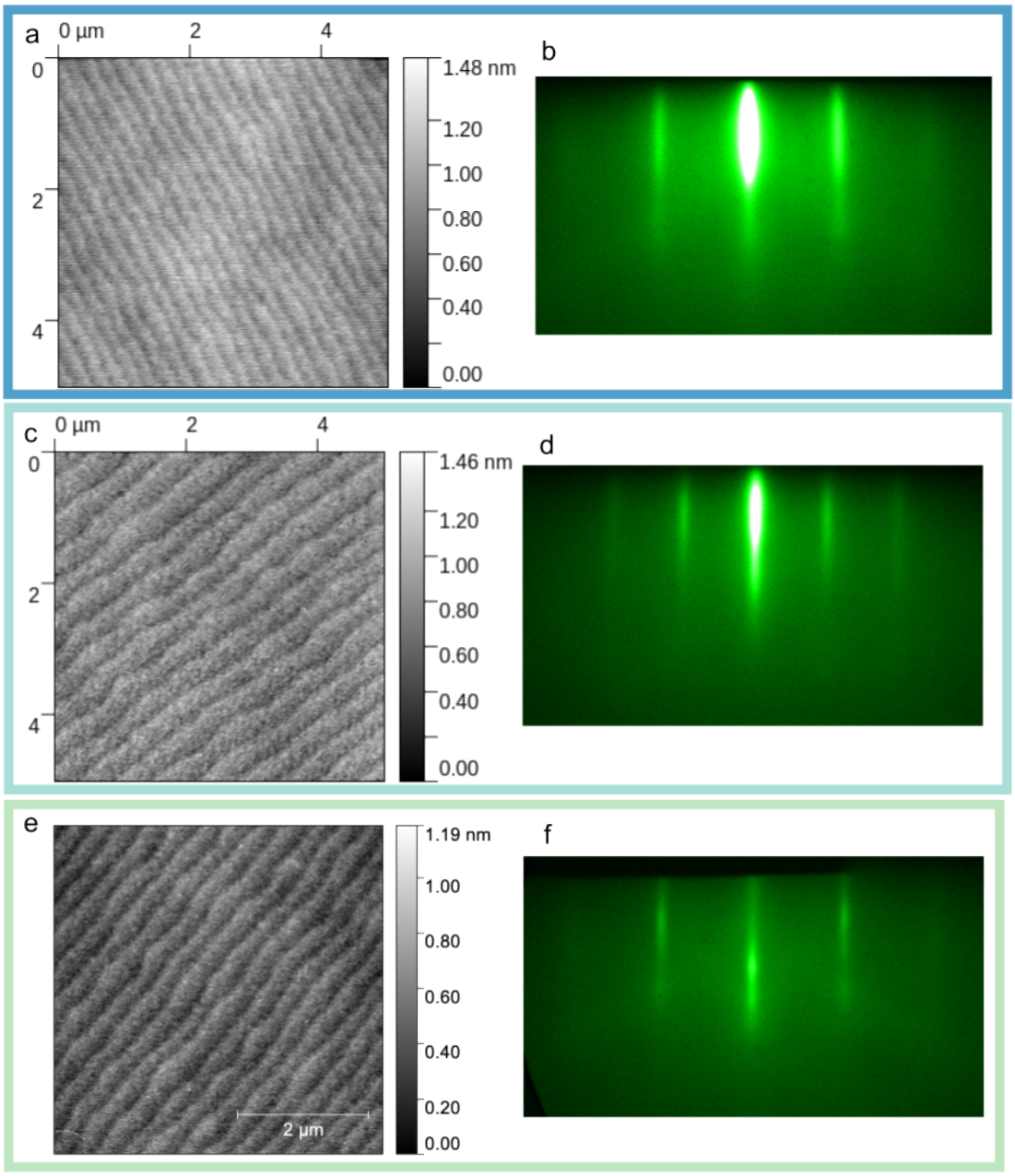

Figure 5.3: AFM and RHEED characterization of the 80 nm $BaTiO_3$ films on (a) $DyScO_3$, (b) $TbScO_3$, and (c) $GdScO_3$. Films are smooth and in-plane diffraction shows no secondary phases.

they are anisotropic crystals, which adds additional complication to fitting.

Generally ellipsometry is used to determine the index of refraction of a thin film. By taking measurements at multiple wavelength of light and and multiple angles, the Muller matrix can be fit to extract the index of refraction as well as as the loss of thin films. An example on LSAT is shown in Fazlioglu-Yalcin et. al[68]. Accurate values for the ordinary (n_o) and extra-ordinary (n_e) are important to know when designing and modeling integrated photonic devices. Prior work has demonstrated that the refractive index of strained $BaTiO_3$ thin films may deviate significantly from that of bulk,[68,61,75] but no reports have been made on the refractive index of films on scandate substrates.

However, for this measurement to be effective, the substrate must be effectively transparent for the ellipsometry data to fit correctly. If the substrate is absorbing light in the same regions that we are trying to fit the film, it is not possible to effectively extract the index. Therefore, we take both reflection and transmission measurements on the substrates themselves to see if ellipsometry can be effectively used. Results of transmission measurements are shown in Figure 5.4. In order to ensure that our substrate measurements are as close to the baseline of the film on substrates measurements as possible, we treat the substrates to the same conditions that we used for the film growth — we first anneal them and then treat with the same temperature and oxygen conditions as films grown in the MBE experience.

In all cases, the substrates have siginicant features in their transmission data in the region below 400 nm, which is where the film features are in ellipsometry. This makes it extremely challenging to analyze any film-on-scandate ellipsometry data as the substrate features cannot be isolated from the film features with a standard model.

5.2.2 UV-vis spectroscopy

UV-vis spectroscopy is a method by which the bandgap of a material can be determined. The principle behind the measurement in relatively simple — one determines how much light at each

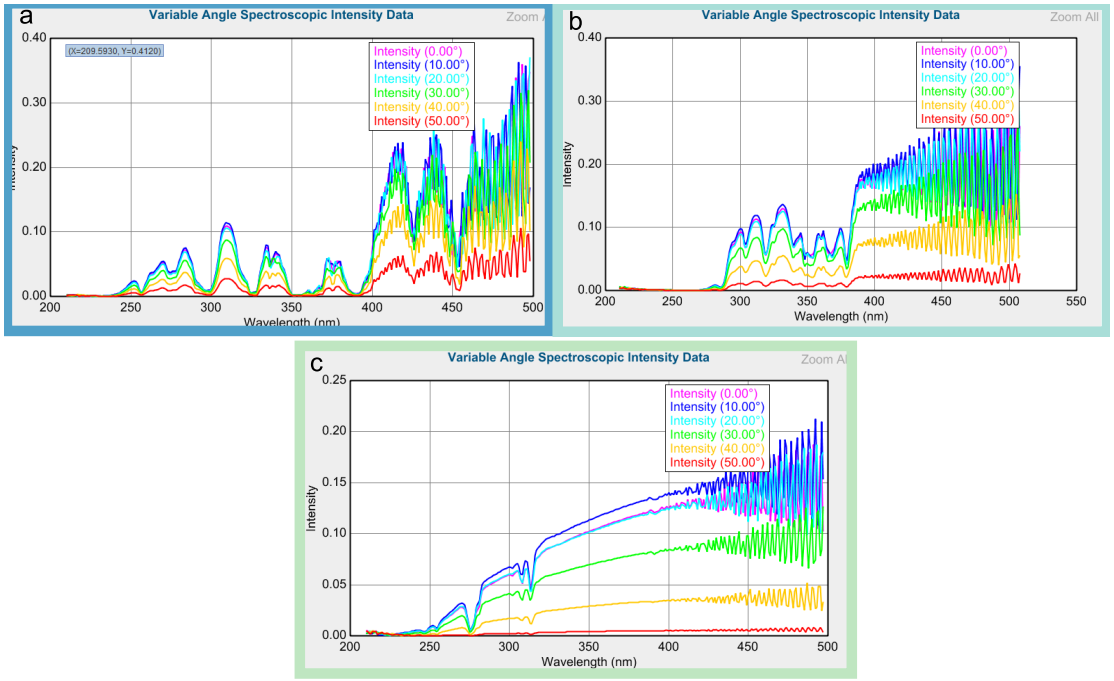

Figure 5.4: Transmission of double-sided polished substrates of $DyScO_3$ (a), $TbScO_3$ (b), and $GdScO_3$ (c) measured at different angles. This measurement shows only the intensity through the substrate. In all cases, the substrates have significant features in the >400 nm wavelength.

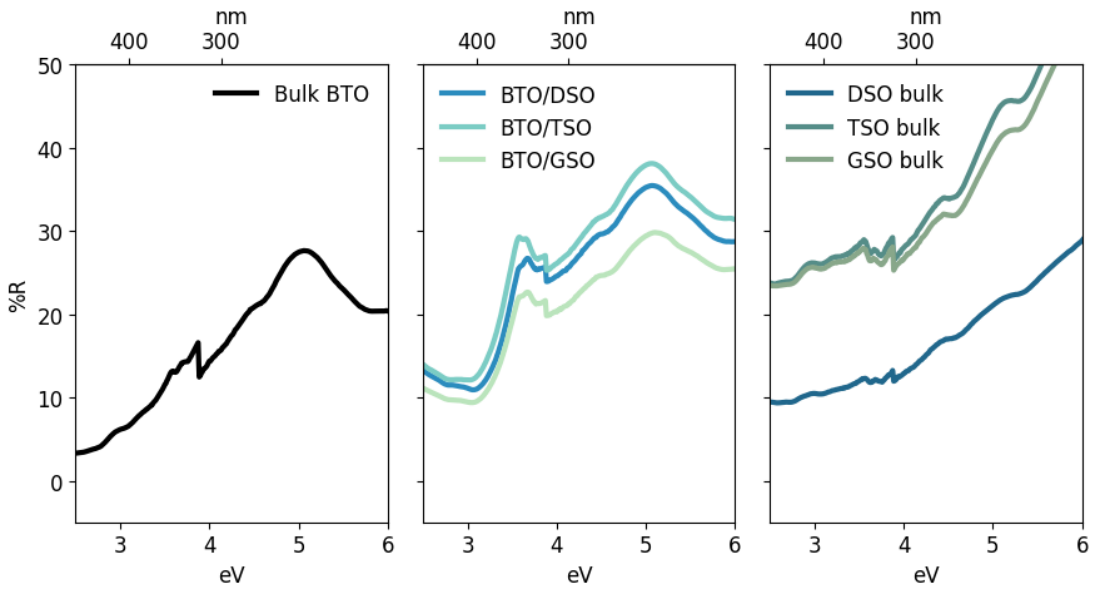

Figure 5.5: UV-vis measurements of bulk $BaTiO_3$(left), 80 nm $BaTiO_3$ films (center), and bare substrates, prepared in the same way as a $BaTiO_3$ film (right). Note that the feature at around 4 eV is an instrument artifact from changing detectors.

wavelength is absorbed. By plotting the absorption vs the energy of the light, the bandgap of a material can be extracted, as these quantities are related through:

$$(\alpha h\nu)^{1/\gamma} = B(h\nu - E_g)$$

Where α is the absorption, h is Plank's constant, ν is the wavelength of light, E_g is the bandgap energy of the material, and γ is 2 for direct bandgaps and 1/2 for indirect bandgaps.

Measurements can be taken in transmission or reflection and can either be 'diffuse' measurements, which use an integrating sphere in order to capture light that is scattered off the front or back surface, or can be taken in a specular mode where no integrating sphere is used. UV-vis is a common technique for thin films. Often these measurements are taken in diffuse reflection mode where the percent of reflected light (%R) is collected, then the Kubelka–Munk formalism is used in place of α as shown below[76]:

$$F(R) = \frac{(1-\%R)^2}{2*\%R}$$

$$(F(R)h\nu)^{1/\gamma} = B(h\nu - E_g)$$

While the Kubelka-Munk formalism is a commonly accepted method, there have been several studies into bandgap estimation using different methods and it appears that it is most important to consistently use one method between samples as different methods may yield results of bandgap energy that vary by up to 1 eV in some cases[77,78,79].

In this case we use specular reflection mode at an angle of 60°. As specular reflection does not capture any scattered light, the Kubelka-Munk formalism is not applicable. Thus we consider only the $\%R$ collected in the measurement and look at qualitative trends in the data, shown in Figure 5.5.

We collect data on a bulk $BaTiO_3$ sample from MSE supplies, on the films, and on substrates that have been prepared in the same way as the films (same heating and oxygen treatment). The bulk $BaTiO_3$ sample shows a gradual increase in reflectivity that peaks around 5 eV. The bulk bandgap of $BaTiO_3$ should be approximately 3.2 eV. In our data there are no clear features at this value. If the slope from 4-5 eV is extrapolated to the baseline at 2.5 eV, it intersects at a value of around 3.1 eV.

Bare substrates should have all have bandgaps of between 5.5-6 eV (from manufacturer), or up to 6.5 eV (in literature)[80,81]. In the UV-vis data we collect, we see that the samples become more and more reflective as the approach the bandgap energies, similar behavior to the bulk $BaTiO_3$ sample, but different behavior from what we would expect with a diffuse refelectivity measurement.

Considering the data collected on the 80 nm films, we see that the films show a similar feature as the bulk $BaTiO_3$ sample, with a peak in reflectivity at around 5 eV which does not appear in the substrates alone. However, an additional feature appears at around 3.2-3.4 eV. When extrapolated to the baseline, the intercept is at around 3.2 eV for all films. While it is unclear if this corresponds exactly to the bandgap energy of the films, it is clear both that the UV-vis of the films correlate well to the bulk $BaTiO_3$ spectra with a strong feature that is unique to the films and appears around the

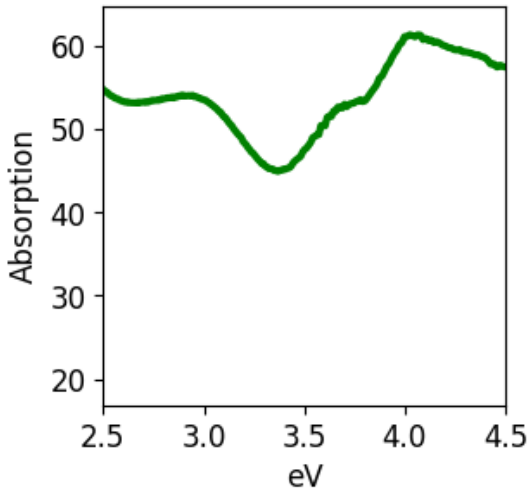

Figure 5.6: Absorption vs energy of a 200 nm thick, oxygen deficient, $BaTiO_3$ film grown on MgO, taken via UV-vis.

expected bandgap energy.

As a point of comparison, a 200 nm, fully relaxed film grown on MgO is measured with UV-vis in diffuse reflection and diffuse transmission mode, where an integrating sphere collects both the specular and scattered light in both measurements. Therefore any light not captured by one or the other of these measurements is assumed to be absorbed. Results are shown in Figure 5.6. Note that the more traditional value of absorption, or α, is shown for this film, as opposed to the specular reflection shown for strained films. In this film a bandgap-like feature appears at 3.3 eV. Increasing absorption below the bandgap may be due to oxygen deficiency in this film, which was not grown with ozone.

With this in mind, further analysis with a more traditional UV-vis setup for the strained thin films would be ideal to fully understand and analyze the trend of bandgap with strain.

5.3 Electro-Optic Measurements

5.3.1 Confocal Electro-optic Setup

To measure the electro-optical coefficient of the $BaTiO_3$ films, we use a homebuilt scanning confocal system, a schematic of which is shown in Figure 5.7a.

The measured intensity reflected from the film is proportional to the the electro-optic response. We refer to the measured signal as the normalized reflectivity $(1/r)(dr/dE)$ - the derivative of the Fresnel relation $r = (1-n)^2/(1+n)^2$ with respect to the electric field E normalized by the total reflectance. In our measurements, we sweep the DC field, light polarization, and electric field orientation and fit the resulting data to determine the electro-optic tensor components from the measured signal[82].

Since the refractive index change is very small in this configuration, we use a signal generator at 200 kHz and an RF spectrum analyzer to measure the power spectral density as a function of DC voltage, AC voltage, and optical polarization. A schematic of the electro-optic measurement system shown in Figure 5.7a. A 800 nm laser (MIRA) is first sent through a rotatable polarizer to set the input polarization. A 50/50 beamsplitter (Thorlabs) is then used to send half of the power into a reference detection arm (and into optical fiber), while the signal beam is sent into a scanning confocal system composed of a piezo-controlled xy scanning mirror, two lenses forming a 4f system, and a long focal distance 50x (NA 0.4, Olympus) near-infrared objective. The light is focused and directed into the gap of an interdigitated electrode on the surface of the film. The reflected light returns through the 4f system and is collected on the signal arm of the system and coupled into an optical fiber. Both the signal and reference arms are connected to a balanced photodiode. The intensity of the reference arm is adjusted to avoid saturating the detector using a variable ND filter, and the difference signal is sent to a Radio-frequency Spectrum Analyzer (RSA) to measure the power at the modulation frequency. The total input intensity to the photodiode is measured to properly

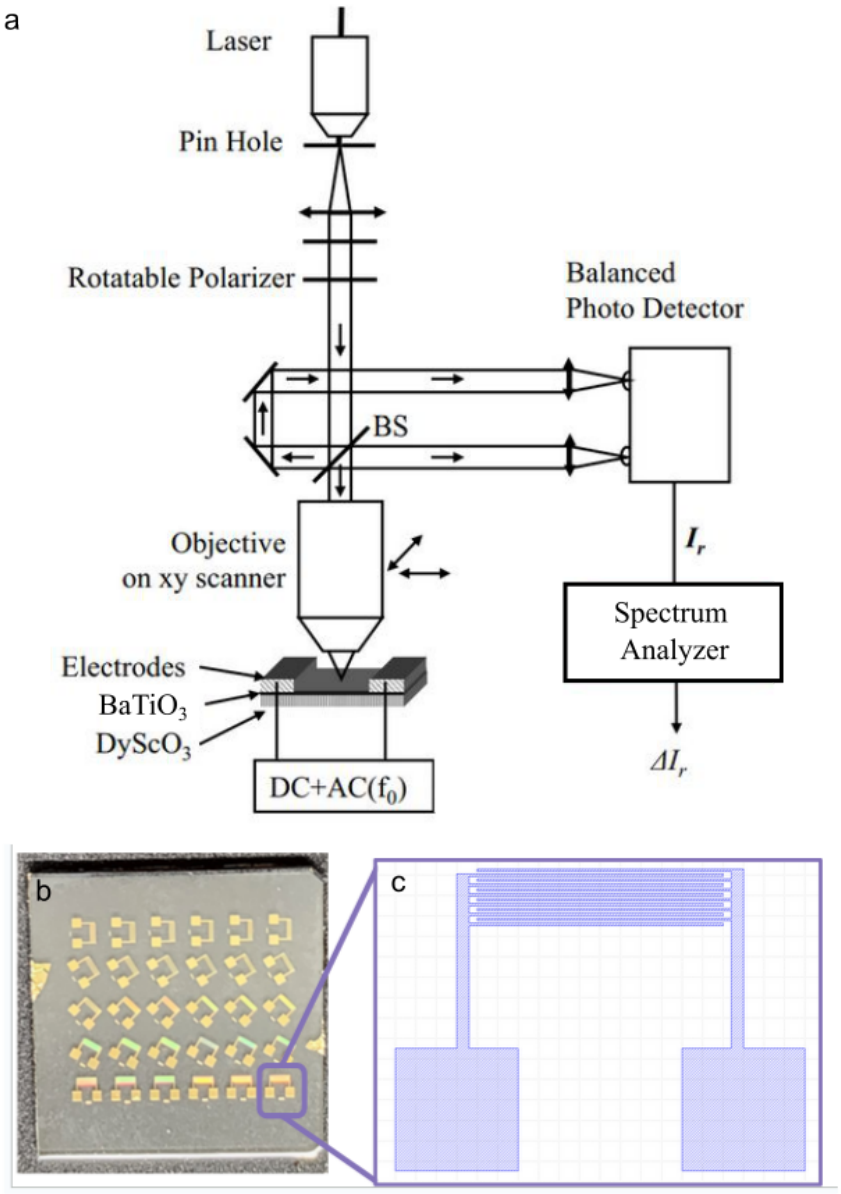

Figure 5.7: a) Schematic of the confocal scanning electro-optic measurement setup, adapted from Ma et al.[82]. A DC+AC field is applied to electrodes on the film and the resulting change in reflectivity at the AC field frequency is measured, which is proportional to the electro-optic response. b) Picture of a sample with IDEs patterned onto the film surface. Probes, which supply the electrical signal, touch down on the interdigitated electrode devices patterned onto the $BaTiO_3$ film at multiple angles. (c) schematic of the IDE design.

normalize the reflectivity.

The sample is mounted on a computer-controlled xyz piezo stage (Suruga), while the electrodes are contacted with Signatone probes connected to an AC signal generator (HP) and DC power supply (Keithley) to provide a voltage range of +/- 60 V DC. The AC signal is set to 200 kHz. We use both a DC and AC electric field to tune the electro-optic response.

5.3.2 IDE Devices

To map out the electro-optic coefficient tensor, interdigitated electrodes (IDEs) are used at various angles with respect to the crystal axis, as shown in Figure 5.7b. The devices are deposited using e-beam evaporation with a 5 nm Ti wetting layer and 200 nm of Au. Each IDE has 6 fingers, spaced 8 um apart. Fingers are 8 um in width and 500 um in length. IDEs are deposited at various angles ranging from 0°, where the electric field is in the $BaTiO_3$ [100] direction, to 90°, where the electric field is in the $BaTiO_3$ [010] direction. Measuring at a varieties of angles allows us to disentangle effects of different electro-optic tensor components rather than only measuring an effective electro-optic coefficient.

5.3.3 Electro-Optic Tensor for $BaTiO_3$

In order to understand the different effects of the electric field, crystal, and optical field directions, we consider the electro-optic tensor of $BaTiO_3$. First we define index ellipsoid, where the surface of the ellipsoid follows the refractive index of the crystal in the crystallographic direction normal to the tangent plane at that point on the surface. We use the standard basis for the definition:

$$\frac{x^2}{n_a^2} + \frac{y^2}{n_b^2} + \frac{z^2}{n_c^2} = 1$$

For electro-optic materials, the index of refraction changes upon application of an electric field, the

$$\frac{x^2}{n_a^2} + \frac{y^2}{n_b^2} + \frac{z^2}{n_c^2} + \frac{2yz}{n_{bc}^2} + \frac{2zx}{n_{ca}^2} + \frac{2xy}{n_{ab}^2} = 1$$

For electro-optic materials, the index of refraction changes upon application of an electric field in a way defined by the electro-optic tensor of that material. The symmetries of the crystal define which entries of the tensor have non-zero components. Once the symmetry of $BaTiO_3$ is applied, the below equations describe the change in refractive index in an applied electric field with orthogonal components along the crystalline axes of the film $E = E_a + E_b + E_c$:

$$\Delta(\tfrac{1}{n^2}) = \begin{bmatrix} \Delta(\frac{1}{n^2})_a \\ \Delta(\frac{1}{n^2})_b \\ \Delta(\frac{1}{n^2})_c \\ \Delta(\frac{1}{n^2})_{bc} \\ \Delta(\frac{1}{n^2})_{ca} \\ \Delta(\frac{1}{n^2})_{ab} \end{bmatrix} = \Sigma r_{ijk} E_k = \begin{bmatrix} 0 & 0 & r_{13} \\ 0 & 0 & r_{13} \\ 0 & 0 & r_{33} \\ 0 & r_{42} & 0 \\ r_{42} & 0 & 0 \\ 0 & 0 & 0 \end{bmatrix} * \begin{bmatrix} E_a \\ E_b \\ E_c \end{bmatrix} = \begin{bmatrix} r_{13}E_c \\ r_{13}E_c \\ r_{33}E_c \\ r_{42}E_b \\ r_{42}E_a \\ 0 \end{bmatrix}$$

It is important to note that the effect the applied electric field on the measured index of refraction depends heavily on the orientation of the electric field with respect to the crystalline axes. Thus it is critical to have an in depth understanding of the orientation or orientations of the crystal.

In our case, since the sample is single crystal, c-axis oriented, and our E-field is in-plane, we will only retain E_a and E_b components, which in $BaTiO_3$ distort the index ellipse in the *bc* and *ca* directions respectively. Based on our setup, our optical field polarization sweeps are in the *ab* plane, so we should see the projections of the *bc* and *ca* distortions onto that plane. The exact distortion will depend on the angle of the electrode with respect to the crystal. For further discussion, see [83].

5.3.4 Preliminary Electro-Optic Results

Preliminary electro-optic results are shown in Figure 5.8. The electro-optic conversion efficiency, which should be proportional to the effective electro-optic response, shows two lobes. The signal

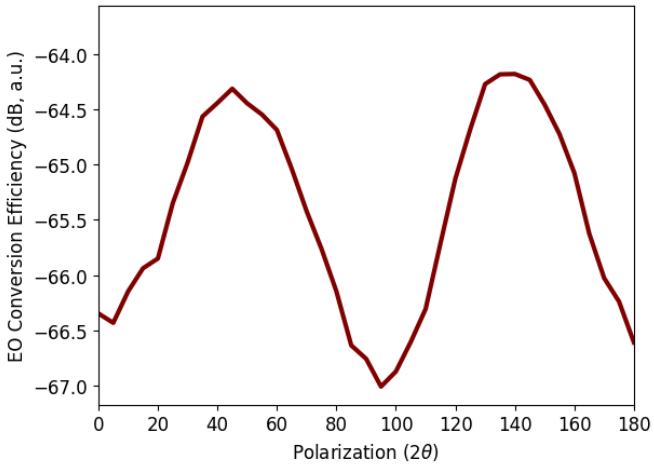

Figure 5.8: Preliminary electro-optic measurements. The electro-optic conversion efficiency, which should be proportional to the effective electro-optic response, shows two lobes with a sweep through polarization angles. The dependence on polarization is indicative of on electro-optic response in the film.

changes by nearly 3 dB between its maximum and minimum, indicating a strong electro-optic response. The electro-optic conversion efficiency is not yet calibrated to the crystallographic axis or to real units, but the dependence on polarization is indicative of on electro-optic response in the film. Calibration and analysis is ongoing. To calibrate the response, measurements on a sample of bulk lithium niobate or similar well-understood electro-optic material must be conducted. To go from an 'effective electro-optic response' to the r_{42} value of interest, data at different angles with respect to the crystal axis must be collectively fit with respect to the electro-optic tensor.

5.4 Discussion

In summary, we grow a series of 80 nm film with different amounts of in-plane strain. The films are 80nm, strained to their scandate substrates, have a low surface roughness, and are highly crystalline. We find that the nature of the scandate substrates makes it challenging to find the index of refraction of the films, but see features in the UV-vis spectra that correspond to the expected bandgap

values. We construct a confocal measuring setup that can be used to access the electro-optic tensor of interest r_{42}, and show preliminary results of electro-optic measurements on the films that indicate a strong electro-optic response.

6

Barium Titanate Grown with Hybrid-MBE

While conventional oxide MBE is a powerful tool for growing high quality $BaTiO_3$ films, there are several challenges with regards to realistic industrial-scale production. One limitation of conventional oxide MBE growth of titanate materials is that the sticking coefficient of each of the non-oxygen elements is close to one. This means that every atom of Ba or Ti that reaches the film surface will be incorporated into the film. Not all oxide films are grown in a regime where the

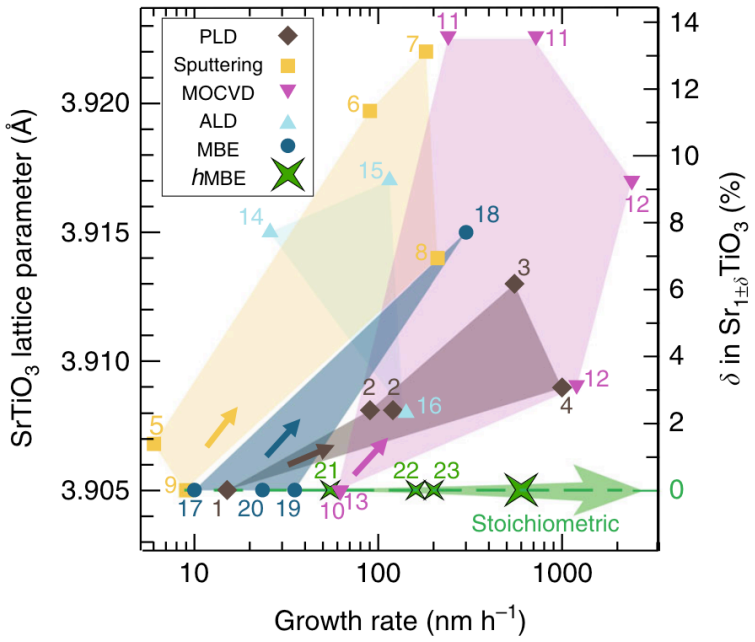

Figure 6.1: Schematic adapted from Lapano et al. showing the film quality and growth speed of $SrTiO_3$ thin film with various growth methods. In the $SrTiO_3$ material system, unlike in our $BaTiO_3$ thin films, off-stoichiometry is directly correlated with an increase in lattice constant[62]. hMBE is here identified as the most effective way to grow stoichiometric titanate films at a high growth rate.

non-oxygen elements all have sticking factors close to one, and high sticking factors are certainly not the standard in other material families grown by MBE. Growing materials in regimes with high sticking factors generally necessitates excellent stoichiometry control to achieve high quality films. Details of stoichiometry effects on MBE-grown $BaTiO_3$ can be found in Chapter 4, but suffice to say that stoichiometry control with flux calibration to within a few percent is important to achieve high quality, smooth, as-grown $BaTiO_3$ films.

Even with the best calibration, flux drift occurs over the course of days to a week. Thus, a calibration may only be stable for a day or so before there is some drift that must be re-calibrated to get back to a highly stoichiometric film. Here enters the second challenge with conventional oxide MBE for device-scale $BaTiO_3$ growth. In order to make useful photonic devices such as waveguides,

a $BaTiO_3$ film must be at least 200 nm thick as thinner films are unable to confine visible light. With conventional MBE, a limitation on the speed of $BaTiO_3$ film growth is the temperature of the Ti effusion cell. As Ti is a refractory metal, it has an extremely low vapor pressure, and is in fact the only refractory metal that can be grown with a traditional effusion cell at all. Unfortunately if Ti gets too hot and melts, it will also melt the effusion cell and cause a major failure in the MBE. To stay safe, Ti temperatures are limited to 1350°C in our MBE. This produces a flux of only 8×10^{12} atoms/(cm^2·s) or so. At these low fluxes, even with co-deposition of Ba and Ti, the growth rate is about 20 nm/hr. The resulting film growth times of 10 hours or more is getting uncomfortably close to the timescale on which flux drift begins to have an impact on $BaTiO_3$ film quality. To summarize: a slow growth rate combined with a sticking ratio of one for the films leads conventional MBE to reliably and reproduce produce thick, high quality films of $BaTiO_3$.

Other options for increasing Ti flux have been identified, such as using an ALD-inspired approach by introducing a metal-organic precursor as a source of Ti into the MBE. This technique, known as hybrid MBE (hMBE), can not only increase film growth rate but also move $BaTiO_3$ film growth into an adsorption-controlled regime where stoichiometry control requirements are relaxed. Because the vapor pressure of the metal organic is extremely high (as a liquid at room temperature), it is easy to supply a very high Ti pressure with modest source temperatures of less than 100°C. The hydrocarbon ligands attached to the Ti atom in the TTIP molecule strongly affect the surface kinetics of the molecule and result in a sticking factor of less than one, thus allowing stoichiometric films to grow with some range of Ba:Ti ratios. With these benefits in mind, hMBE of titanates has been an active area of research over the course of the last decade, with reports of high quality films of both $SrTiO_3$ [84,85] and $BaTiO_3$ [86,87,68] As shown in Figure 6.1, hMBE has been identified as the most effective method for achieving stoichiometric films of $SrTiO_3$ at high growth rates, up to 100s of nm/hour[88].

6.1 Prior work and 'growth window' concept

Thinking about the compositional phase space with hMBE is significantly more complicated than it is with conventional MBE. In conventional oxide MBE of titanates, the Ba and Ti flux can be individually calibrated (for example with binary oxides), then the Ba:Ti flux ratio can be set to one. Moving away from this ratio generally yields non-stoichiometric films. In hMBE, there is a 'growth window' of Ba:Ti flux ratios where stoichiometric films can form. However, calibration can be challenging because the Ti flux cannot be measured directly. Generally Ti 'flux' is reported through TTIP beam equivalent pressure (BEP) or foreline pressure, both of which are assumed to be linear with the 'actual' flux of TTIP that is available to be incorporated into the film based on the ideal gas law. Since the sticking factor of the TTIP heavily depends on the surface dynamics, the effective flux for a binary oxide such as TiO_2 is not necessarily the same as the effective flux for a film such as $BaTiO_3$ even if the BEP or foreline pressure measurements are held constant between those two growths. Additionally, factors such as the substrate temperature, chamber pressure, and growth rate have a strong effect both the size of the growth window and the specific Ba:Ti ratios the growth window cover[89].

Prior works with TTIP have taken different approaches to stoichiometry variation. In work by Jalan on hMBE-grown $SrTiO_3$, the TTIP beam equivalent pressure (BEP) is held constant and the Sr flux is varied over a 300% range at various temperatures[89]. The stoichiometric window found in that work is reproduced in Figure 6.2a. As the growth temperature increases, the stoichiometric window increases and also shifts to have a higher Ti:Sr ratio. Between temperatures of 700°C and 800°C, the growth window increases from growing stoichiometric films within 5% range of Sr flux variation to a range of 30%. This work also shows that increasing the oxygen pressure in the chamber reduced the growth window at the same temperature, which is assumed to be due to increased TTIP degradation in the presence of oxygen.

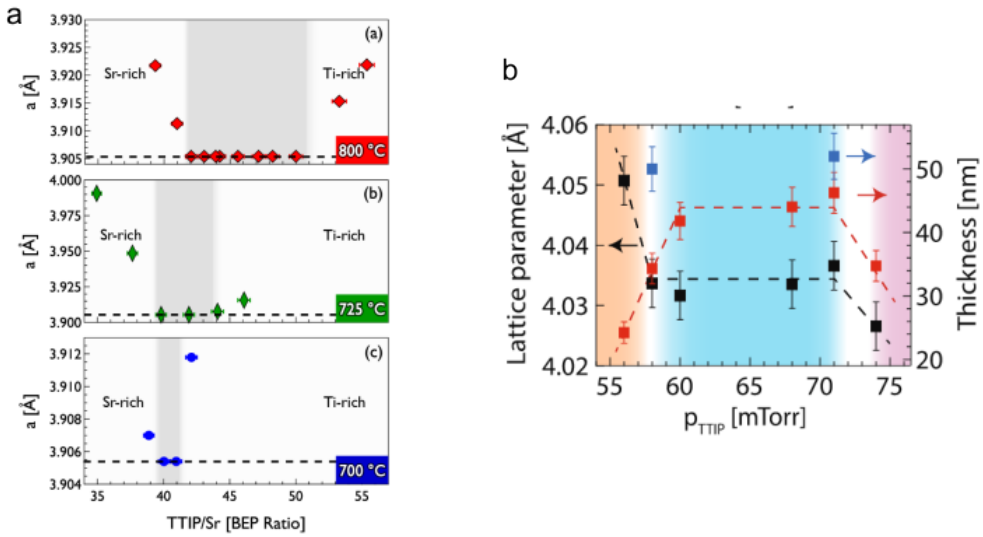

Figure 6.2: Stoichiometry windows for hMBE grown (a) $SrTiO_3$, reproduced from Jalan[89], and (b) $BaTiO_3$, reproduced from Fazlioglu-Yalcin et al[68].

In the work of Fazlioglu-Yalcin et al. on hMBE-grown $BaTiO_3$, the Ti pressure is varied while the Ba flux is held constant[68] at 800°C. Representative results are reproduced in Figure 6.2b and show a growth window where the TTIP foreline pressure can be varied by 25% while retaining stoichiometric film growth. No additional oxygen was provided to films during growth. Note that this work found that for relaxed $BaTiO_3$, the lattice constant for Ba-rich films is larger than bulk while for Ti-rich films the lattice constant is smaller than bulk. This relationship between stoichiometry and lattice constant is different from the trend discussed in Chapter 4 for fully strained $BaTiO_3$ films, so it is important to know whether films are strained or relaxed when considering the lattice constant as an indicator of stoichiometry.

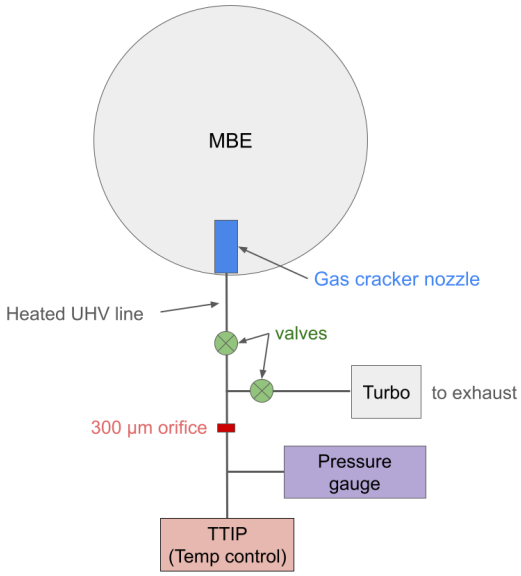

Figure 6.3: Schematic of TTIP system.

6.2 Methods and Equipment

The system we are using for hMBE growth is a commercial ALD system made by SVT Technology Services & Solutions, customized to fit on our MBE. The MBE is a Veeco GenXplor fitted with an radio-frequency (RF) plasma source for oxidation. LSAT substrates are cleaned before use in acetone and IPA. Films are grown without additional oxygen or plasma except where otherwise specified. The Ba is loaded in a conical Ti crucible with a differentially pumped effusion cell. The MBE is fitted with a 1/2 jacket for LN_2, which is supplied during growth except where otherwise specified. The TTIP itself is from Sigma Aldrich.

The TTIP delivery system has a fixed 300 μm orifice between the TTIP can and the high vacuum lines. A valve system allows the TTIP to be either pumped into a 'conditioning' line into exhaust or into the MBE chamber. TTIP flux is controlled through the temperature of the TTIP can and is monitored in the foreline, before the orifice. These local pressures are generally in the 0.2-0.4 Torr

range for TTIP temperatures of 30-50°C range. During a normal film growth the TTIP is brought to temperature and the pressure is monitored until the TTIP foreline pressure is stable in the conditioning line for around 30 minutes. Then the TTIP is directed into the MBE chamber through a heated gas cracking nozzle kept at 150°C while the conditioning line is kept under vacuum. To end the growth, this process is reversed. The lines the TTIP goes through are heated to prevent any condensation.

Note that low RHEED intensity or lack of RHEED images for films throughout this chapter is caused by platen design limiting RHEED coverage of the films.

6.3 Exploration of hMBE $BaTiO_3$

6.3.1 Effect of LN_2

Many MBE systems use liquid nitrogen (LN_2) to cool the shroud of the system to keep the pressure of the MBE low during film growth. As the LN_2 cools the walls of the MBE, the chamber walls act as type of temporary cryo-pump.

In hybrid MBE of $BaTiO_3$, we find that LN_2 is essential to achieve reasonable film crystallinity. A comparison between two subsequent films, one growth without LN_2 and the next with LN_2 while with all other growth parameters are held constant is shown in Figure 6.4. Films are grown on LSAT substrates with a thermocouple temperature of 800°C (870-900°C measured by pyrometer). The foreline pressure of the TTIP was 280 mTorr, and the Ba flux was approximately 2.3×10^{13} atoms/(cm^2·s). As shown in Figure 6.4c, the maximum chamber pressure for the film grown without LN_2 reached 2.16×10^{-6} Torr, while the maximum pressure for the film grown with LN_2 was 4.6×10^{-8} Torr. It is important to note that the difference in pressure is due to the presence of TTIP in the chamber. The base pressure of the chamber before opening the TTIP valve to the chamber is similar (within 2×10^{-8} Torr of each other), and the increase in pressure dur-

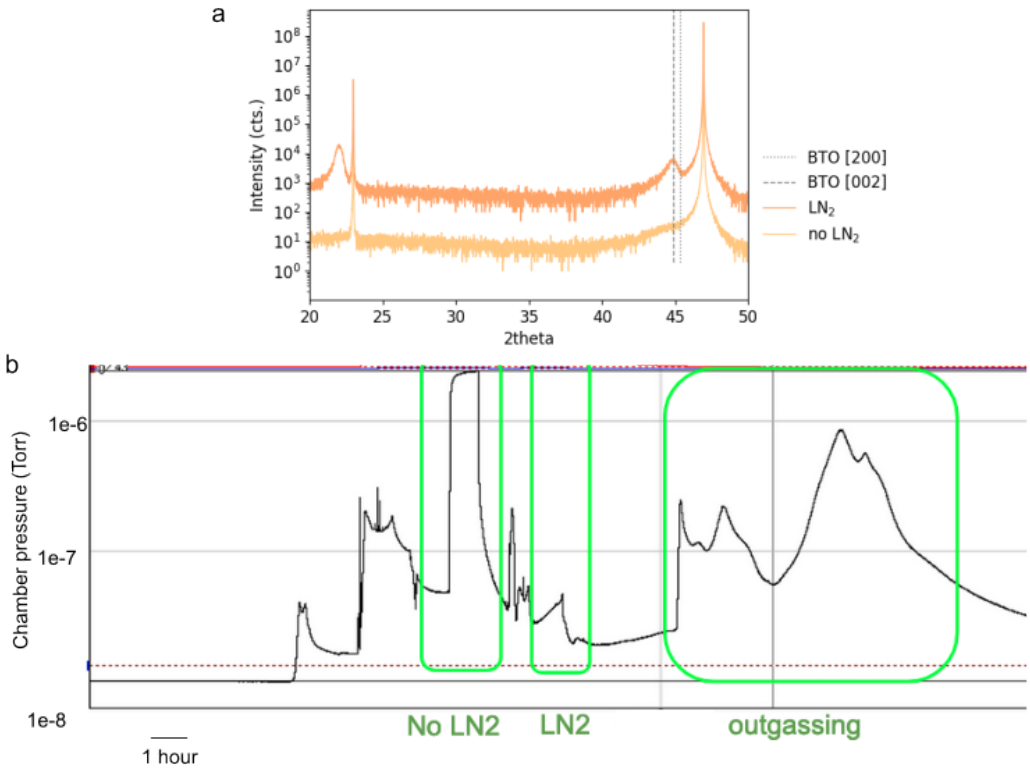

Figure 6.4: XRD of films grown with (a) and without (b) LN_2 cooling of the MBE chamber walls. Films were grown subsequently and with other growth parameters held constant. (c) Pressure trace in Torr of the growth chamber before and during film growth. Each film growth is 40 minutes long and indicated by the boxes. Pressure spikes outside of the growth portion are from the Ba effusion cell, TTIP injector, and sample platen outgassing. Effects of the chamber warming up are also indicated in a green box. The growth pressure of the film grown with LN_2 is nearly 2 orders of magnitude lower than the film grown without LN_2.

ing TTIP film growth comes almost exclusively from the TTIP being introduced to the chamber. The pressure spikes and drops quickly with the respective opening and closing of the TTIP nozzle. The molecules causing the increase in pressure are the TTIP molecules and any TTIP hydrocarbon byproducts produced upon decomposition.

On the film grown without LN_2, there is a shoulder on the $SrTiO_3$ 002 substrate peak in the correct range for a $BaTiO_3$ thin film, but there is not a strong, coherent, film peak over the 2θ range. On the other hand, when the MBE is cooled with LN_2 during film growth, there are distinct $BaTiO_3$ $00n$ film peaks. In this case, the film is not fully stoichiometric, so the 002:001 peak intensity and overall film crystallinity is not of the highest quality.

Nevertheless, the marked change in the film crystallinity between the film grown with and without LN_2 indicates that a low chamber pressure is critical to achieve good results with TTIP and further indicates that when the pressure of TTIP molecules and decomposition products are present in high quantities, they disrupt the crystallinity of the film growth. This results is interesting as prior work on hMBE-grown $SrTiO_3$ indicate that films grown with TTIP do not incorporate detectable levels of hydrocarbons as long as the substrate is kept at a temperature >800°C during growth, as measured by secondary ion mass spectroscopy[90]. While mass-spectroscopy-type characterization has not been done, it seems likely that there is some incorporation of TTIP or TTIP decomposition products into the film that disrupts the out-of-plane crystallinity.

Another interesting observation is that the $SrTiO_3$ and anatase TiO_2 films grown with the same hMBE chamber under similar conditions did not require LN_2 to form coherent, crystalline films, although extensive testing was not done on these films outside of RHEED and XRD characterization. See Chapter 7 for more details and characterization of anatase TiO_2 films.

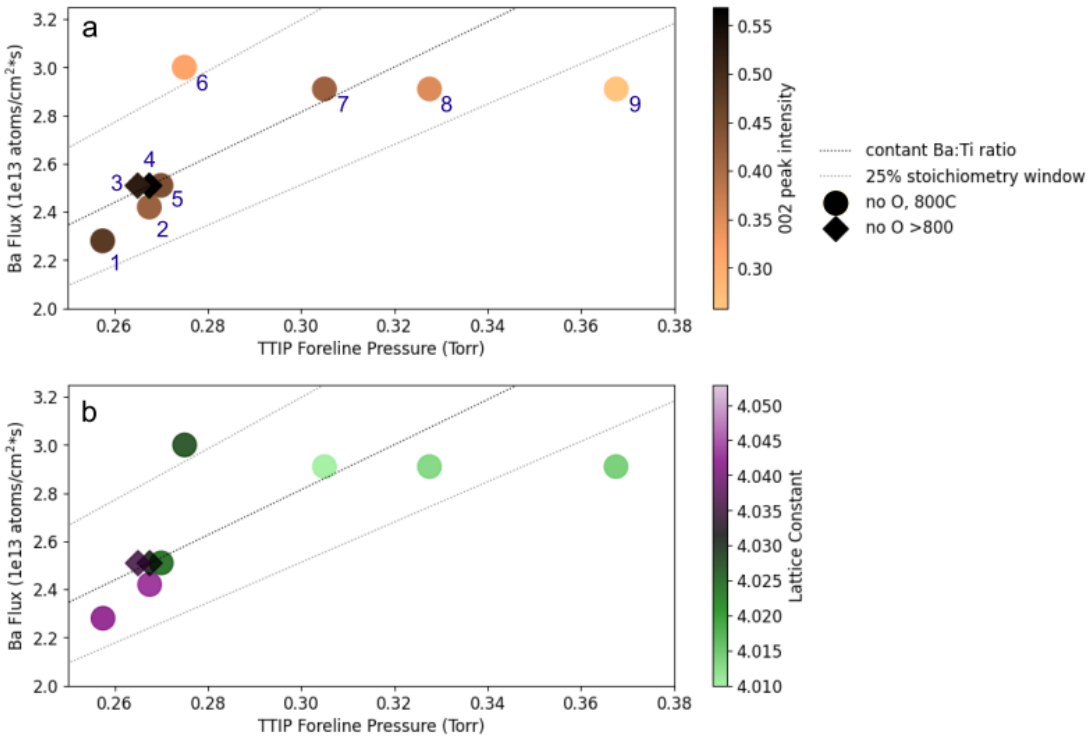

Figure 6.5: (a) Films plotted with respect to their TTIP and Ba flux's. Color indicates 002 film peak intensity. Iso-stoichiometry lines are drawn as a guide to the eye, with the area between the two outer lines corresponding to a 25% window of stoichiometry. Samples indicated with an arrow are shown in (b). (b) similar to part (a) but here color indicates lattice constant of the film, with the bulk lattice constant of $BaTiO_3$ shown in black.

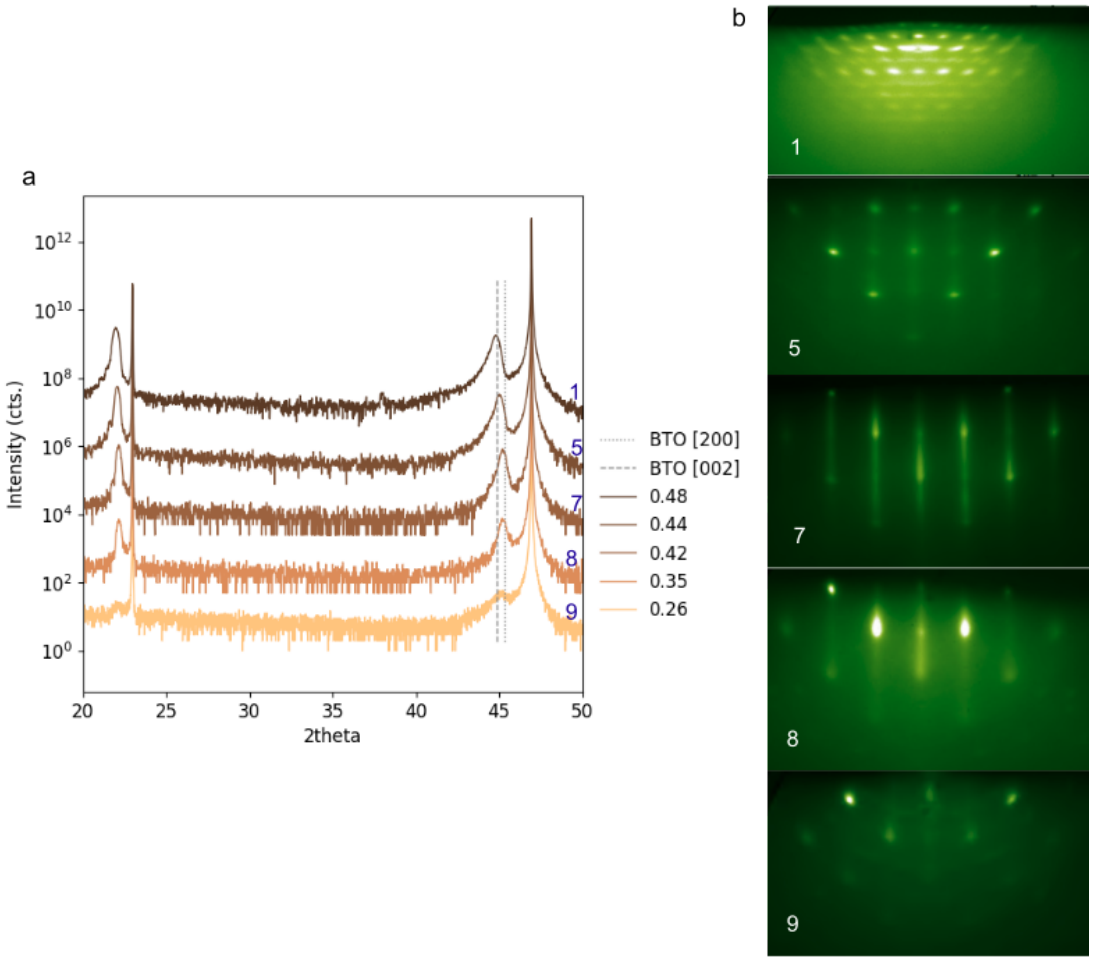

Figure 6.6: XRD (a) and RHEED (b) characterization of five representative films grown across the Ba flux: TTIP foreline pressure phase space. XRD traces are color-coded according in line their 002 peak intensity, as in Figure 6.5a. All films show indications of a rough surface or secondary phase in RHEED. Film quality assessed qualitatively via RHEED quality does not fully correlate with our XRD measure of merit.

6.3.2 Exploring stoichiometry

In our work on $BaTiO_3$ film grown with hMBE, we have begun to explore the phase space of high quality film growth by growing films at different TTIP pressures and Ba fluxes, as opposed to fixing one or the other of these values.

Most films are grown at 800°C with no additional oxygen, so based on prior work we would also expect a roughly 25% stoichiometry window. Results are shown in Figure 6.5. Films are categorized by their 002 peak intensity in XRD (Figure 6.5a) and by their lattice constant (Figure 6.5b). Each film is labeled with a number which will be used to identify that film throughout this chapter. A set of representative films, characterized by XRD and RHEED, are shown in Figure 6.6 for reference. As a guide to the eye, a line of constant stoichiometry is drawn in the phase diagrams with the expected 25% growth window. This is not a line of perfect stoichiometric growth, but is rather our current best estimate. The films are of varying crystalline quality, but all are c-axis oriented, based on XRD analysis.

As expected, films generally have higher quality along the iso-stoichometry line and generally decrease in quality as we move away. With the conditions of 800°C and no oxygen, it seems our measured growth window is smaller than that found by Fazlioglu-Yalcin et al[68]. Because different systems measure temperature at different locations and with different methods, it is very possible that we are at a lower effective temperature in our system, thus shrinking our growth window. Given this, it is especially important to note that the highest quality films, as measured by XRD, are the two grown at a higher temperature. This will be discussed more in depth in Section 6.3.3, but here we simply note that we likely have a relatively small growth window at a temperature of 800°C.

Another important note is that for our films, the XRD 002 peak intensity is not sufficient to fully characterize the quality of the film. As shown in RHEED images, some of peaks with the most intense 002 peaks do not appear to be smooth, for example the film labeled "1" appears to have mul-

tiple in-plane domain orientations or a secondary phase. Although the XRD shows only a single crystalline phase, it is possible that there is a secondary phase of low total volume or that is not epitaxial.

Even within the relatively small range we explore in this chapter, the ratio of TTIP flux:Ba flux is not sufficient to fully describe our films. This is clear when the lattice constant of the films is considered. Nearly universally, films grown at a slower rate (lower TTIP pressure and lower Ba flux) have a higher lattice constant, while films grown more quickly having a lower lattice constant. A side by side comparison of two films grown with the same nominal TTIP:Ba ratio but at speeds that vary by 50% can be seen in Figure 6.7. In this example, not only does position of the film peaks change slightly between the two growths, but the film grown more slowly looks more strained to the LSAT based on the 002 peak asymmetry, and has generally more intense film peak. These results indicate that in order to optimize the quality of the $BaTiO_3$ films with hMBE, care must be taken to specify where, in the overall area of the TTIP:Ba flux diagram, the films are grown and not only compare the TTIP:Ba flux ratio. Prior work on $SrTiO_3$ showed that relative growth window decreases as the rate increases, although the range of TTIP pressures explored was almost an order of magnitude larger than in our study[88].

6.3.3 Effect of Substrate Temperature

Next we look specifically at three films grown one after another with similar TTIP:Ba flux values. One film was grown in a platen which exposes the substrate directly to the heater at a thermocouple-read value of 800°C. The next film was grown under the same conditions but at a thermocouple-read value of 900°C. The final film was grown on a different style of sample holder where the substrate is pasted to a solid metal plate and not thus not exposed directly to the heater, at a thermocouple value of 800°C. Based on personal qualitative observations from a number of growths on various MBE systems, substrates pasted onto the solid metal plate design get significantly hotter

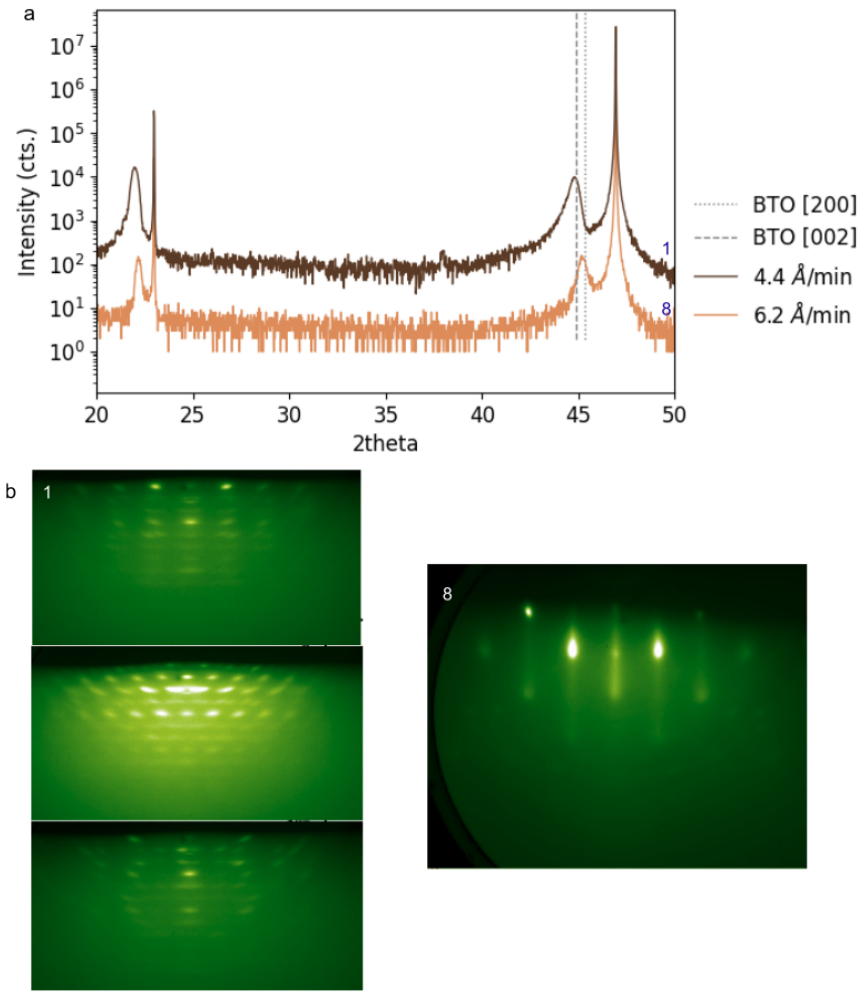

Figure 6.7: XRD (a) and RHEED (b) of two films with the same nominal TTIP:Ba ratio but grown at different overall speeds. The lattice constant of the films as well as the overall film crystallinity varies between the two films. Note that the XRD peak at 38.6° is a Ag (111) peak, and artifact of the paste used to mount the sample. RHEED patterns differ greatly for the two samples.

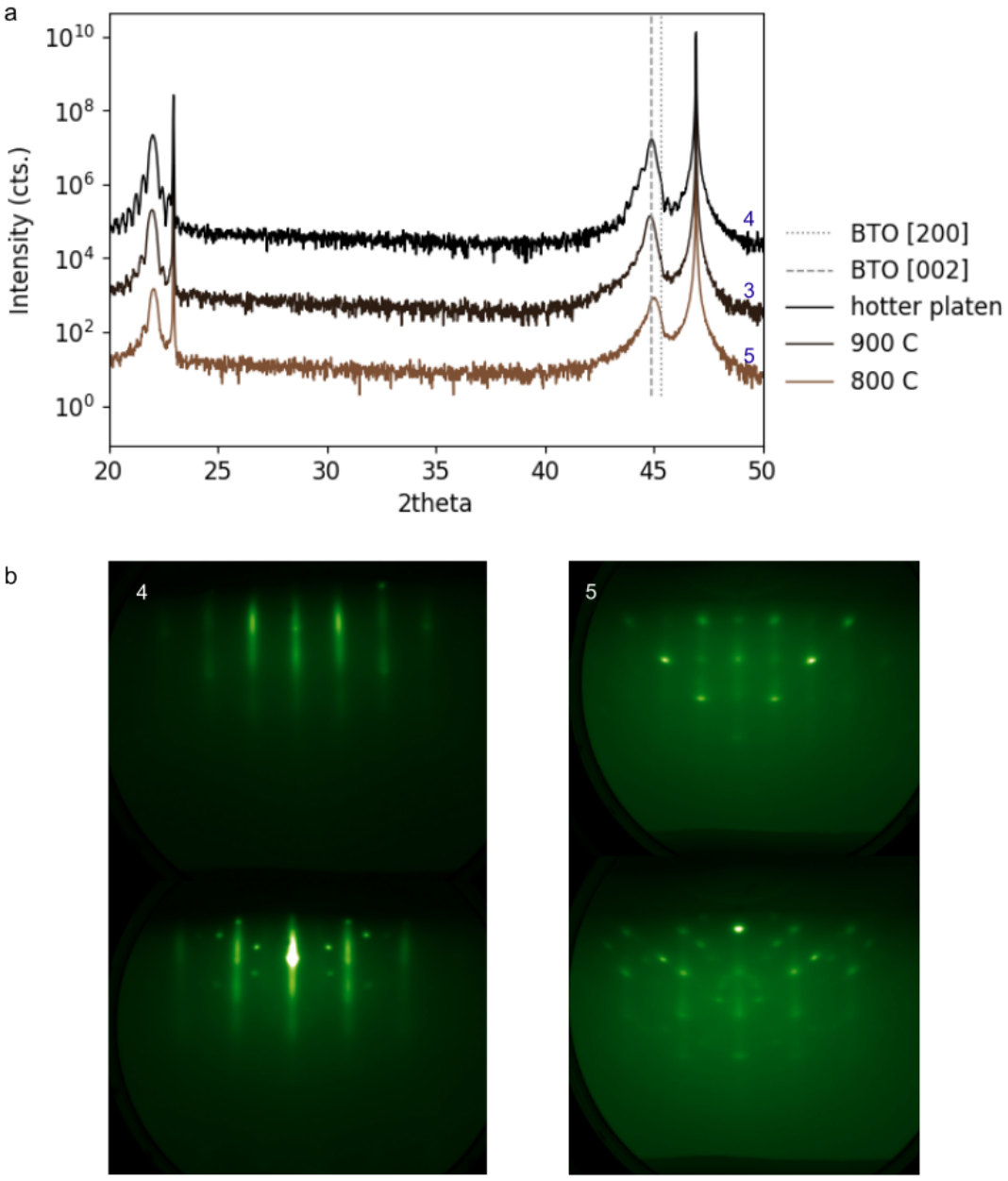

Figure 6.8: Samples grown at different temperatures but otherwise similar growth conditions. Films grown at higher temperatures are of higher quality in both RHEED and XRD. We were unable to acquire reasonably high-intensity RHEED images on sample 3, likely due to platen design and alignment.

than substrates directly exposed to the heater, even when substrates are 'backside-coated' with a thin layer of Pt to increase their heat absorption. Since the directly-exposed substrates in this test were not even backside-coated, they are unlikely to be in temperature equilibrium with the thermocouple reading, which is taken very close to the heating filaments of the substrate heater. We therefore assume the film on the solid metal plate has the highest growth temperature of the three samples.

RHEED and XRD results can be seen in Figure 6.8. As the temperature increases, the crystallinity of the sample's 001, 002, and especially 003 peaks in XRD also increase. The RHEED of the hottest sample also looks significantly smoother than that of the coldest sample. Note that the relative intensities of the RHEED is not a good indication of film quality, rather the RHEED pattern itself must be considered. Note also that all three samples show either some amount of roughness or a secondary phase that show spots in the RHEED, nevertheless the hottest sample has the highest quality film streaks.

Based on the growth window of hMBE-grown $SrTiO_3$, as the temperature increases, the growth window should both expand and also move to require more Ti flux[89]. Therefore these results make sense if we are in an area of the Ba:Ti flux phase diagram that is close to stoichiometric or slightly Ti-rich for the 800°C film. Based on these results in conjunction with the results shown in Figure 6.5, growing at significantly higher thermocouple temperatures or with sample holders that lead to higher effective temperatures is important in achieving high quality $BaTiO_3$ films.

6.3.4 Effect of Oxygen Plasma

Next we explore the effect of oxygen plasma on $BaTiO_3$ film growth. Two films are grown sequentially with growth parameters kept similar, but one film is grown with a pressure of 9e-7 Torr oxygen plasma introduced into the chamber while the other is grown in a vacuum pressure of 7e-8 Torr or below. Results are shown in Figure 6.9. XRD results show that the film grown with plasma had decreased crystallinity compared to the film grown in oxygen. Additionally, although the film was

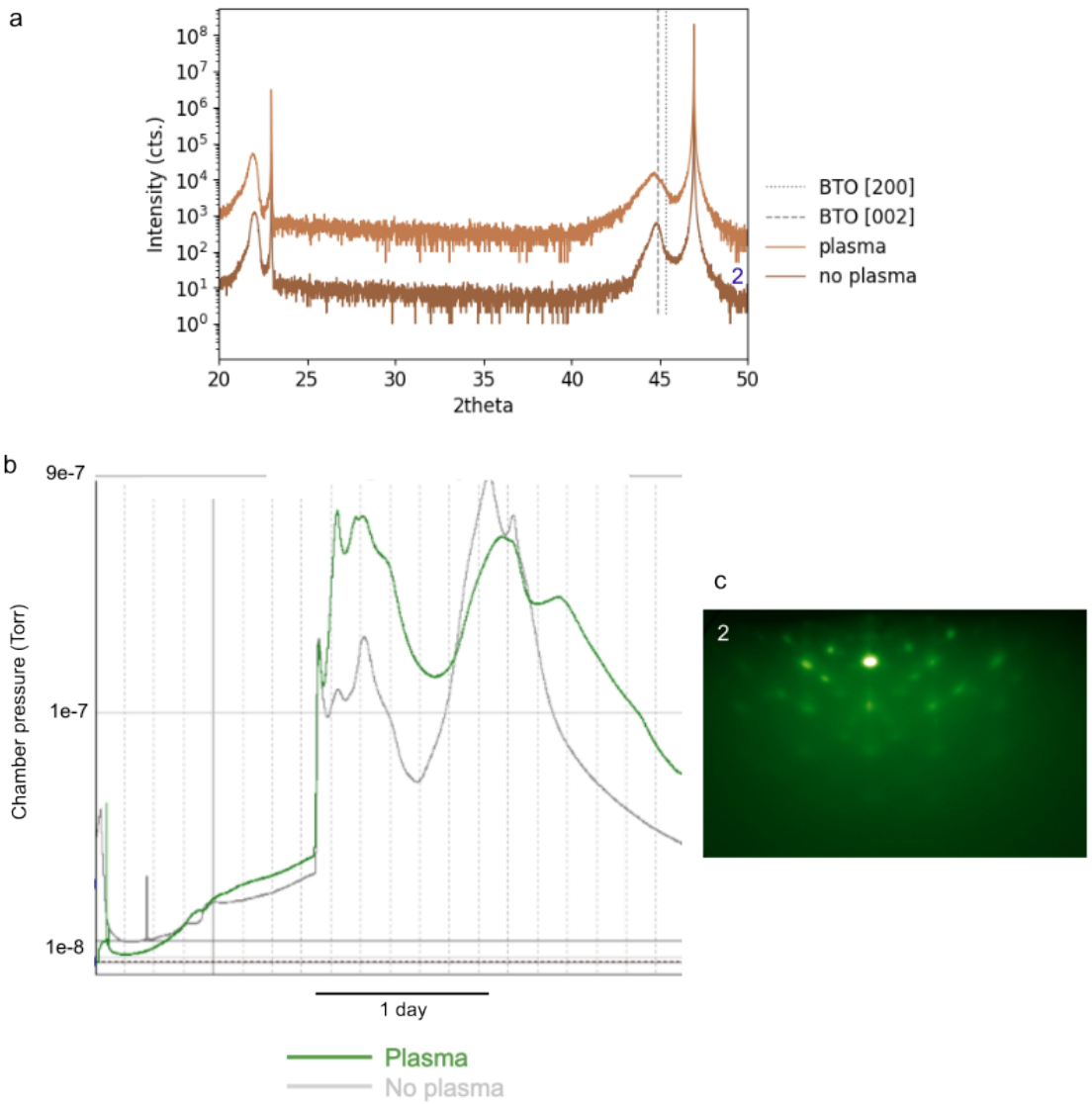

Figure 6.9: (a) XRD of two films grown sequentially and with growth parameters held the same between films except for the introduction of oxygen plasma. (b) differences in outgassing pressure trace with and without plasma. (c) RHEED image of film grown without plasma.

grown with similar fluxes, the film grown with plasma was about 6% thicker than the film grown without plasma.

Taken together, the results indicate that the plasma assists with TTIP degradation, effectively increasing the sticking factor of the Ti and thus shrinking the growth window. These results are in link with prior work that saw a decreasing growth window with increased oxygen pressure in hMBE $SrTiO_3$ growth [89], and prior work which showed that introduction of plasma significantly changes the TTIP sticking factor at temperatures below 900°C [91].

Another indication that plasma in the chamber significantly changes the degradation of TTIP is the pressure of the chamber upon outgassing. As described earlier, when LN_2 is used to cool the chamber walls, TTIP and its decomposition products stick to the walls of the MBE chamber. After film growth is finished, the LN_2 flow to the chamber is stopped and as the LN_2 evaporates, the chamber warms back up to around room temperature, which causes outgassing of the chamber walls. The pressure trace during outgassing has a repeatable shape with consistent peaks. Although we do not monitor the temperature of the chamber walls, we can consider the pressure trace to be indicative that different decomposition products degas from the chamber walls at different temperatures.

Figure 6.9b shows the difference in the outgassing pressure trace between films grown with and without plasma. Many of the same peaks appear, but the relative intensity of the peaks are very different. It appears that using plasma increases the concentration of both smaller decomposition products that degas early, and also heavier decomposition products that take almost a day to fully degas, while decreasing the concentration of mid-weight decomposition products. To more fully understand the exact nature of these different categories of decomposition products, a residual gas analyzer (RGA) attached to the chamber could be used.

6.4 Discussion

Overall, the preliminary results presented here paint a picture of a complex landscape with many variables. Films grown on LSAT with a thickness of 30-40 nm appear to grow relaxed. We explore the effects of substrate temperature, plasma, growth rate, and variations in the 2-dimensional phase space of TTIP pressure and Ba flux. Generally, we find that the majority of films in the phase space we explore have some roughness or a secondary phase in RHEED even if they appear high quality in XRD. In line with prior work, a hotter substrate temperature increases the film quality as measured by both XRD and RHEED, while growing at a faster deposition rate and introducing plasma into the system seems to narrow or shift the growth window. Further exploration of this phase space is needed to achieve high quality, smooth, single crystal $BaTiO_3$ via this hMBE system.

7

Anatase TiO_2

In addition to being a useful way of calibrating Ti flux for film growth [92], anatase TiO_2 has been identified as a promising material for surface-based photochemistry such as photocatalysis and solar cells [93,94]. Unfortunately, anatase TiO_2 (TiO_2-a) is difficult to synthesize in bulk because it is metastable at room temperature and transitions irreversibly to the more stable rutile form (TiO_2-r) at 575°C (see Figure 7.1) [67]. When synthesized in nanoparticle form, TiO_2-a can stabilized to provide large surface areas for catalytic activity, but careful process control including appropriate

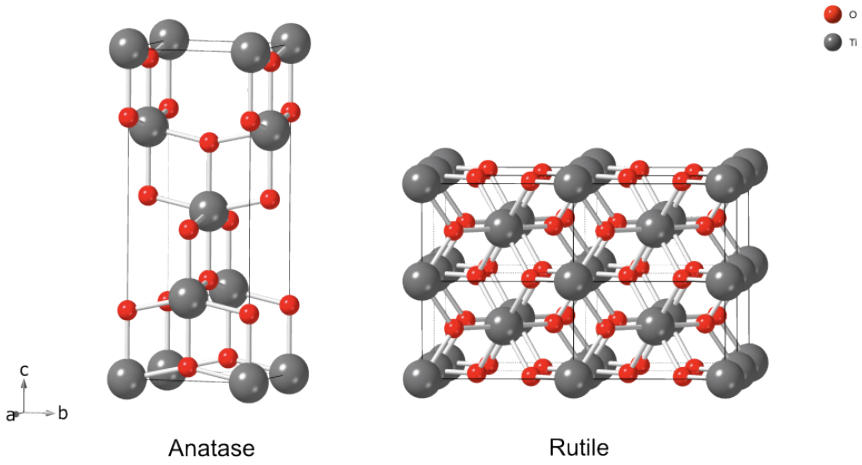

Figure 7.1: Anatase and rutile crystal structures of TiO_2.

selection of morphology controlling agents is needed to form nanoparticles with a high proportion of reactive surface area [95]. Epitaxial stabilization of TiO_2-a is another option for fabricating large surface areas, and choice of substrate can determine which plane of the anatase crystal structure is exposed.

MBE growth of TiO_2-a via MBE has been described in several prior works, which indicate that (001) TiO_2-a can be stabilized effectively on both $SrTiO_3$ [96,97,98,99,100] and $LaAlO_3$ [101,100,67,99]. The (001) surface is highly active for photocatalysis [93,94,102]. Substrate temperature and Ti deposition rate are identified as important factors in the quality of the resulting film.

There is prior report of hMBE-grown rutile TiO_2 [91], but to the best of my knowledge, no hMBE-grown anatase TiO_2has been reported in literature.

7.1 Anatase TiO_2 via Conventional MBE

TiO_2-a films are grown on LAO substrates with conventional MBE by supplying a 20% O_3, 80% O_2 mixture at pressures between 4.5-5$\times 10^{-7}$ Torr. Substrate temperatures were kept at either 410°

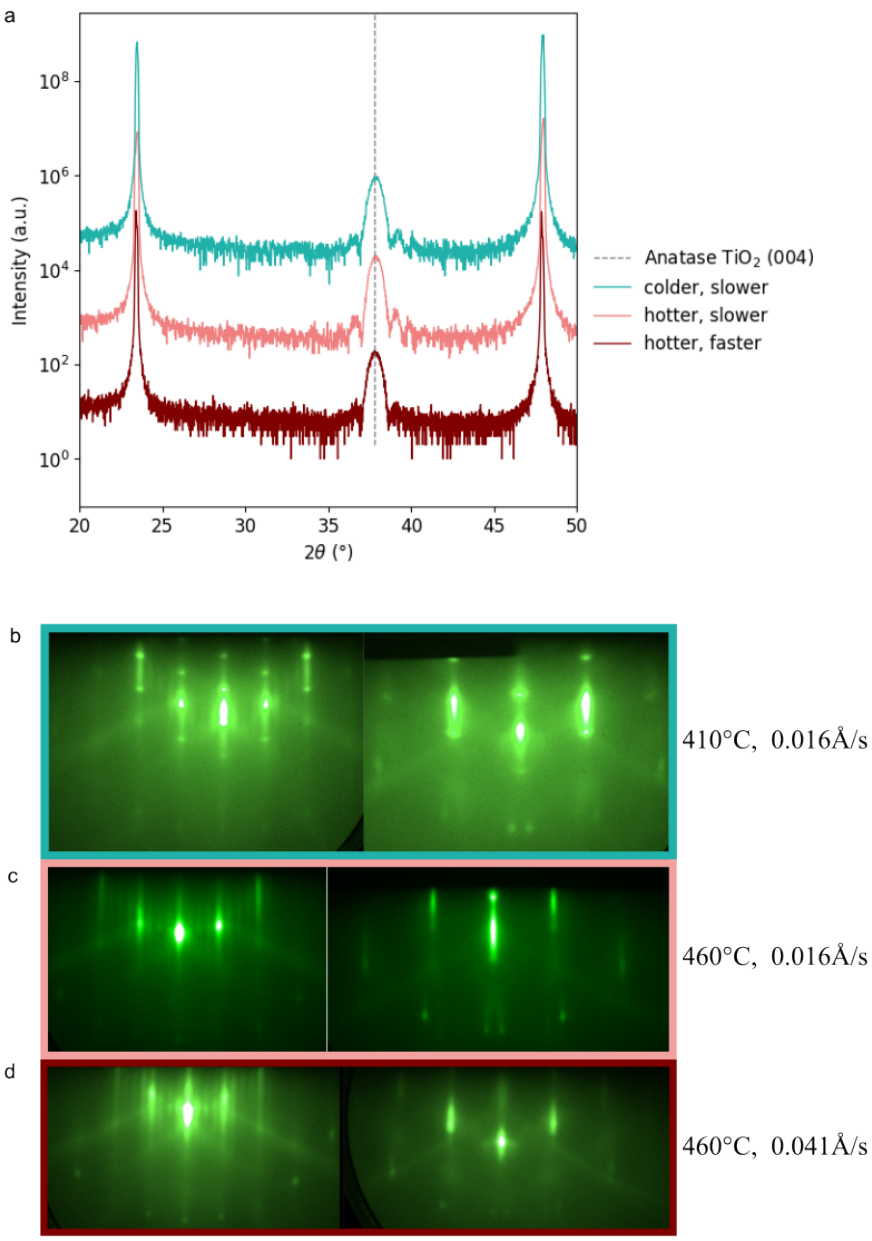

Figure 7.2: Conventional MBE growth of TiO_2-a films. XRD (a) and RHEED (b,c,d) [100] (left) and [110] (right) azimuths of three films. Films are grown either at a colder (410°C), or hotter (460°C) temperature as measured by a thermocouple, and a either a faster (0.041 Å/s) or slower (0.016 Å/s) deposition rate. Films grown with a hotter temperature show both a highly crystalline structure as well as a smooth surface.

or 460°C and a Ti flux of either 1.2×10^{13} atoms/(cm^2·s) or 0.6×10^{13} atoms/(cm^2·s), which correspond to a deposition rate of 0.041 Å/s or 0.016 Å/s respectively. More growth details on the oxidation and MBE system are provided in Chapter 5.1.

Here we choose LAO as a desirable substrate both because of the smaller lattice mismatch (-0.2% for LAO vs -3.1% for STO), and because it is more straightforward to evaluate optical properties for films grown on LAO [101].

Resulting XRD and AFM of the TiO_2-a films can be seen in Figure 7.2. In all cases, the films appear to be single crystal TiO_2-a, with no secondary phases appearing in the XRD. RHEED patterns indicate the characteristic 4×1 reconstruction seen in prior work along the [100] azimuth of the film [67]. The RHEED of the film grown at a colder temperature shows distinct spots along both the [100] and [110] azimuths of the film, indicating higher surface roughness. These results are in line with prior work, although generally we are growing at lower temperatures than previously reported. Films show RHEED intensity oscillations of the (11) and ($\bar{1}$1) reflection along the [110] azimuth of the film, previously reported for the the specular, or (00) reflection in the [100] azimuth [99,67,101]. Both the RHEED oscillations and the thickness of the smooth film can be used to ensure the Ti flux is well known.

7.2 Anatase TiO_2 via Hybrid MBE

Effects of substrate temperature and film growth rate are additionally explored with hybrid MBE using a TTIP source to supply Ti and O, as well as oxygen plasma to supply further oxidative power. Further methods and system details can be found in Chapter 6.2. A plasma with 250W and a pressure of 6×10^{-7} Torr was supplied. Films are grown at a substrate temperature of either 400°C or 495°C. TTIP foreline pressure was kept either at 290 mTorr or 470 mTorr during film growth. Liquid nitrogen was not supplied to the MBE shroud, so the chamber pressure increased significantly

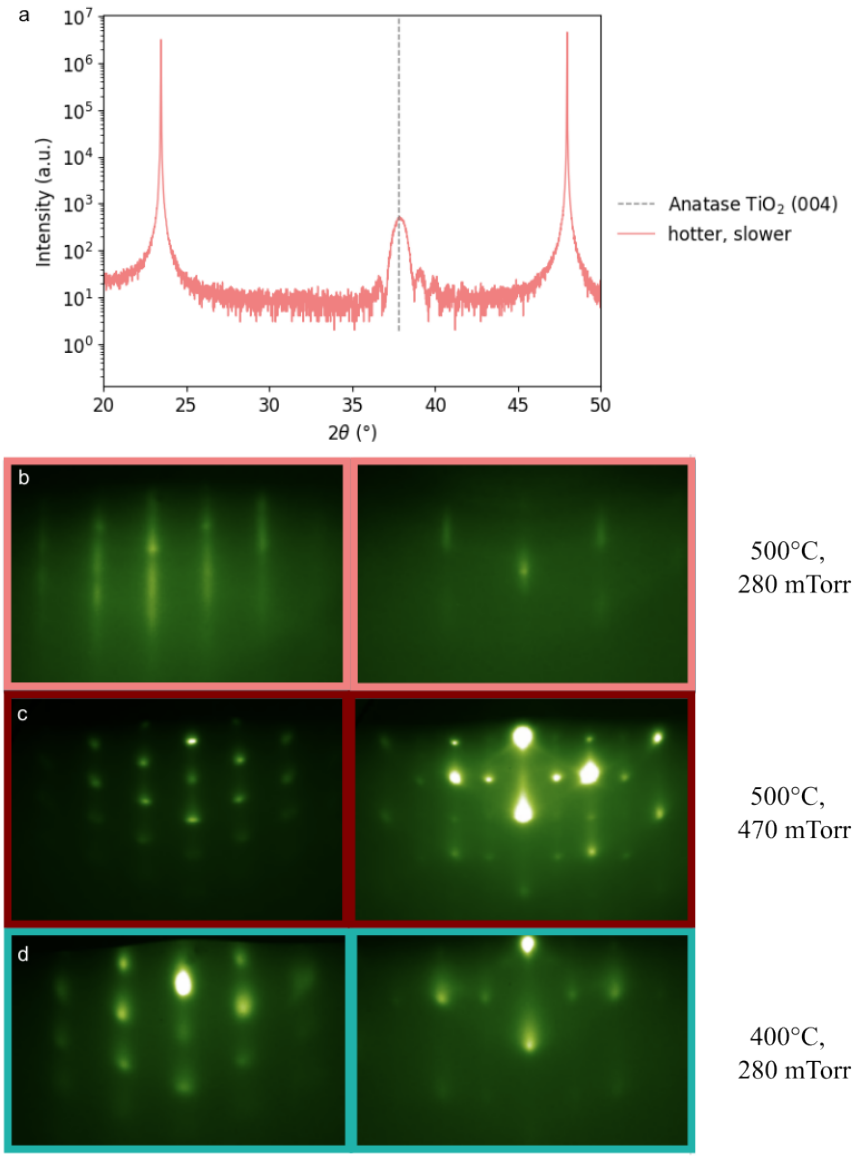

Figure 7.3: Characterization of TiO_2-a films, grown either at a colder (400°C), or hotter (500°C) temperature as measured by a thermocouple, and a either a higher (470 mTorr) or lower (280 mTorr) TTIP foreline pressure. Films grown with a hotter temperature and low TTIP foreline pressure show both a highly crystalline structure as well as a smooth surface in both RHEED and XRR, while growing colder or increasing the growth rate reduces the surface quality of the samples significantly. XRD was not measured on the rough samples.

once the TTIP supply was opened to the chamber, reaching around 2.2×10^{-6} Torr for the lower TTIP foreline pressure and 8×10^{-6} Torr for the higher TTIP foreline pressure. During growth the oxygen plasma partial pressure was kept constant.

Characterization of the hMBE grown films are shown in Figure 7.3. The film grown at a hotter substrate temperature of 495°C and with a lower TTIP pressure of 290 mTorr shows both high quality RHEED and XRD. Unlike with conventional MBE, the RHEED does not show the characteristic 4×1 reconstruction. Low RHEED intensity may be due to high chamber pressure during growth or lack of good RHEED coverage of the film due to platen design. The crystallinity of the hybrid MBE grown film is on par with that of the conventionally grown film based on XRD, implying that this is a promising method for growing high quality anatase.

Film surface quality is significantly degraded for samples grown slow but colder (290 mTorr and 400°C) or hotter but faster (470 mTorr and 400°C). In both cases, RHEED patterns are indicative of a crystalline, 3D-textured film.

One point of interest is the growth rate of the film. Prior work growing rutile TiO_2 with hMBE shows that the sticking factor of the TTIP strongly depends on the substrate temperature when films are grown in vacuum. However when films are grown under 5×10^{-6} Torr of oxygen plasma, the sticking factor does not change significantly for films grown with temperatures between 700-1000°C[89]. Based on XRR taken on the highest quality anatase hMBE sample, the growth rate was 0.047 Å/s, on par with the rates used with our conventional MBE-grown samples. Films grown colder or with higher TTIP pressure were too rough to accurately measure the thickness and thus the effective film growth rate.

References

[1] Ø. Fischer, M. Kugler, I. Maggio-Aprile, C. Berthod, and C. Renner, Reviews of Modern Physics **79**, 353 (2007).

[2] I. Zeljkovic and J. E. Hoffman, Physical Chemistry Chemical Physics **15**, 13462 (2013).

[3] T. Cren, D. Roditchev, W. Sacks, J. Klein, J.-B. Moussy, C. Deville-Cavellin, and M. Laguës, Physical Review Letters **84**, 147 (2000).

[4] C. Howald, P. Fournier, and A. Kapitulnik, Physical Review B **64**, 100504(R) (2001).

[5] K. M. Lang, V. Madhavan, J. E. Hoffman, E. W. Hudson, H. Eisaki, S. Uchida, and J. C. Davis, Nature **415**, 412 (2002).

[6] K. McElroy, D.-H. Lee, J. E. Hoffman, K. M. Lang, J. Lee, E. W. Hudson, H. Eisaki, S. Uchida, and J. C. Davis, Physical Review Letters **94**, 197005 (2005).

[7] M. C. Boyer, W. D. Wise, K. Chatterjee, M. Yi, T. Kondo, T. Takeuchi, H. Ikuta, and E. W. Hudson, Nature Physics **3**, 802 (2007).

[8] A. Pushp, C. V. Parker, A. N. Pasupathy, K. K. Gomes, S. Ono, J. Wen, Z. Xu, G. Gu, and A. Yazdani, Science **324**, 1689 (2009).

[9] C. Howald, H. Eisaki, N. Kaneko, and A. Kapitulnik, Proceedings of the National Academy of Sciences **100**, 9705 (2003).

[10] Y. Wang, Y. Zhong, Z. Luo, M. Liao, R. Wang, Z. Dou, Q. Zhang, D. Zhang, L. Gu, C.-L. Song, X.-C. Ma, and Q.-K. Xue, npj Quantum Materials **4**, 1 (2019).

[11] M. H. Hamidian, S. D. Edkins, S. H. Joo, A. Kostin, H. Eisaki, S. Uchida, M. J. Lawler, E.-A. Kim, A. P. Mackenzie, K. Fujita, J. Lee, and J. C. S. Davis, Nature **532**, 343 (2016).

[12] D. F. Agterberg, J. S. Davis, S. D. Edkins, E. Fradkin, D. J. Van Harlingen, S. A. Kivelson, P. A. Lee, L. Radzihovsky, J. M. Tranquada, and Y. Wang, Annual Review of Condensed Matter Physics **11**, 231 (2020).

[13] G. Grissonnanche, O. Cyr-Choinière, F. Laliberté, S. René de Cotret, A. Juneau-Fecteau, S. Dufour-Beauséjour, M.-È. Delage, D. LeBoeuf, J. Chang, B. J. Ramshaw, D. A. Bonn, W. N. Hardy, R. Liang, S. Adachi, N. E. Hussey, B. Vignolle, C. Proust, M. Sutherland, S. Krämer, J.-H. Park, D. Graf, N. Doiron-Leyraud, and L. Taillefer, Nature Communications **5**, 3280 (2014).

[14] A. Molodyk, S. Samoilenkov, A. Markelov, P. Degtyarenko, S. Lee, V. Petrykin, M. Gaifullin, A. Mankevich, A. Vavilov, B. Sorbom, J. Cheng, S. Garberg, L. Kesler, Z. Hartwig, S. Gavrilkin, A. Tsvetkov, T. Okada, S. Awaji, D. Abraimov, A. Francis, G. Bradford, D. Larbalestier, C. Senatore, M. Bonura, A. E. Pantoja, S. C. Wimbush, N. M. Strickland, and A. Vasiliev, Scientific Reports **11**, 2084 (2021).

[15] H. L. Edwards, J. T. Markert, and A. L. de Lozanne, Physical Review Letters **69**, 2967 (1992).

[16] M. Maki, T. Nishizaki, K. Shibata, and N. Kobayashi, Journal of the Physical Society of Japan **70**, 1877 (2001).

[17] M. Maki, T. Nishizaki, K. Shibata, T. Sasaki, and N. Kobayashi, Physica C: Superconductivity **357–360**, 291 (2001).

[18] H. L. Edwards, A. L. Barr, J. T. Markert, and A. L. de Lozanne, Physical Review Letters **73**, 1154 (1994).

[19] D. J. Derro, E. W. Hudson, K. M. Lang, S. H. Pan, J. C. Davis, J. T. Markert, and A. L. de Lozanne, Physical Review Letters **88**, 097002 (2002).

[20] I. Maggio-Aprile, Ch. Renner, A. Erb, E. Walker, and Ø. Fischer, Physical Review Letters **75**, 2754 (1995).

[21] K. Shibata, M. Maki, T. Nishizaki, and N. Kobayashi, Physica C: Superconductivity Proceedings of the 15th International Symposium on Superconductivity (ISS 2002): Advances in Superconductivity XV. Part I, **392–396**, 323 (2003).

[22] J. E. Bruer, *Scanning Tunneling Microscopy and Spectroscopy on YBa2Cu3O7: New Light on the Subgap States*, Ph.D. thesis, (:unav) (2014).

[23] C. Berthod, I. Maggio-Aprile, J. Bruér, A. Erb, and C. Renner, Physical Review Letters **119**, 237001 (2017).

[24] V. B. Zabolotnyy, S. V. Borisenko, A. A. Kordyuk, J. Geck, D. S. Inosov, A. Koitzsch, J. Fink, M. Knupfer, B. Buchner, S.-L. Drechsler, H. Berger, A. Erb, M. Lambacher, L. Patthey, V. Hinkov, and B. Keimer, Physical Review B **76**, 064519 (2007).

[25] R. Liang, D. A. Bonn, and W. N. Hardy, Physical Review B **73**, 180505(R) (2006).

[26] G. Kresse and J. Hafner, Physical Review B **47**, 558 (1993).

[27] G. Kresse and J. Furthmüller, Computational Materials Science **6**, 15 (1996).

[28] G. Kresse and J. Furthmüller, Physical Review B **54**, 11169 (1996).

[29] G. Kresse and D. Joubert, Physical Review B **59**, 1758 (1999).

[30] J. W. Furness, A. D. Kaplan, J. Ning, J. P. Perdew, and J. Sun, The Journal of Physical Chemistry Letters **11**, 8208 (2020).

[31] J. Ning, C. Lane, B. Barbiellini, R. S. Markiewicz, A. Bansil, A. Ruzsinszky, J. P. Perdew, and J. Sun, Comparing first-principles density functionals plus corrections for the lattice dynamics of YBa$_2$Cu$_3$O$_6$ (2023), arxiv:2310.12259 [cond-mat] .

[32] E. Caldeweyher, S. Ehlert, A. Hansen, H. Neugebauer, S. Spicher, C. Bannwarth, and S. Grimme, The Journal of Chemical Physics **150**, 154122 (2019).

[33] S. Grimme, S. Ehrlich, and L. Goerigk, Journal of Computational Chemistry **32**, 1456 (2011).

[34] S. Ehlert, U. Huniar, J. Ning, J. W. Furness, J. Sun, A. D. Kaplan, J. P. Perdew, and J. G. Brandenburg, The Journal of Chemical Physics **154**, 061101 (2021).

[35] A. A. R. Fernandes, J. Santamaria, S. L. Bud'ko, O. Nakamura, J. Guimpel, and I. K. Schuller, Physical Review B **44**, 7601 (1991).

[36] Z. Jirák, J. Hejtmánek, K. Knížek, and R. Sonntag, Physica C: Superconductivity **267**, 225 (1996).

[37] P. Lazar and R. Podloucky, Physical Review B **78**, 104114 (2008).

[38] H. L. Edwards, Journal of Vacuum Science & Technology B: Microelectronics and Nanometer Structures **12**, 1886 (1994).

[39] S. H. Pan, E. W. Hudson, and J. C. Davis, Review of Scientific Instruments **70**, 1459 (1999).

[40] T. Nishizaki, K. Shibata, M. Maki, and N. Kobayashi, Journal of Low Temperature Physics **131**, 931 (2003).

[41] S. Hüfner, M. A. Hossain, A. Damascelli, and G. A. Sawatzky, Reports on Progress in Physics **71**, 062501 (2008).

[42] S. Misra, S. Oh, D. J. Hornbaker, T. DiLuccio, J. N. Eckstein, and A. Yazdani, Physical Review Letters **89**, 087002 (2002).

[43] S. Sugita, T. Watanabe, and A. Matsuda, Physical Review B **62**, 8715 (2000).

[44] C. Proust and L. Taillefer, Annual Review of Condensed Matter Physics **10**, 409 (2019).

[45] Y. Zhang, C. Lane, J. W. Furness, B. Barbiellini, J. P. Perdew, R. S. Markiewicz, A. Bansil, and J. Sun, Proceedings of the National Academy of Sciences **117**, 68 (2020).

[46] Y. He, Y. Yin, M. Zech, A. Soumyanarayanan, M. M. Yee, T. Williams, M. C. Boyer, K. Chatterjee, W. D. Wise, I. Zeljkovic, T. Kondo, T. Takeuchi, H. Ikuta, P. Mistark, R. S. Markiewicz, A. Bansil, S. Sachdev, E. W. Hudson, and J. E. Hoffman, Science **344**, 608 (2014).

[47] S. H. Pan, E. W. Hudson, A. K. Gupta, K.-W. Ng, H. Eisaki, S. Uchida, and J. C. Davis, Physical Review Letters **85**, 1536 (2000).

[48] J. E. Hoffman, E. W. Hudson, K. M. Lang, V. Madhavan, H. Eisaki, S. Uchida, and J. C. Davis, Science **295**, 466 (2002).

[49] Y.-T. Hsu, M. Berben, M. Čulo, S. Adachi, T. Kondo, T. Takeuchi, Y. Wang, S. Wiedmann, S. M. Hayden, and N. E. Hussey, Proceedings of the National Academy of Sciences **118**, e2016275118 (2021).

[50] O. Cyr-Choinière, D. LeBoeuf, S. Badoux, S. Dufour-Beauséjour, D. A. Bonn, W. N. Hardy, R. Liang, D. Graf, N. Doiron-Leyraud, and L. Taillefer, Physical Review B **98**, 064513 (2018).

[51] J. B. Parise and E. M. McCarron, Journal of Solid State Chemistry **83**, 188 (1989).

[52] D. Zhu, L. Shao, M. Yu, R. Cheng, B. Desiatov, C. J. Xin, Y. Hu, J. Holzgrafe, S. Ghosh, A. Shams-Ansari, E. Puma, N. Sinclair, C. Reimer, M. Zhang, and M. Lončar, Advances in Optics and Photonics **13**, 242 (2021).

[53] A. K. Hamze, M. Reynaud, J. Geler-Kremer, and A. A. Demkov, npj Computational Materials **6**, 130 (2020).

[54] A. Ataei, P. McManamon, C. Bradley, M. Wagner, and E. Ruff, Applied Sciences **11**, 3313 (2021).

[55] C. Xiong, W. H. P. Pernice, J. H. Ngai, J. W. Reiner, D. Kumah, F. J. Walker, C. H. Ahn, and H. X. Tang, Nano Letters **14**, 1419 (2014).

[56] A. B. Posadas, H. Park, M. Reynaud, W. Cao, J. D. Reynolds, W. Guo, V. Jeyaselvan, I. Beskin, G. Z. Mashanovich, J. H. Warner, and A. A. Demkov, ACS Applied Materials & Interfaces **13**, 51230 (2021).

[57] K. J. Kormondy, Y. Popoff, M. Sousa, F. Eltes, D. Caimi, M. D. Rossell, M. Fiebig, P. Hoffmann, C. Marchiori, M. Reinke, M. Trassin, A. A. Demkov, J. Fompeyrine, and S. Abel, Nanotechnology **28**, 075706 (2017).

[58] S. Abel, F. Eltes, J. E. Ortmann, A. Messner, P. Castera, T. Wagner, D. Urbonas, A. Rosa, A. M. Gutierrez, D. Tulli, P. Ma, B. Baeuerle, A. Josten, W. Heni, D. Caimi, L. Czornomaz, A. A. Demkov, J. Leuthold, P. Sanchis, and J. Fompeyrine, Nature Materials **18**, 42 (2019).

[59] K. Suzuki and K. Kijima, Japanese Journal of Applied Physics **44**, 2081 (2005).

[60] W. Cai, C. Fu, J. Gao, Q. Guo, X. Deng, and C. Zhang, Physica B: Condensed Matter **406**, 3583 (2011).

[61] SH. Wemple, M. Didomenico, and I. Camlibel, Journal of Physics and Chemistry of Solids **29**, 1797 (1968).

[62] C. M. Brooks, L. F. Kourkoutis, T. Heeg, J. Schubert, D. A. Muller, and D. G. Schlom, Applied Physics Letters **94**, 162905 (2009).

[63] C. M. Brooks, R. B. Wilson, A. Schäfer, J. A. Mundy, M. E. Holtz, D. A. Muller, J. Schubert, D. G. Cahill, and D. G. Schlom, Applied Physics Letters **107**, 051902 (2015).

[64] S. Lee, C. A. Randall, and Z.-K. Liu, Journal of the American Ceramic Society **90**, 2589 (2007).

[65] S. Lee, C. A. Randall, and Z.-K. Liu, Journal of the American Ceramic Society **91**, 1748 (2008).

[66] D. Filimonov, Z.-K. Liu, and C. Randall, Materials Research Bulletin **37**, 467 (2002).

[67] S. Chambers, C. Wang, S. Thevuthasan, T. Droubay, D. McCready, A. Lea, V. Shutthanandan, and C. Windisch Jr, Thin Solid Films **418**, 197 (2002).

[68] B. Fazlioglu-Yalcin, A. C. Suceava, T. Kuznetsova, K. Wang, V. Gopalan, and R. Engel-Herbert, Advanced Materials Interfaces **10**, 2300018 (2023).

[69] J. Bharathan, J. Narayan, G. Rozgonyi, and G. E. Bulman, Journal of Electronic Materials **42**, 40 (2013).

[70] V. Vaithyanathan, J. Lettieri, W. Tian, A. Sharan, A. Vasudevarao, Y. L. Li, A. Kochhar, H. Ma, J. Levy, P. Zschack, J. C. Woicik, L. Q. Chen, V. Gopalan, and D. G. Schlom, Journal of Applied Physics **100**, 024108 (2006).

[71] J. B. Nelson and D. P. Riley, Proceedings of the Physical Society **57**, 160 (1945).

[72] K. D. Fredrickson, V. V. Vogler-Neuling, K. J. Kormondy, D. Caimi, F. Eltes, M. Sousa, J. Fompeyrine, S. Abel, and A. A. Demkov, Physical Review B **98**, 075136 (2018).

[73] K. J. Choi, M. Biegalski, Y. L. Li, A. Sharan, J. Schubert, R. Uecker, P. Reiche, Y. B. Chen, X. Q. Pan, V. Gopalan, L.-Q. Chen, D. G. Schlom, and C. B. Eom, Science **306**, 1005 (2004).

[74] K. J. Kormondy, Y. Cho, A. B. Posadas, L. Zheng, K. Lai, Q. Wang, M. J. Kim, Q. He, A. Y. Borisevich, M. C. Downer, and A. A. Demkov, Applied Physics Letters **113**, 132902 (2018).

[75] R. A. McKee, F. J. Walker, J. R. Conner, E. D. Specht, and D. E. Zelmon, Applied Physics Letters **59**, 782 (1991).

[76] P. Makuła, M. Pacia, and W. Macyk, The Journal of Physical Chemistry Letters **9**, 6814 (2018).

[77] E. S. Welter, S. Garg, R. Gläser, and M. Goepel, ChemPhotoChem **7**, e202300001 (2023).

[78] P. Jubu, F. Yam, V. Igba, and K. Beh, Journal of Solid State Chemistry **290**, 121576 (2020).

[79] P. R. Jubu, O. Obaseki, A. Nathan-Abutu, F. Yam, Y. Yusof, and M. Ochang, Results in Optics **9**, 100273 (2022).

[80] E. Amonette, P. Dulal, D. Sotir, M. Barone, D. Schlom, and N. J. Podraza, Applied Physics Letters **123**, 052103 (2023).

[81] M. Raekers, K. Kuepper, S. Bartkowski, M. Prinz, A. V. Postnikov, K. Potzger, S. Zhou, A. Arulraj, N. Stüßer, R. Uecker, W. L. Yang, and M. Neumann, Physical Review B **79**, 125114 (2009).

[82] H. Ma, J. Levy, M. D. Biegalski, S. Trolier-McKinstry, and D. G. Schlom, Journal of Applied Physics **105**, 014102 (2009).

[83] M. Bernier, A. Warzecha, L. Duvillaret, J.-L. Lasserre, and A. Paupert, in *SPIE Europe Security and Defence*, edited by G. W. Kamerman, O. K. Steinvall, K. L. Lewis, T. J. Merlet, and R. C. Hollins (Cardiff, Wales, United Kingdom, 2008) p. 71140L.

[84] B. Jalan, J. Cagnon, T. E. Mates, and S. Stemmer, Journal of Vacuum Science & Technology A **27**, 1365 (2009).

[85] R. C. Haislmaier, G. Stone, N. Alem, and R. Engel-Herbert, Applied Physics Letters **109**, 043102 (2016).

[86] Y. Matsubara, K. S. Takahashi, Y. Tokura, and M. Kawasaki, Applied Physics Express **7**, 125502 (2014).

[87] W. Nunn, S. Sandlass, M. Wegner, R. Haislmaier, A. Kumar, M. Tangi, J. LeBeau, E. Quandt, R. D. James, and B. Jalan, Journal of Vacuum Science & Technology A **39**, 040404 (2021).

[88] J. Lapano, M. Brahlek, L. Zhang, J. Roth, A. Pogrebnyakov, and R. Engel-Herbert, Nature Communications **10**, 2464 (2019).

[89] B. Jalan, *Hybrid Molecular Beam Epitaxy for High Quality SrTiO3 Films*, Ph.D. thesis.

[90] B. Jalan, P. Moetakef, and S. Stemmer, Applied Physics Letters **95**, 032906 (2009).

[91] B. Jalan, R. Engel-Herbert, J. Cagnon, and S. Stemmer, Journal of Vacuum Science & Technology A: Vacuum, Surfaces, and Films **27**, 230 (2009).

[92] J. Sun, C. T. Parzyck, J. H. Lee, C. M. Brooks, L. F. Kourkoutis, X. Ke, R. Misra, J. Schubert, F. V. Hensling, M. R. Barone, Z. Wang, M. E. Holtz, N. J. Schreiber, Q. Song, H. Paik, T. Heeg, D. A. Muller, K. M. Shen, and D. G. Schlom, Physical Review Materials **6**, 033802 (2022).

[93] F. Xiong, L.-L. Yin, F. Li, Z. Wu, Z. Wang, G. Sun, H. Xu, P. Chai, X.-Q. Gong, and W. Huang, The Journal of Physical Chemistry C **123**, 24558 (2019).

[94] L. Chu, Z. Qin, J. Yang, and X. Li, Scientific Reports **5**, 12143 (2015).

[95] H. G. Yang, C. H. Sun, S. Z. Qiao, J. Zou, G. Liu, S. C. Smith, H. M. Cheng, and G. Q. Lu, Nature **453**, 638 (2008).

[96] Y. Liang, S. Gan, S. A. Chambers, and E. I. Altman, Physical Review B **63**, 235402 (2001).

[97] Y. Du, D. J. Kim, T. C. Kaspar, S. E. Chamberlin, I. Lyubinetsky, and S. A. Chambers, Surface Science **606**, 1443 (2012).

[98] G. S. Herman and Y. Gao, Thin Solid Films **397**, 157 (2001).

[99] R. Shao, C. Wang, D. E. McCready, T. C. Droubay, and S. A. Chambers, Surface Science **601**, 1582 (2007).

[100] S. Chambers, T. Ohsawa, C. Wang, I. Lyubinetsky, and J. Jaffe, Surface Science **603**, 771 (2009).

[101] M. Murakami, Y. Matsumoto, K. Nakajima, T. Makino, Y. Segawa, T. Chikyow, P. Ahmet, M. Kawasaki, and H. Koinuma, Applied Physics Letters **78**, 2664 (2001).

[102] X.-Q. Gong and A. Selloni, The Journal of Physical Chemistry B **109**, 19560 (2005)